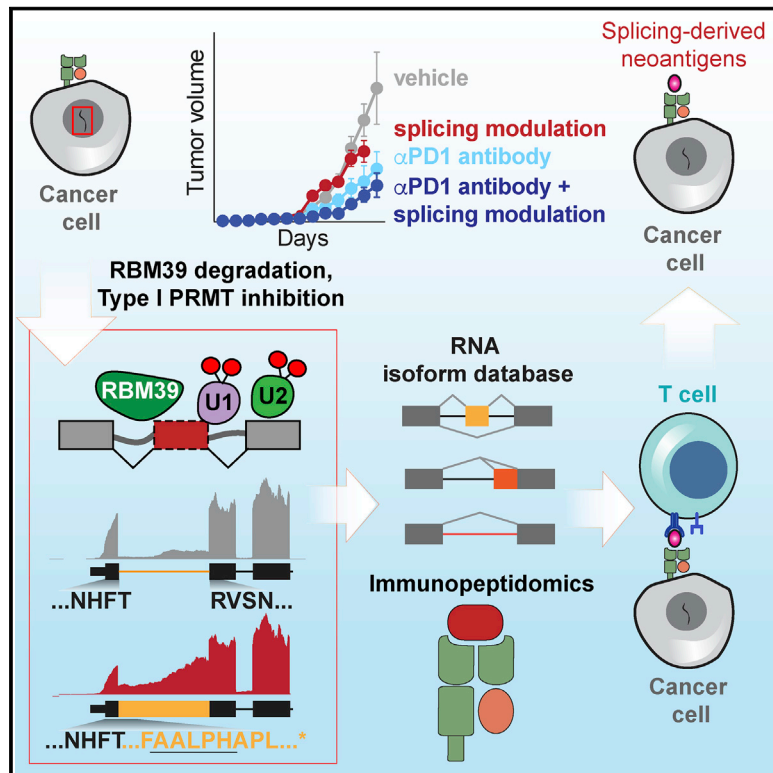


# Pharmacologic modulation of RNA splicing enhances anti-tumor immunity

## Graphical abstract



## Authors

Sydney X. Lu, Emma De Neef, James D. Thomas, ..., Luis A. Diaz, Jr., Omar Abdel-Wahab, Robert K. Bradley

## Correspondence

abdelwao@mskcc.org (O.A.-W.), rbradley@fredhutch.org (R.K.B.)

## In brief

By provoking production of “neoantigens” that are recognized by immune cells, drugs that modulate RNA splicing can enhance cancer immunotherapy.

## Highlights

- Pharmacologic modulation of splicing enhances immune checkpoint blockade efficacy
- RBM39 degradation and type I PRMT inhibition are well tolerated by immune cells
- Splicing perturbation induces splicing-derived neoepitopes that are immunogenic
- Rigorous framework for the identification of splicing-derived antigenic peptides

Article

# Pharmacologic modulation of RNA splicing enhances anti-tumor immunity

Sydney X. Lu,<sup>1,2,15</sup> Emma De Neef,<sup>3,4,5,15</sup> James D. Thomas,<sup>3,4,15</sup> Erich Sabio,<sup>1,6</sup> Benoit Rousseau,<sup>2</sup> Mathieu Gigoux,<sup>1,14</sup> David A. Knorr,<sup>2</sup> Benjamin Greenbaum,<sup>7</sup> Yuval Elhanati,<sup>7</sup> Simon J. Hogg,<sup>1</sup> Andrew Chow,<sup>1,2,14</sup> Arnab Ghosh,<sup>1,2,14</sup> Abigail Xie,<sup>8</sup> Dmitriy Zamarin,<sup>1,2,14</sup> Daniel Cui,<sup>1</sup> Caroline Erickson,<sup>1</sup> Michael Singer,<sup>1</sup> Hana Cho,<sup>1</sup> Eric Wang,<sup>1</sup> Bin Lu,<sup>1</sup> Benjamin H. Durham,<sup>1</sup> Harshal Shah,<sup>1</sup> Diego Chowell,<sup>6,9</sup> Austin M. Gabel,<sup>3,4,5,10</sup> Yudao Shen,<sup>11</sup> Jing Liu,<sup>11</sup> Jian Jin,<sup>11</sup> Matthew C. Rhodes,<sup>12</sup> Richard E. Taylor,<sup>12</sup> Henrik Molina,<sup>13</sup> Jedd D. Wolchok,<sup>1,2,14</sup> Taha Merghoub,<sup>1,2,14</sup> Luis A. Diaz, Jr.,<sup>2</sup> Omar Abdel-Wahab,<sup>1,2,16,\*</sup> and Robert K. Bradley<sup>3,4,5,\*</sup>

<sup>1</sup>Human Oncology and Pathogenesis Program, Memorial Sloan Kettering Cancer Center, New York, NY 10021, USA

<sup>2</sup>Department of Medicine, Memorial Sloan Kettering Cancer Center, New York, NY 10021, USA

<sup>3</sup>Computational Biology Program, Public Health Sciences Division, Fred Hutchinson Cancer Research Center, Seattle, WA 98109, USA

<sup>4</sup>Basic Sciences Division, Fred Hutchinson Cancer Research Center, Seattle, WA 98109, USA

<sup>5</sup>Department of Genome Sciences, University of Washington, Seattle, WA 98195, USA

<sup>6</sup>Center for Immunotherapy and Precision-Oncology, Cleveland Clinic, Cleveland, OH 44195, USA

<sup>7</sup>Department of Epidemiology and Biostatistics, Computational Oncology Program, Memorial Sloan Kettering Cancer Center, New York, NY 10021, USA

<sup>8</sup>Medical Scientist Training Program, Weill Cornell Medical School, New York, NY 10065, USA

<sup>9</sup>The Precision Immunology Institute, The Tisch Cancer Institute, Department of Oncological Sciences, Icahn School of Medicine at Mount Sinai, New York, NY 10029, USA

<sup>10</sup>Medical Scientist Training Program, University of Washington, Seattle, WA 98195, USA

<sup>11</sup>Mount Sinai Center for Therapeutics Discovery, Departments of Pharmacological Sciences and Oncological Sciences, Tisch Cancer Institute, Icahn School of Medicine at Mount Sinai, New York, NY 10029, USA

<sup>12</sup>The Warren Family Research Center for Drug Discovery and Development and the Department of Chemistry and Biochemistry, University of Notre Dame, Notre Dame, IN 46556, USA

<sup>13</sup>Proteomics Resource Center, The Rockefeller University, New York, NY 10065, USA

<sup>14</sup>Swim Across America and Ludwig Collaborative Laboratory, Immunology Program, Parker Institute for Cancer Immunotherapy, Memorial Sloan Kettering Cancer Center, New York, NY 10021, USA

<sup>15</sup>These authors contributed equally

<sup>16</sup>Lead contact

\*Correspondence: [abdelwao@mskcc.org](mailto:abdelwao@mskcc.org) (O.A.-W.), [rbradley@fredhutch.org](mailto:rbradley@fredhutch.org) (R.K.B.)

<https://doi.org/10.1016/j.cell.2021.05.038>

## SUMMARY

Although mutations in DNA are the best-studied source of neoantigens that determine response to immune checkpoint blockade, alterations in RNA splicing within cancer cells could similarly result in neoepitope production. However, the endogenous antigenicity and clinical potential of such splicing-derived epitopes have not been tested. Here, we demonstrate that pharmacologic modulation of splicing via specific drug classes generates bona fide neoantigens and elicits anti-tumor immunity, augmenting checkpoint immunotherapy. Splicing modulation inhibited tumor growth and enhanced checkpoint blockade in a manner dependent on host T cells and peptides presented on tumor MHC class I. Splicing modulation induced stereotyped splicing changes across tumor types, altering the MHC I-bound immunopeptidome to yield splicing-derived neoepitopes that trigger an anti-tumor T cell response *in vivo*. These data definitively identify splicing modulation as an untapped source of immunogenic peptides and provide a means to enhance response to checkpoint blockade that is readily translatable to the clinic.

## INTRODUCTION

Immune checkpoint blockade has greatly improved outcomes for several malignancies that are challenging to treat. Therapeutic benefit is associated with increased mutational burden (Marabelle et al., 2020; Sha et al., 2020) and mismatch repair deficiency (Le et al., 2017), commonly attributed to high tumor

neoantigen load. Coding mutation-derived neoantigens are best studied, but neoantigens can also arise from other processes, such as altered RNA splicing. Two studies analyzing The Cancer Genome Atlas (TCGA) RNA sequencing (RNA-seq) data concluded that tumor-specific alternative splicing is abundant and may generate peptides that contribute to epitope repertoires (Jayasinghe et al., 2018; Kahles et al., 2018). Another

study demonstrated that peptides translated from retained introns arising from incomplete RNA splicing can be presented by MHC I in cancer cell lines (Smart et al., 2018). These provided proof-of-concept that splicing-derived peptides may serve as neoepitopes. However, whether splicing-derived neoepitopes elicit an endogenous immune response remains unknown, in part due to the inherent complexity of RNA processing and corresponding challenges with robustly identifying candidate splicing-derived neoantigens.

Determining whether splicing alterations can generate bona fide neoantigens is particularly important given the development of multiple clinical-grade compounds that alter RNA splicing via non-overlapping mechanisms. Many compounds, such as pladienolide B, GEX1A, E7107, and H3B-8800, inhibit the SF3b splicing complex's interactions with RNA (Lee et al., 2016; Seiler et al., 2018; Sellin et al., 2019; Yokoi et al., 2011). Recently, a series of "anti-cancer sulfonamides," including indisulam and E7820, were found to degrade the accessory splicing factor RBM39 by rendering it a neosubstrate for the Ddb1/CUL4 E3 ubiquitin ligase (Han et al., 2017). Additionally, blocking post-translational modifications of splicing factors, which are required for spliceosome assembly and effective splicing catalysis, can robustly perturb splicing. For example, RNA splicing factors are the most heavily arginine-methylated proteins (Musiani et al., 2019), thus, drugs that block asymmetric or symmetric arginine dimethylation by inhibiting type I or II protein arginine methyltransferases (PRMTs) potentially perturb splicing (Fedorin et al., 2019; Fong et al., 2019).

Here, we address the central question of whether altered RNA splicing generates immunologically meaningful neoantigens to provoke an effective anti-tumor immune response.

## RESULTS

### Pharmacologic perturbation of splicing suppresses tumor growth *in vivo* in a manner dependent on host T cells and tumoral MHC I-presented peptides

We hypothesized that pharmacologic splicing modulation might generate aberrant mRNAs encoding novel proteins, a subset of which could be translated and presented by MHC I as neoepitopes that provoke anti-tumor immunity. We first tested this by treating cancer cell lines with the RBM39-degrader indisulam at doses sub-inhibitory for growth (Figure 1A). This yielded graded RBM39 degradation but little effect on growth (Figures 1B, S1A, and S1B). Across cell lines, *ex vivo* treatment and drug washout yielded sustained suppression of RBM39 protein following drug removal, with minimal effects on subsequent proliferation or apoptosis (Figures 1C, 1D, S1C, and S1D). Drug treatment also did not notably change MHC I/II, PD-L1, cytokine, or death receptor expression (Figures S1E and S1F). In contrast, identical cells exhibited strikingly durable growth inhibition following engraftment into mice, despite transient drug exposure (Figures 1E, 1F, and S1G). The effect was dose dependent, with increasing drug concentrations causing increased splicing alterations (Figures S1H–S1K), reduced tumor growth (Figures S1L–S1N), and improved survival (Figure S1O).

The discrepancy between *in vitro* and *in vivo* growth suggested non-tumor cell-autonomous effects. To assess whether

splicing alterations stimulated an anti-cancer immune response, we repeated our experiments but engrafted treated B16-F10 cells into Rag2-deficient C57BL/6 mice and, separately, into mice with T or natural killer (NK) cell depletion (Figure 1G). *In vivo* tumor growth inhibition was rescued in lymphocyte-deficient Rag2 recipients and by T cell depletion, but not NK depletion, suggesting a T cell and antigen-dependent mechanism (Figures 1H, 1I, and S1P–S1Y).

To test whether MHC I-bound antigens and CD8<sup>+</sup> T cells could be responsible, we evaluated the effects of indisulam versus DMSO pretreatment of isogenic B16-F10 cells with or without CRISPR-mediated knockout (KO) of *B2m*, encoding  $\beta_2$ -microglobulin (Figures 1J and 1K). *B2m* KO rescued the growth inhibition induced by indisulam pretreatment (Figure 1L). Overall, these results indicate that RBM39 degradation impairs cancer growth in a manner dependent on T cells and tumor MHC I expression.

We similarly observed immune-mediated suppression of tumor growth for MS-023, a splicing modulator that inhibits type I PRMT enzymes (Eram et al., 2016). *Ex vivo* MC38 treatment with MS-023 concentrations subinhibitory for *in vitro* growth resulted in globally reduced asymmetric dimethyl arginines (ADMA), but minimal effects on cell growth *in vitro* after drug washout (Figures 2A and S2A). However, identically treated cells yielded durable suppression of tumor growth in C57BL/6 mice (Figures 2B and 2C). These data suggest that splicing modulation can suppress tumor growth *in vivo* across multiple tumor types and mechanisms of splicing perturbation.

We next tested whether splicing modulation enhanced tumor immune recognition via drug-induced neoantigen production. To explore this, we compared the ability of professional antigen-presenting cells (APCs) loaded with lysates from control versus drug-treated tumors to stimulate naive, syngeneic T cells (Figure S2B). MC38 cells were treated with DMSO, indisulam, or MS-023 and used to generate lysates containing potentially immunogenic peptides, but no drug or viable tumor cells. Bone marrow-derived dendritic cells (BMDCs) from wild-type C57BL/6 or *B2m* knockout mice were pulsed with lysates and incubated with CD45.1<sup>+</sup> splenic T cells. BMDCs loaded with lysates from cells treated with indisulam or MS-023 more strongly promoted CD8<sup>+</sup> T cell proliferation than did control BMDCs (Figures 2D and 2E). This effect was not observed with *B2m* KO BMDCs, indicating that MHC I peptide presentation was required.

### Drug-specific effects of splicing modulators on T cells

Our initial studies did not address *in vivo* splicing modulator treatment, which can affect immune and hematopoietic compartments as well as tumors. To address this, we evaluated the effects of multiple classes of splicing modulators on T cell function: indisulam, MS-023, pladienolide B, GEX1A, and the PRMT5 inhibitor EPZ015666 (Chan-Penebre et al., 2015). We first assessed the effects of these drugs on the proliferation of CFSE-labeled, naive splenic T cells upon anti-CD3 and CD8 stimulation (Figure S2C). With 3 days of exposure, indisulam and the PRMT inhibitors had minimal effects on proliferation (IC<sub>50</sub> ~1–10  $\mu$ M), whereas pladienolide B and GEX1A were markedly inhibitory (IC<sub>50</sub> of nMs) (Figures 2F, S2D, and S2E).

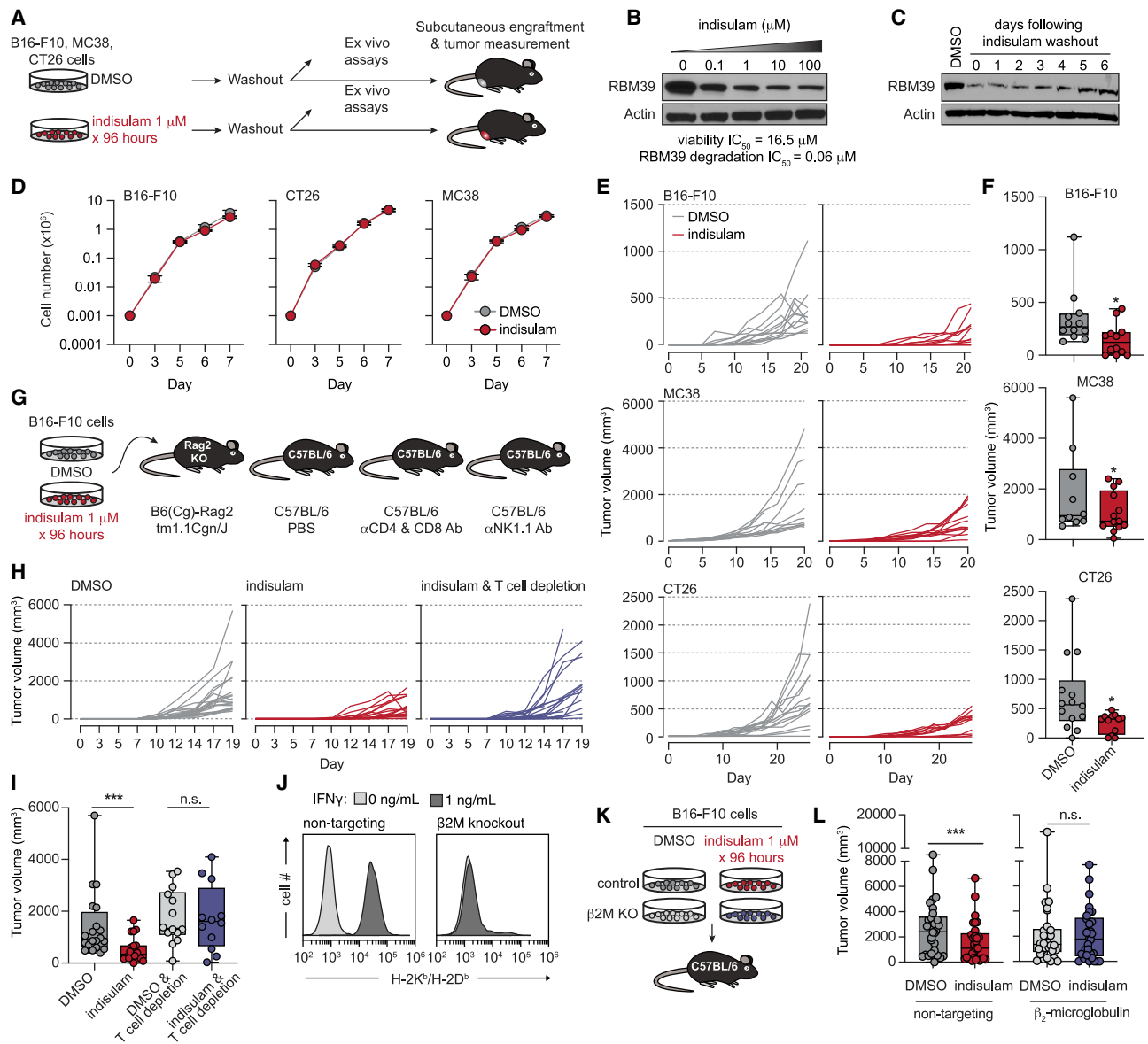


**Figure 1. Pharmacologic RNA splicing modulation impairs tumor growth in a manner dependent on immune recognition**

- (A) Schema of drug treatment and washout.  
 (B) Western blot of RBM39 in B16-F10 cells after 24 h of indisulam treatment.  $IC_{50}$ , half-maximal inhibitory concentration.  
 (C) As (B), but with 4 days of 1  $\mu$ M indisulam, then drug washout and continued culture *in vitro*.  
 (D) Cell growth following 4 days of DMSO or indisulam 1  $\mu$ M, and drug washout (day 0) *in vitro*. Mean  $\pm$  SD.  
 (E) *In vivo* tumor volumes of cells from (D). Each line is an individual tumor (n = 10/group, tumors on both flanks).  
 (F) Box-and-whisker plots of tumor volumes from final day of measurement in (E). For box and whiskers plots throughout, bar indicates median, box edges first and third quartiles, and whiskers minimum and maximum. p from Wilcoxon rank-sum test.  
 (G) Schema of drug treatment and engraftment in mice with immune perturbations.  
 (H) Individual B16-F10 tumor volumes following DMSO or indisulam treatment and engraftment in mice with control versus T cell depletion. Each line is one tumor (n = 10/group).  
 (I) Tumor volumes from (H) at day 19; p from Wilcoxon rank-sum test: \*\*\*p = 0.000379; not significant (n.s.), p > 0.05.  
 (J) H-2K<sup>b</sup>/D<sup>b</sup> expression of control versus B2M KO B16-F10 cells  $\pm$  IFN- $\gamma$ .  
 (K) Schema to evaluate requirement of  $\beta$ 2M for tumor control *in vivo*.  
 (L) Individual tumor volumes at day 30 from (K); p from Wilcoxon rank-sum test: \*\*\*p = 0.009; n.s., p > 0.05.  
 See also Figure S1.

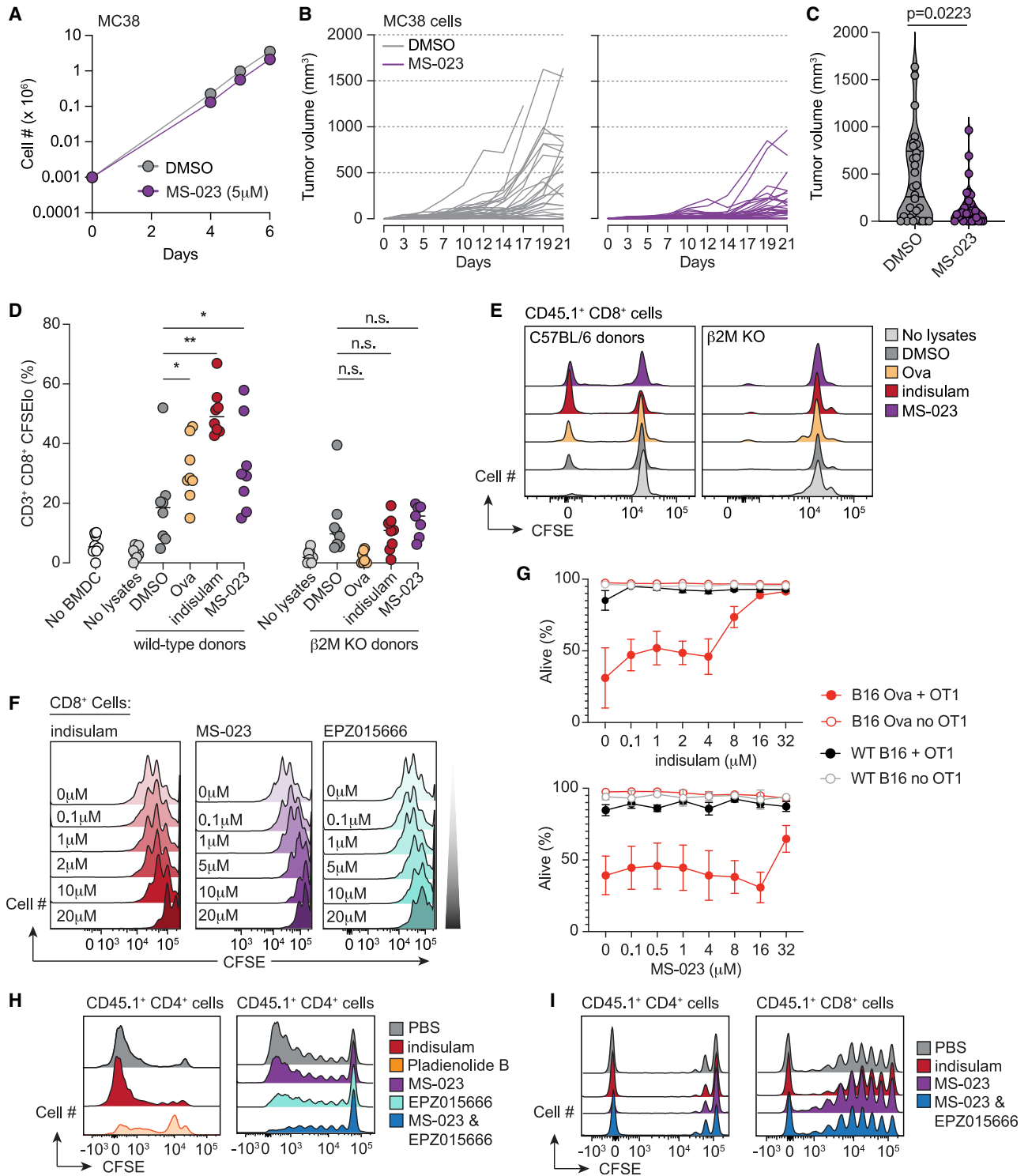


**Figure 2. Pharmacologic splicing modulation promotes T cell reactivity without T cell toxicity *in vivo***

(A) *In vitro* growth of MC38 cells following treatment with DMSO or MS-023 for 96 h and drug washout. Mean  $\pm$  SD shown.

(B) *In vivo* growth of cells from (A) in C57BL/6 mice; individual tumor volumes shown (n = 10/group).

(C) Tumor volumes at day 21 from (B). p from Wilcoxon rank-sum test.

(legend continued on next page)

Measurement of apoptosis and activation markers (Figure S2E) confirmed that these SF3b inhibitors were profoundly immunosuppressive.

We next assessed drug effects on T cell function. Indisulam and MS-023 minimally blunted the *in vitro* cytotoxicity of primed OT-1 T cells against ovalbumin (OVA)-expressing B16-F10 or MC38 cells (Figures 2G and S2F), with little impairment of cell killing at doses <4  $\mu$ M. Exposure to higher drug concentrations did not inhibit OT-1 T cell secretion of interferon (IFN)- $\gamma$  or tumor necrosis factor alpha (TNF- $\alpha$ ) (Figures S2G and S2H) or degranulation (Figures S2I and S2J). We complemented these functional studies by determining the effects of each compound on gene expression in T cells activated with anti-CD3 and CD28 *ex vivo* (Figure S2K). Normally upregulated genes (Figure S2L) were markedly attenuated by pladienolide B, and to a lesser extent EPZ015666, whereas indisulam and MS-023 caused much milder changes (Figure S2M).

We then evaluated the effect of each drug on *in vivo* T cell function in response to antigen. Here, donor CD45.1<sup>+</sup> T cells were adoptively transferred into lethally irradiated recipients that were either syngeneic (C57BL/6), mismatched for non-MHC “minor” antigens (LP/J), or major MHC mismatched (BALB/c; H-2<sup>b</sup> versus H-2<sup>d</sup>) (Figure S2N) (Na et al., 2010). In BALB/c mice, donor T cells showed robust activation and proliferation in response to alloantigen (Figures 2H and S2O–S2Q). Although *in vivo* treatment with indisulam, MS-023, or EPZ015666 resulted in minimal impairment of T cell function (Figures S2P and S2Q), inhibition of both type I and II PRMTs blocked T cell proliferation (Figures 2H and 2I). Pladienolide B was similarly suppressive (Figures 2H, S2O, and S2R). These observations were recapitulated in the C56BL/6  $\rightarrow$  LP/J model (Figure 2I). Indisulam, MS-023, and EPZ015666 were permissive to the homeostatic expansion of T cells after syngeneic adoptive transfer (Figures S2R and S2S).

Last, we assessed the effects of splicing modulators on hematopoiesis in methylcellulose assays. Normal hematopoiesis was intact at even high  $\mu$ M doses of MS-023 and indisulam, whereas EPZ015666 suppressed hematopoiesis (Figure S2T). Pladienolide B suppressed hematopoiesis at nM concentrations (Figure S2T). These data indicate that select splicing modulators can be nontoxic at therapeutic concentrations in preclinical models.

### Modulating splicing enhances immune checkpoint blockade

We next tested whether perturbing RNA splicing together with immune checkpoint blockade promoted control of established tumors. We evaluated *in vivo* RBM39 degradation alone or with anti-PD1 by engrafting C57BL/6 mice with syngeneic tumors

and treated with splicing inhibitors starting on day 3 and anti-PD1 on day 7, the approximate date range at which tumors became measurable (Figure S3A). Simultaneous indisulam and anti-PD1 therapy led to significantly reduced growth of both B16-F10 and MC38 tumors, which exceeded the effects of either drug alone (Figures 3A–3F and S3A) and yielded on-target RBM39 protein reduction (Figure 3B). We observed similar benefits in LLC tumors, which are resistant to anti-PD1 monotherapy (Bertrand et al., 2017; Lesterhuis et al., 2013) (Figures 3G and 3H).

We then evaluated MS-023 *in vivo*, finding that MS-023 treatment significantly improved response to anti-PD1 therapy (Figures 3I–3L). For mice engrafted with MC38 cells, combined MS-023 and anti-PD1 treatment resulted in 50% of mice alive and tumor-free 3 months after engraftment ( $p < 0.001$ ) (Figure 3M). These survivors demonstrated immune memory: upon rechallenge 6 months later with MC38 cells (with or without MS-023 pretreatment *in vitro* before engraftment), they exhibited markedly improved tumor control compared to naive age-matched mice (Figures S3B–S3F).

Finally, we assessed potential toxicity in non-tumor tissues. Treatment with indisulam or MS-023 with or without anti-PD1 did not affect blood counts (Figure S4A). MC38 tumors exhibited increased CD8<sup>+</sup> T cells when indisulam or MS-023 was given with anti-PD1, consistent with intra-tumoral T cell expansion (Figure S4B). Drug-treated animals did not exhibit histologic inflammation or increased CD8<sup>+</sup> infiltrates in the skin, lung, gut, or liver (Figures S4C–S4F). Concordantly, RNA-seq analyses of lung, colon, and splenic T cells from indisulam-treated mice showed mild splicing changes (Figures S4G–S4K), and gene pathway analyses did not reveal an inflammatory signature (Figures S4L–S4O).

### Splicing modulators induce RNA isoforms encoding predicted neoepitopes

We next determined the molecular mechanisms by which splicing modulation enhances anti-tumor immunity. We assessed how splicing modulation altered tumor cell transcriptomes in murine tumor cell lines treated with DMSO, indisulam, or MS-023, performed high-coverage RNA-seq, and quantified differential gene and isoform expression. Both drugs drove dramatic changes in alternative and constitutive splicing, with differential cassette exon inclusion and constitutive intron retention the most common alterations (Figures 4A and S5A–S5C; Tables S1 and S2). Identical experiments in human tumor cell lines revealed similar changes (Figures 4B and S5D–S5F; Tables S3 and S4). A subset of mis-splicing events were consistently induced across all cell lines in a given species (Figures

(D) Percentage of live donor CD8<sup>+</sup>CFSE<sup>lo</sup> T cells on day 5 of a mixed leukocyte reaction with BMDC from wild-type or *B2m* KO C57BL/6 mice. Each dot is a technical replicate. Bar represents median. “No lysates”: T cells cultured with BMDC and without lysate.  $p$  from Wilcoxon rank-sum test. For wild-type BMDCs, DMSO-versus-Ova  $p = 0.019$ , versus indisulam  $p = 0.001$ , versus MS-032  $p = 0.032$ .

(E) Representative histograms of CFSE dilution from (D).

(F) CFSE-labeled naive splenic T cells from C57BL/6 mice stimulated with anti-CD3 and CD28 for 3 days.

(G) Wild-type or ovalbumin-expressing B16-F10 cells were cultured alone or with primed OT-1 T cells for 18 h and viable tumor cells enumerated.

(H) CFSE dilution of donor CD45.1<sup>+</sup> T cells adoptively transferred into irradiated BALB/c recipients treated with the indicated compounds. Donor splenic CD4<sup>+</sup> T cells on day 3.

(I) As (H), but in LP/J recipients; donor splenic T cells on day 5.

See also Figure S2.

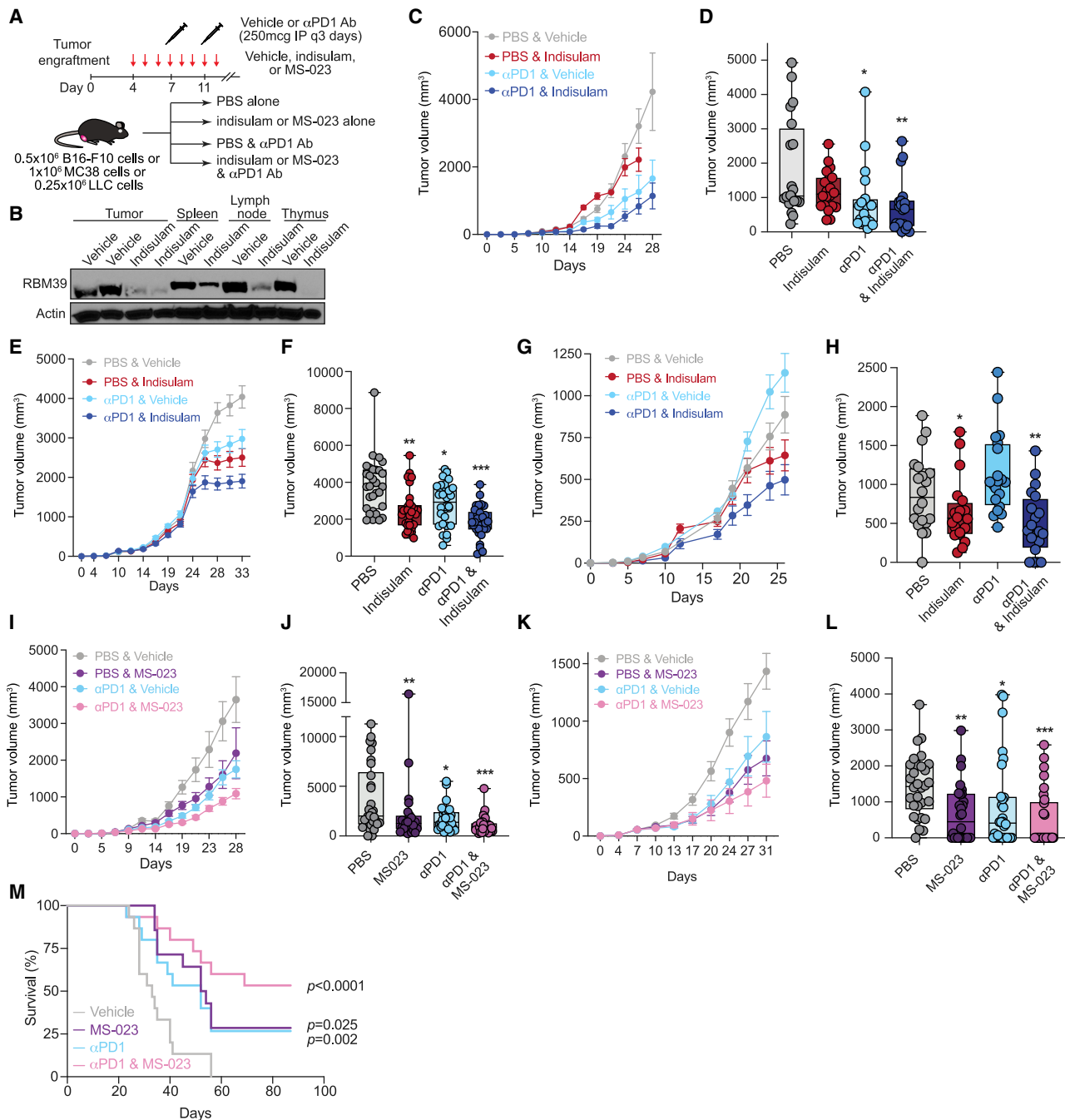


**Figure 3. Splicing modulation enhances checkpoint immunotherapy**

(A) Treatment schema.

(B) Western blot of RBM39 in B16-F10 and immune organs of mice treated with vehicle versus indisulam for 10 days.

(C) B16-F10 tumor volumes in mice treated with vehicle, indisulam, anti-PD1, or both (n = 10/group). Mean  $\pm$  SEM. Termination of line before day 28 indicates all animals had reached endpoints.

(D) Data from (C) at day 26; p from Wilcoxon rank-sum test versus PBS; \*p = 0.002; \*\*p = 0.000581. p indisulam versus  $\pm$  PD1 = 0.004.

(E) As (C), but for MC38 tumor-bearing mice (n = 10/group).

(F) Data from (E) at day 31; p as above. \*p = 0.004; \*\*p = 0.0000682; \*\*\*p = 0.00000101. p indisulam versus  $\pm$  PD1 = 0.04.

(G) As (C), but for LLC tumor-bearing mice (n = 10/group).

(H) Data from (G) at day 26. p as above. \*p = 0.048; \*\*p = 0.004. p indisulam versus  $\pm$  PD1 = 0.125.

(legend continued on next page)

S5G–S5I), and 29.0% (indisulam) and 9.1% (MS-023) of mis-spliced genes were mis-spliced in both species (Figure S5J), consistent with conserved splicing mechanisms.

Indisulam and MS-023 gave rise to distinct downstream splicing alterations (Figure S5K). Indisulam-induced splicing alterations were dominated by reduced splicing efficiency: cassette exons were preferentially not included and constitutive introns were preferentially not excised (Figures 4C and 4D). MS-023, in contrast, resulted in more balanced changes (Figures S5C and S5F). Nonetheless, convergent mis-splicing between drugs was relatively common (~4%–8% of mis-spliced events) (Figures S5L and S5M). Constitutive introns preferentially retained following indisulam treatment were significantly depleted for poly(AT) (Figures 4E and 4F), consistent with RBM39 binding of poly(AT) motifs (Wang et al., 2019) and on-target RBM39 degradation. For MS-023, we observed no such obvious motif enrichment, as expected given the broad effects of type I PRMT inhibition.

We next evaluated the cytoplasmic availability of mis-spliced mRNAs for translation. Because splicing is linked to cytoplasmic mRNA export (Zhou et al., 2000), splicing alterations could fail to yield novel peptides. We separated nuclear and cytoplasmic RNA pools from DMSO- and indisulam-treated cells (focusing on indisulam because it led to global decreases in splicing efficiency) (Figure S5N) and quantified drug-induced isoforms in each subcellular compartment. Indisulam-induced intron retention was readily apparent in the cytoplasmic fraction (Figures 4G, S5O, and S5P), where such mRNAs could be translated into potential neoepitopes (Figure 4H).

We finally estimated the potential consequences of indisulam-induced splicing alterations for neoepitope production. We enumerated all 8–14 amino acid sequences (8- to 14-mers) arising from mRNA isoforms in the transcriptome and estimated the binding affinity of each to common MHC I alleles with NetMHCpan. We restricted this list to predicted binders, then epitopes arising from differentially spliced genes, and finally epitopes from isoforms promoted by indisulam treatment. This filtering dramatically reduced the space of potential neoepitopes (Table S5), with most arising from cassette exons and constitutive introns (Figures 4I and 4J). Many predicted neoepitopes were shared within mouse (5,764) or human (24,378) cell lines (Figure S5Q), whereas fewer (1,763) were shared across species (Figure S5R), presumably reflecting non-conserved splicing alterations and differences in binding preferences of murine and human MHC.

### Drug-induced, splicing-derived neoepitopes are presented by MHC I on tumor cells

We augmented transcriptomic analyses with experimental identification of splicing-derived neoepitopes. We purified H-2K<sup>b</sup> and H-2D<sup>b</sup> from DMSO versus indisulam-treated B16-F10 cells,

eluted bound peptides, and performed liquid chromatography-tandem mass spectrometry (LC-MS/MS) (Figure 5A).

As MHC I-bound peptide identification from mass spectrometry depends critically upon the search database (proteome) (Murphy et al., 2017), we tested four distinct proteomes. These were “full-length” (i.e., all full-length protein sequences in the transcriptome) “predicted binders,” restricted to 8- to 14-mers that were predicted MHC I binders; “predicted binders + spiked non-binders,” augmented with decoy predicted non-binders; and “filtered predicted binders,” restricted to predicted binders from differentially expressed or spliced genes (Figure 5B).

We first evaluated the full-length proteome. Approximately 80% and 86% of identified peptides were predicted binders for H-2D<sup>b</sup> and H-2K<sup>b</sup> versus 0.6% and 0.9% for peptides randomly sampled from the proteome (Figures 5C and S6A). Repeating this analysis with MHCflurry (O'Donnell et al., 2018) yielded similar results (not shown). Identified peptides had expected sequence preferences at anchor residues and preferential identification of 9-mers and 8- to 9-mers for H-2D<sup>b</sup> and H-2K<sup>b</sup>, respectively (Figures 5D, S6B, and S6C). We next varied the input proteome to maximize peptide identification. Restricting the search to predicted binders increased recovery ~2-fold relative to the full-length proteome, whereas further restricting to differentially expressed or spliced genes decreased recovery ~3.4-fold for H-2D<sup>b</sup> (Figure 5E), with similar results for H-2K<sup>b</sup> (Figure S6D). Restricting to predicted binders did not decrease specificity: we identified only 2 predicted non-binders, versus 2,204 predicted binders, across all six replicates when we queried the spiked non-binder proteome for H-2D<sup>b</sup> (Figure 5F), again with similar results for H-2K<sup>b</sup> (Figure S6E). Because the predicted binders proteome maximized yield while minimizing false-positives, we used it for subsequent analyses. The vast majority of identified peptides arose from genes expressed at moderate to high levels in B16-F10 cells (Figures 5G and S6F).

We identified 518 and 366 peptides for H-2D<sup>b</sup> and H-2K<sup>b</sup> that were only recovered from indisulam-treated samples (Figure 5H). We intersected these with predicted isoform-specific epitopes identified by RNA-seq (Figure 4J) to obtain 42 and 28 peptides that were bound by H-2D<sup>b</sup> and H-2K<sup>b</sup>, respectively, and arose from mRNA isoforms that were promoted by indisulam treatment (Figure 5I; Table S6). Due to the known limited sensitivity of mass spectrometry for the MHC I immunopeptidome (Schuster et al., 2018), we also nominated an additional 39 candidate peptides that were supported by RNA-seq alone, but predicted to be high-affinity binders to H-2D<sup>b</sup> or H-2K<sup>b</sup> (Figure S6G; Tables S1 and S2). We used this set of 109 (70 from mass spectrometry, 39 from RNA-seq) high-confidence, potentially antigenic peptides in subsequent functional assays.

(I) Tumor volumes of B16-F10 tumor-bearing mice treated with vehicle, MS-023, anti-PD1, or both (n = 10/group). Mean ± SEM.

(J) Data from (I) at day 28; p as above. \*p = 0.023; \*\*p = 0.013; \*\*\*p = 0.0000153. p MS-023 versus ± PD1 = 0.056.

(K) As (I), but for MC38 tumor-bearing mice.

(L) Data from (I) at day 31; p as above. \*p = 0.001; \*\*p = 0.000342; \*\*\*p = 0.00000821. p MS-023 versus ± PD1 = 0.101.

(M) Kaplan-Meier survival from (I). All survivors past day 60 were tumor-free. p from log-rank test versus vehicle.

See also Figures S3 and S4.

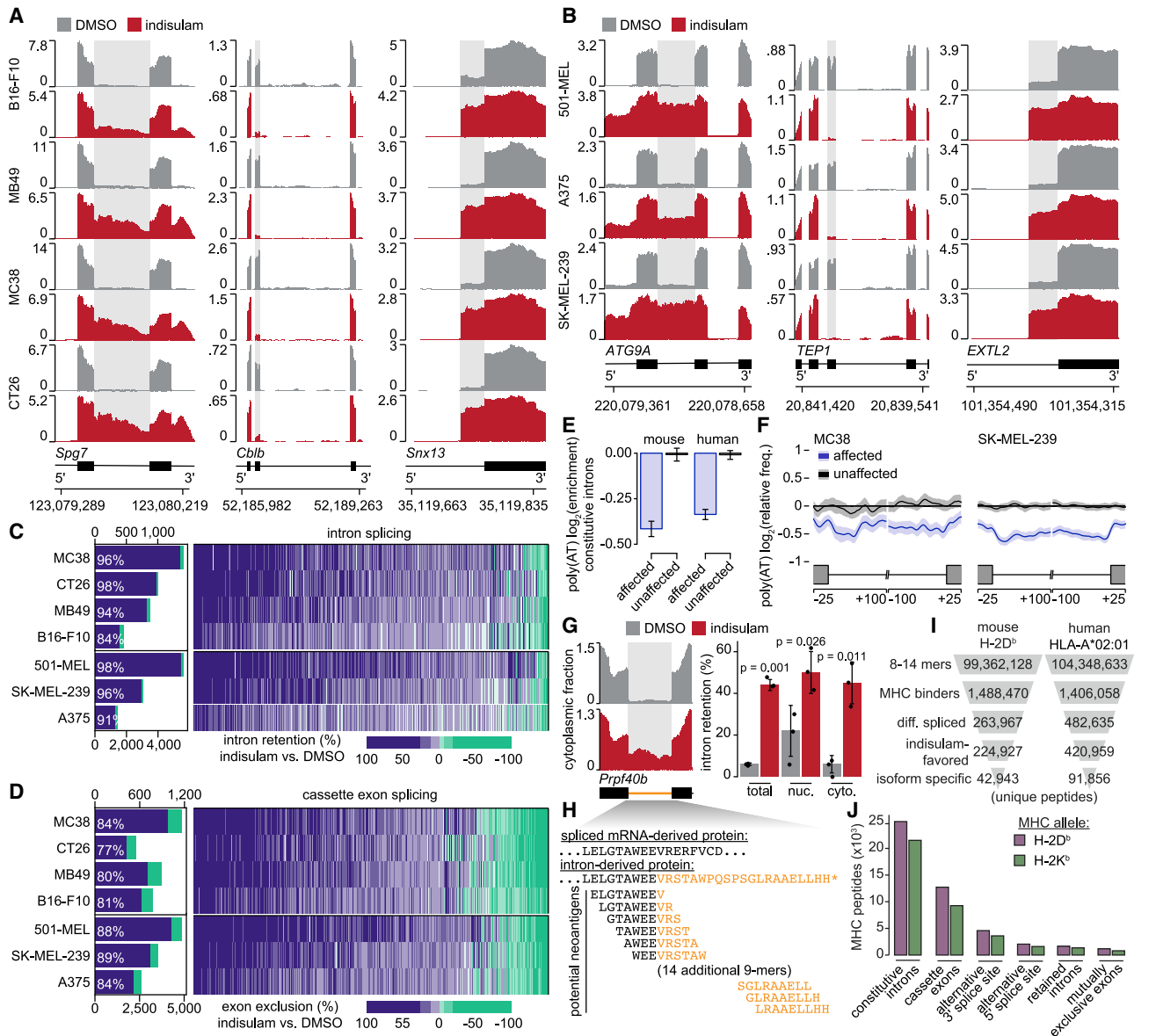


**Figure 4. Splicing modulation induces widespread potential neoepitope production**

(A and B) RNA-seq read coverage illustrating shared intron retention (left), cassette exon exclusion (middle), and competing 3' splice site selection (right) induced by indisulam in mouse (A) and human cancer cell lines (B). Conditions as in Figure 1A.

(C) Left: stacked bar graph illustrating numbers of differentially retained introns following indisulam treatment. Blue/green, increased/decreased intron retention in indisulam versus DMSO; percentages shown for blue. Right: heatmap illustrating quantitative extent of intron retention for introns significantly mis-spliced in at least one sample.

(D) As (C), but for cassette exons.

(E) Bar graph of poly(AT) motif enrichment in introns preferentially retained versus unaffected upon indisulam treatment. Motif enrichment computed relative to a randomly selected group of unaffected introns. Error bars, 95% confidence intervals estimated by bootstrapping.

(F) Metagenes plot of poly(AT) enrichment across introns that were preferentially retained or unaffected following indisulam treatment. Shading, 95% confidence intervals estimated by bootstrapping.

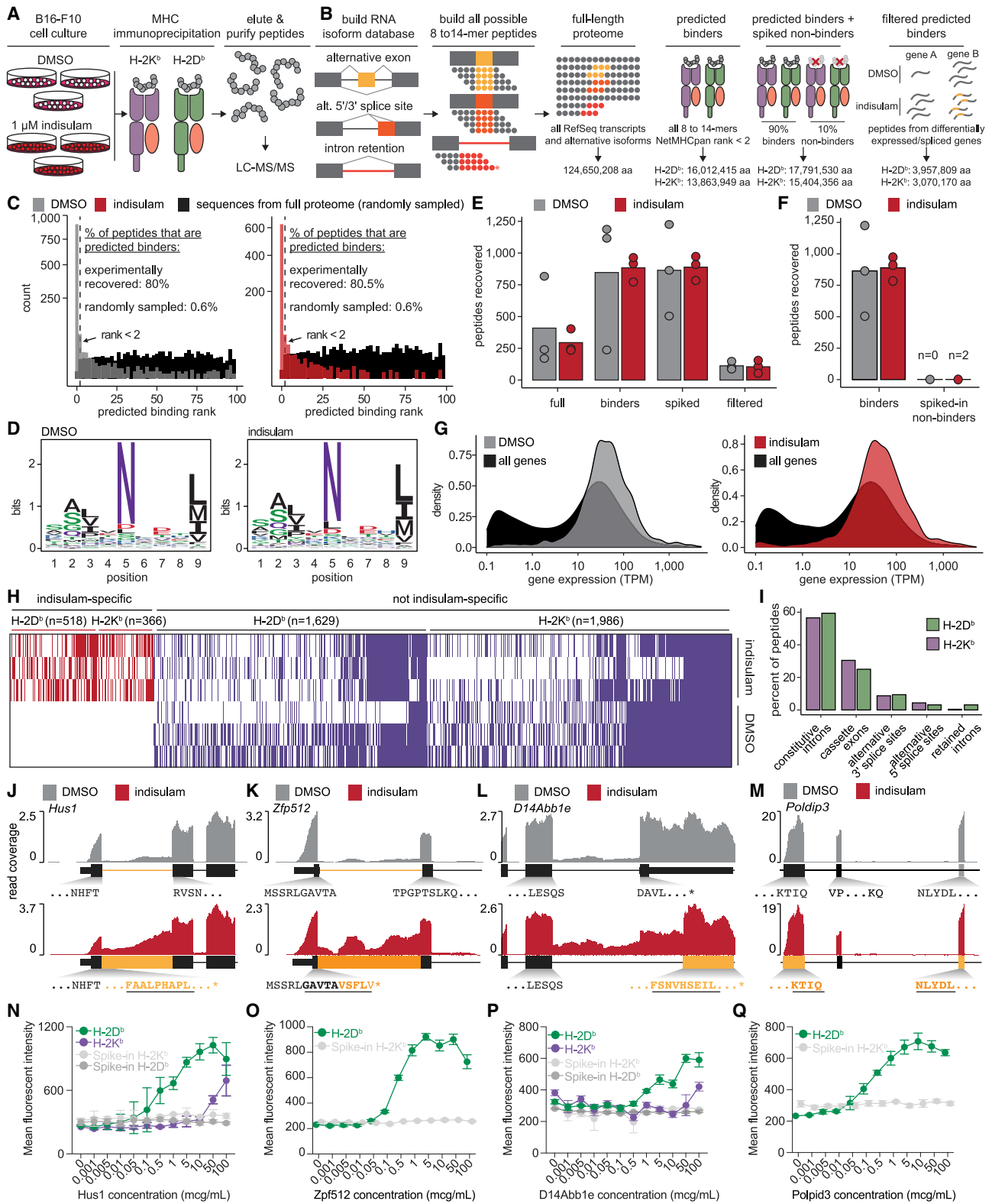
(G) Left: RNA-seq read coverage illustrating *Prpf40b* intron retention in the cytoplasmic fraction following indisulam treatment of B16-F10. Right: quantification of *Prpf40b* intron retention in total, nuclear (nuc.), and cytoplasmic (cyto.) fractions. p from unpaired t test.

(H) Predicted 9-mer peptides arising from indisulam-induced *Prpf40b* intron retention. Black/blue, exon/intron-derived amino acids.

(I) Filtering strategy to predict potential indisulam-induced, MHC I bound epitopes. Numbers of unique peptides present at each step are shown for representative MHC I alleles following DMSO or indisulam treatment of B16-F10 and 501-MEL cells.

(J) Bar graph illustrating numbers of predicted indisulam-induced 8- to 14-mer peptides arising from different splicing events following DMSO or indisulam treatment of B16-F10 cells. All analyses performed for n = 3 biological replicates for each cell line and treatment unless specified otherwise.

See also Figure S5 and Tables S1, S2, S3, S4, and S5.



(legend on next page)

### Splicing-derived neoantigens can trigger an endogenous T cell response

We experimentally assessed binding of each of our 109 candidate neoantigenic peptides, which arose from diverse splicing changes (Figures 5I–5M), to H-2D<sup>b</sup> or H-2K<sup>b</sup> in the RMA-S stabilization assay (Figure S7A) (De Bruijn et al., 1991; De Silva et al., 1999). Candidate peptides had a range of abilities to stabilize H-2 molecules, with ~97% (68/70) of peptides identified from both MHC I mass spectrometry and RNA-seq exhibiting some binding, and several exhibiting very strong binding (Figures 5N–5Q, 6A, and S7B). Negative control “spike-in” peptides showed no binding.

Because MHC I binding is imperfectly correlated with immunogenicity, we experimentally tested each candidate. We immunized naive mice with each of the 109 peptides by hock injection, obtained draining lymph nodes (Figure 6B), and performed IFN- $\gamma$  ELISpot with purified CD8<sup>+</sup> T cells incubated with naive, syngeneic splenocytes loaded with DMSO or cognate peptide (Table S7). ~43% (30/70) of peptides with both mass spectrometry and RNA-seq support elicited a CD8<sup>+</sup> T cell response (Figures 6C, 6D, and S7C), and several such peptides were induced by indisulam in all tested mouse cancer cell lines (Figure S6G). We further confirmed the specificity of these responses by immunizing across a range of peptide doses, revealing a dose-dependent CD8<sup>+</sup> T cell response (Figures 6E, S7D, and S7E).

All 39 candidate peptides selected based solely on RNA-seq analyses and MHC I binding predictions exhibited some H-2 binding (Figure S7F), and 28% (11/39) were immunogenic *in vivo* (Figure S7G). Our *in silico* analyses thereby identified a reasonable proportion of splicing-derived, potentially immunogenic peptides, but nonetheless a number of candidate peptides with verified MHC I binding failed to elicit CD8<sup>+</sup> T cell activation *in vivo* (Figures S7H–S7J). To understand the basis for this differential response, we interrogated potential distinctions between immunogenic and nonimmunogenic splicing-derived peptides. Analyses of pre-

dicted binding affinity (NetMHCpan), experimental ability to stabilize MHC I (RMA-S assay), parent gene expression, type and magnitude of splicing alteration, and predicted induction of NMD revealed that only binding to MHC I (NetMHCpan or RMA-S assay) differed significantly between immunogenic and nonimmunogenic peptides (Figures 6F and 6G).

We next tested the ability of CD8<sup>+</sup> T cells from peptide-immunized mice to kill tumor cells presenting the cognate peptide. Although DMSO-immunized CD8<sup>+</sup> T cells exerted no cytotoxic activity regardless of the peptide presented, CD8<sup>+</sup> T cells from mice immunized with an immunogenic peptide selectively killed B16-F10 cells presenting that same peptide (Figures 7A and 7B).

Finally, we assessed the endogenous consequences of splicing-derived peptide production by testing whether drug-treated tumors generated neoantigenic peptides at concentrations that activated CD8<sup>+</sup> T cells. We repeated the above experiments, but used B16-F10 cells treated with indisulam as APCs (Figure 7C). This demonstrated that indisulam treatment of tumor cells indeed stimulates endogenous generation of specific splicing-derived neoantigens that trigger antigen-specific T cell activation (Figures 7D–7H). We therefore tested whether indisulam treatment drove the expansion of antigen-specific CD8<sup>+</sup> T cells that recognized neoantigenic peptides *in vivo* (Figure 7I). We generated H-2K<sup>b</sup> tetramers loaded with peptides that elicited strong IFN- $\gamma$  secretion and cytotoxicity in the above experiments. These were used to stain tumor-draining lymph nodes of B16-F10 tumor-bearing mice treated with vehicle, indisulam, anti-PD1, or the combination (Figures 7J and S7K). This revealed increased frequencies of CD8<sup>+</sup> T cells capable of recognizing splicing-derived peptides in mice receiving indisulam or the combination of indisulam and anti-PD1 (Figure 7K). Together, these data demonstrate that splicing modulation triggers the production of specific splicing-derived neoantigens at levels sufficient to drive expansion of CD8<sup>+</sup> T cells recognizing those antigens.

#### Figure 5. Indisulam-induced neopeptides are presented by MHC I

(A) Workflow overview.

(B) Schematic for RNA isoform and proteome database creation.

(C) Histogram of predicted NetMHCpan binding rank of all peptides identified from the H-2D<sup>b</sup> immunoprecipitation (IP) and full-length proteome. Peptides with rank <2 are predicted binders. Peptides identified in DMSO-treated (gray, left) and indisulam-treated (red, right) samples are overlaid on a random sample of 1,000 sequences from the full-length proteome (black) for comparison.

(D) Sequence logo for 9-mers identified from the H-2D<sup>b</sup> IP and full-length proteome.

(E) Bar plot of numbers of peptides identified from the H-2D<sup>b</sup> IP using each proteome in (B).

(F) Bar plot of numbers of predicted binders and non-binders identified from H-2D<sup>b</sup> IP using the spiked non-binders proteome, which consists of predicted binders (rank <2) composing 90% of this proteome, and non-binders (rank >90), added to constitute 10% of the proteome.

(G) Density plots of parent gene expression for peptides identified from the H-2D<sup>b</sup> IP from DMSO-treated (gray, left) and indisulam-treated (red, right) samples, each compared to the expression of all genes (black) following treatment with DMSO or indisulam, respectively, using the predicted binders proteome. TPM, transcripts per million.

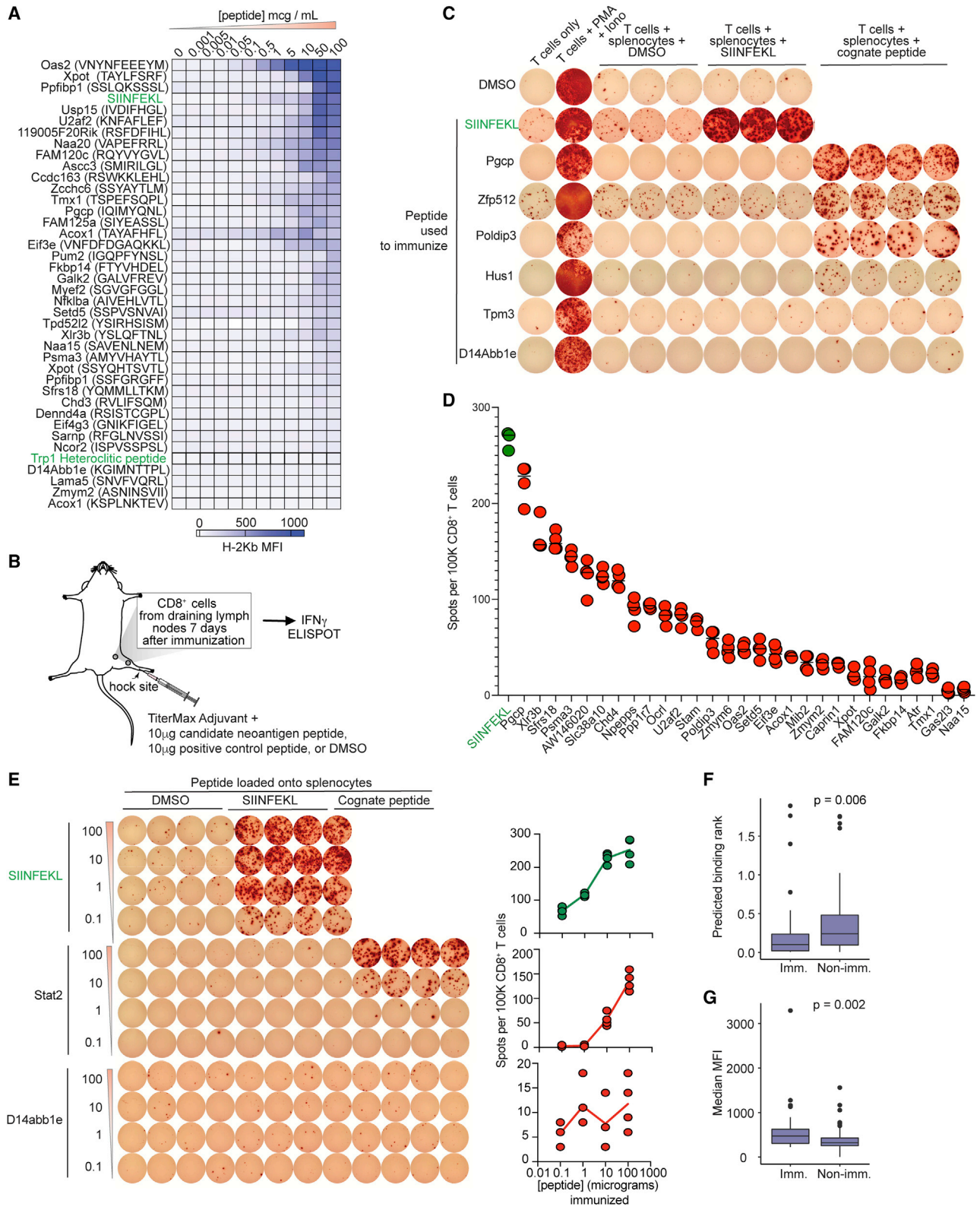
(H) Heatmap illustrating each peptide identified in at least one replicate (rows) using the predicted binders proteome. Columns are peptides.

(I) Bar plot illustrating percentages of indisulam-specific, isoform-specific identified peptides arising from different types of alternative splicing.

(J–M) RNA-seq coverage plots of representative indisulam-induced, candidate splicing-derived neopeptides generated by intron retention in (J) *Hus1* and (K) *Zfp512*, (L) competing 3' splice sites in *D14Abb1e*, and (M) cassette exon skipping in *Poldip3*. Indisulam-promoted peptide shown in bold, underlined text.

(N–Q) Median fluorescence intensities (MFIs) of H-2D<sup>b</sup> and/or H-2K<sup>b</sup> on RMA-S cells following incubation with increasing doses of (N) *Hus1*, (O) *Zfp512*, (P) *D14Abb1e*, and (Q) *Poldip3* candidate neoantigenic peptides from (J)–(M). Mean  $\pm$  SD shown. For (N)–(Q), gray lines indicate negative control peptides randomly selected from the predicted non-binder, “spike-in” peptides used in (B). All analyses performed for n = 3 biological replicates for each treatment for (A)–(M) and n = 4 biological replicates for (N)–(Q). For (C), (D), and (G), data collated across n = 3 replicates per treatment.

See also Figure S6 and Table S6.



(legend on next page)

## DISCUSSION

Mutation-derived neoantigen burden is an established determinant of response to immune checkpoint blockade. Here, we describe a distinct and abundant source of immunogenic peptides derived from novel mRNA species. We demonstrated that multiple clinical-grade compounds, acting via distinct mechanisms, can thereby enhance immune checkpoint blockade by inducing such MHC I-presented neopeptides. These studies thus identify a means to acutely and reversibly induce tumor neoantigens without genomic changes and demonstrate the antigenic potential of splicing-derived neopeptides *in vivo*.

Splicing modulation generates many novel mRNAs derived from large-scale events, including inclusion of intronic sequence into mature mRNA, juxtaposition of exons not normally spliced together, and exons with abnormal 5' or 3' ends. Each can result in the production of peptides containing wholly novel sequences—confirmed by our cytoplasmic RNA sequencing and MHC I mass spectrometry—potentially contributing to the many immunogenic peptides that we identified.

Although direct comparisons of the frequencies of neoantigens derived from aberrant splicing to those derived from single-nucleotide variants is challenging due to differences in experimental methodologies, the frequency of antigenic peptides derived from splicing may be high. For example, of candidate neoantigenic peptides derived from intersecting RNA-seq and MHC I proteomics, we found that 30 of 70 (~43%) could elicit a CD8<sup>+</sup> T cell immune response in naive C57BL/6 mice by IFN- $\gamma$  ELISpot. Predicted neoantigenic peptides derived from RNA-seq alone exhibited a positivity rate of 11/39 (~28%). Of these neoantigenic peptides, we then demonstrated that four were associated with the expansion of antigen-specific CD8<sup>+</sup> T cells following splicing modulator treatment *in vivo*. In comparison, an early seminal study of MC38 cells reported that out of ~1,300 coding variations, ~13% resulted in peptides predicted to bind MHC I, 0.5% of which were identified by mass spectrometry and ~0.25% of which were immunogenic *in vivo* (Yadav et al., 2014). A recent consortium effort evaluating human melanoma and non-small cell lung cancer neoantigens predicted to bind MHC reported an immunogenicity rate of 6% (Wells et al., 2020). Overall, our results highlight the immunological relevance and clinical potential of splicing modulation.

### Limitations of the study

Although we identified many splicing-derived, potentially immunogenic peptides produced upon exposure to splicing inhibitors,

some of which triggered reactive T cell expansion *in vivo*, it is unclear which are most important for controlling tumor growth. However, because splicing modulation yields such diverse peptides, multiple peptides may contribute. Our work also highlights outstanding questions. For example, does splicing modulation affect CD4<sup>+</sup> T cells and MHC II-presented neoantigens? Are there MHC-independent anti-tumor B cell and antibody responses elicited by neoantigenic proteins on the cell surface? Do cancer-associated mutations in RNA splicing factors (Dvinge et al., 2016) alter the response to checkpoint immunotherapy? Finally, does pharmacologically altering RNA metabolic processes beyond splicing, such as intronic polyadenylation or NMD, affect tumor immunogenicity? Our finding that multiple modes of splicing modulation promote tumor immunogenicity will hopefully motivate further efforts to develop novel means of therapeutically modulating splicing and other RNA metabolic processes.

## STAR★METHODS

Detailed methods are provided in the online version of this paper and include the following:

- KEY RESOURCES TABLE
- RESOURCE AVAILABILITY
  - Lead contact
  - Materials availability
  - Data and code availability
- EXPERIMENTAL MODEL AND SUBJECT DETAILS
  - Mice
  - Cell lines
- METHOD DETAILS
  - Pretreatment with splicing inhibitors
  - *In vivo* tumor challenge
  - Determination of cell growth, Annexin V, and activation marker IC<sub>50</sub> values
  - OT-1 cytotoxicity assay
  - LAMP-1 T cell degranulation assay
  - Generation and use of peptide:H-2K<sup>b</sup> tetramers
  - Intracellular cytokine staining
  - Western blotting
  - Therapeutic treatment with splicing compounds and anti-PD1
  - *In vivo* T cell or NK cell depletion
  - CFSE adoptive T cell transfer and splicing modulator treatment

### Figure 6. Splicing-derived neopeptides are immunogenic *in vivo*

(A) Heatmap representing mean MFI of H-2K<sup>b</sup> from RMA-S assay. Green, immunogenic controls.  
(B) Immunization schema.  
(C) Representative IFN- $\gamma$  ELISpot from CD8<sup>+</sup> T cells upon stimulation with syngeneic peptide-loaded splenocytes. Each row is a peptide used for *in vivo* immunization. Columns, T cells reacted with the indicated stimuli. PMA, phorbol 12-myristate 13-acetate; Iono, ionomycin.  
(D) Spots per 10<sup>5</sup> CD8<sup>+</sup> T cells from IFN- $\gamma$  ELISpot for peptides identified as immunogenic. Bar indicates median. SIINFEKL, positive control. Each dot is one technical replicate.  
(E) Representative IFN- $\gamma$  ELISpot of CD8<sup>+</sup> T cells from immunized mice, following stimulation with syngeneic peptide-loaded splenocytes. Each row is one dose. Columns, T cells reacted with the indicated stimuli. Plots on right quantify numbers of dots per well; each dot is one technical replicate.  
(F) Comparisons of predicted MHC I binding for immunogenic (IFN- $\gamma$  ELISpot-positive) versus nonimmunogenic peptides.  
(G) As (F), but with RMA-S MFIs. For (F) and (G), p from two-sided Wilcoxon rank-sum test.  
See also Figure S7 and Table S7.

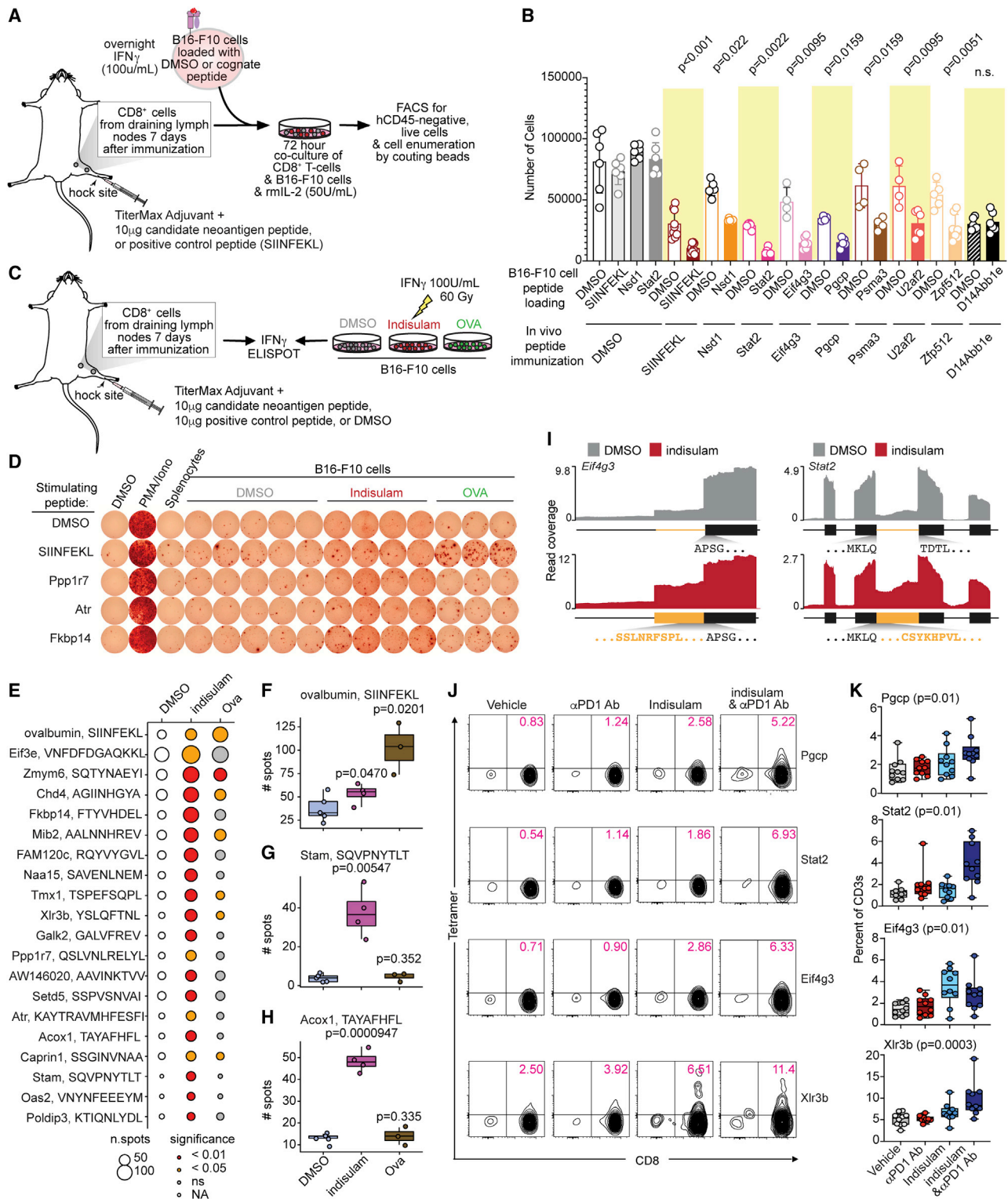


**Figure 7. Splicing-derived neoantigens trigger an endogenous T cell response**

(A) Schema of co-culture of CD8<sup>+</sup> T cells from peptide-immunized C57BL/6 mice with peptide-loaded B16-F10 cells for cytotoxicity.

(B) Bar plot of live B16-F10 cells from (A). Each dot is a technical replicate. p from Wilcoxon rank-sum test.

(C) Schema of CD8<sup>+</sup> T cells from peptide-immunized C57BL/6 mice, stimulated with B16-F10 cells treated with DMSO or indisulam for IFN- $\gamma$  ELISpot.

(legend continued on next page)

- Anti-CD3/CD28 T cell activation
- Mixed leukocyte reaction
- M3434 methylcellulose colony assay
- Intracellular flow cytometry
- Histology
- Cellular fractionation for RNA sequencing
- RNA sequencing
- RNA-seq data analysis
- MHC I immunoprecipitation, peptide purification, and mass spectrometry
- Mass spectrometry
- Proteome creation
- Peptide identification from mass spectrometry data
- Candidate neoepitope identification
- Peptide synthesis
- RMA-S peptide H-2 stabilization assay
- TiterMax immunization
- IFN $\gamma$  ELISpot
- B16-F10 co-culture cytotoxicity assay

● **QUANTIFICATION AND STATISTICAL ANALYSIS**

**SUPPLEMENTAL INFORMATION**

Supplemental information can be found online at <https://doi.org/10.1016/j.cell.2021.05.038>.

**ACKNOWLEDGMENTS**

We thank Phil Gafken and Lisa Jones for mass spectrometry advice. S.X.L. is supported by a Parker Institute for Cancer Immunotherapy (PICI) Bridge Scholar award, the NIH/NCI (K08 CA245242-01), and the Leukemia & Lymphoma Society (5492-20). E.D.N. was supported in part by the NIH/NCI (T32 CA009657). J.D.T. is a Washington Research Foundation postdoctoral fellow. J.D.W. is funded through NIH/NCI Cancer Center (P30 CA008748), Ludwig Collaborative and Swim Across America Laboratory, and PICI. O.A.-W. and R.K.B. were supported by the Edward P. Evans Foundation, NIH/NCI (R01 CA251138), and NIH/NHLBI (R01 HL128239). O.A.-W. is supported in part by the NIH/NCI (R01 CA242020) and Henry and Marilyn Taub Foundation for MDS Research. R.K.B. was supported in part by the NIH/NIDDK (R01 DK103854) and NIH/NHLBI (R01 HL151651). R.K.B. is a scholar of the Leukemia and Lymphoma Society (1344-18). R.E.T. is supported by the NIH/NIGMS (R01 GM123741) and the Walther Cancer Foundation through the Harper Cancer Research Institute at Notre Dame. Computational studies were supported by FHCRC's Scientific Computing Infrastructure (ORIP S10 OD028685).

**AUTHOR CONTRIBUTIONS**

S.X.L., E.D.N., J.D.T., O.A.-W., and R.K.B. designed the study. A.X., C.E., D. Cui, M.S., and H.C. performed drug treatments. E.D.N. and J.D.T. performed proteomic and RNA-seq analyses. S.X.L. and J.D.T. performed analyses of biological data. S.X.L., M.G., D. Cui, C.E., M.S., and H.C. performed peptide immunizations. S.X.L., E.S., and H.M. performed mass spectrometry. S.X.L.

and A.X. performed *in vitro* drug studies. Y.S., J.L., J.J., M.C.R., and R.E.T. generated chemicals. S.X.L., J.D.T., and A.M.G. generated *B2m* KO cells. B.H.D. and J.D.T. analyzed histology. B.R., M.G., D.A.K., B.G., Y.E., S.J.H., A.C., A.G., D.Z., E.W., B.L., H.S., D. Chowell, J.W., T.M., and L.A.D. provided critical reagents and technical advice. S.X.L., E.D.N., J.D.T., O.A.-W., and R.K.B. wrote the manuscript, with input from all authors.

**DECLARATION OF INTERESTS**

O.A.-W. has served as a consultant for H3B Biomedicine, Foundation Medicine, Merck, Prelude Therapeutics, and Janssen, and is on the scientific advisory board of Envisagenics, Pfizer Boulder, and AIChem. O.A.-W. has received prior research funding from Loxo Oncology and H3 Biomedicine unrelated to this work. S.X.L. has served as a consultant (uncompensated) for PTC Therapeutics. B.R. has served as a consultant for Bayer and Roche. D.Z. reports clinical research support to his institution from Astra Zeneca, Plexxikon, and Genentech and personal/consultancy fees from Merck, Synlogic Therapeutics, Tesaro, Bristol Myers Squibb (BMS), Genentech, Xencor, Memgen, Calidi Biotherapeutics, and Agenus. L.A.D. is a member of the board of directors of Personal Genome Diagnostics (PGDx) and Jounce Therapeutics. L.A.D. is a compensated consultant to PGDx, 4Paws (PetDx), Innovatus CP, Se'er, Delfi, Kinnate, and Neophore. L.A.D. is an uncompensated consultant for, but has received clinical trial support from, Merck. L.A.D. holds equity in PGDx, Jounce, Se'er, Delfi, Kinnate, and Neophore and divested equity in Thrive Earlier Detection in 2021. His spouse holds equity in Amgen. J.D.W. is a consultant for Amgen, Apricity, Arsenal IO, Ascentage Pharma, AstraZeneca, Astellas, Boehringer Ingelheim, BMS, Chugai, Dragonfly, F Star, Eli Lilly, Georgiamune, IMVAQ, Merck, Polynoma, Psioxus, Recepta, Trieza, Truvax, Sellas, and Werewolf Therapeutics. J.D.W. has grant/research support from BMS and Sephora. J.D.W. reports equity in Tizona Pharmaceuticals, Imvaq, Beigene, Linneaus, Apricity, Arsenal IO, and Georgiamune. T.M. is an inventor on patents involving the use of anti-PD-1 antibodies. T.M. is a consultant for Immunos Therapeutics and Pfizer. T.M. is a cofounder of and equity holder in IMVAQ. T.M. receives research funding from BMS, Surface Oncology, Kyn Therapeutics, Infinity Pharmaceuticals, Peregrine Pharmaceuticals, Adaptive Biotechnologies, Leap Therapeutics, and Aprea Therapeutics. S.X.L., O.A.-W., and R.K.B. are inventors on a patent application submitted by FHCRC related to this work.

Received: December 9, 2020

Revised: January 26, 2021

Accepted: May 24, 2021

Published: June 24, 2021

**REFERENCES**

- Abelin, J.G., Keskin, D.B., Sarkizova, S., Hartigan, C.R., Zhang, W., Sidney, J., Stevens, J., Lane, W., Zhang, G.L., Eisenhaure, T.M., et al. (2017). Mass Spectrometry Profiling of HLA-Associated Peptidomes in Mono-allelic Cells Enables More Accurate Epitope Prediction. *Immunity* 46, 315–326.
- Bertrand, F., Montfort, A., Marcheteau, E., Imbert, C., Gilhodes, J., Filleron, T., Rochaix, P., Andrieu-Abadie, N., Levade, T., Meyer, N., et al. (2017). TNF $\alpha$  blockade overcomes resistance to anti-PD-1 in experimental melanoma. *Nat. Commun.* 8, 2256.

(D) Representative IFN- $\gamma$  ELISpot from CD8<sup>+</sup> T cells following stimulation with DMSO or indisulam-treated B16-F10 cells, or B16-F10 cells overexpressing ovalbumin. Rows, peptides used for immunization.

(E) Bubble plot of data from (C) and (D); size of bubble indicates number of spots. p from Wilcoxon rank-sum test.

(F–H) Box-and-whisker plots for representative peptides from (E). Each dot is one technical replicate. p from Wilcoxon rank-sum test.

(I) RNA-seq coverage plots demonstrating mis-splicing of *Eif4g3* (left) and *Stat2* (right) upon indisulam exposure and the resulting neoantigenic peptides.

(J) Representative plots of peptide:MHC I tetramer staining of CD8<sup>+</sup> T cells from tumor-draining lymph nodes of B16-F10 tumor-bearing mice treated with vehicle, anti-PD1, indisulam, or the combination and analyzed at day 14, gated on CD3<sup>+</sup> T cells. Each row is one neoantigenic peptide, and columns indicate treatment condition.

(K) Quantification of (J); each dot is one mouse. p from Kruskal-Wallis ANOVA.

See also [Figure S7](#) and [Table S7](#).

- Chan-Penebre, E., Kuplast, K.G., Majer, C.R., Boriack-Sjodin, P.A., Wigle, T.J., Johnston, L.D., Rioux, N., Munchhof, M.J., Jin, L., Jacques, S.L., et al. (2015). A selective inhibitor of PRMT5 with in vivo and in vitro potency in MCL models. *Nat. Chem. Biol.* **11**, 432–437.
- De Bruijn, M.L., Schumacher, T.N., Nieland, J.D., Ploegh, H.L., Kast, W.M., and Melief, C.J. (1991). Peptide loading of empty major histocompatibility complex molecules on RMA-S cells allows the induction of primary cytotoxic T lymphocyte responses. *Eur. J. Immunol.* **21**, 2963–2970.
- De Silva, A.D., Boesteanu, A., Song, R., Nagy, N., Harhaj, E., Harding, C.V., and Joyce, S. (1999). Thermolabile H-2Kb molecules expressed by transporter associated with antigen processing-deficient RMA-S cells are occupied by low-affinity peptides. *J. Immunol.* **163**, 4413–4420.
- Dvinge, H., Ries, R.E., Ilagan, J.O., Stirewalt, D.L., Meshinchi, S., and Bradley, R.K. (2014). Sample processing obscures cancer-specific alterations in leukemic transcriptomes. *Proc. Natl. Acad. Sci. USA* **111**, 16802–16807.
- Dvinge, H., Kim, E., Abdel-Wahab, O., and Bradley, R.K. (2016). RNA splicing factors as oncoproteins and tumour suppressors. *Nat. Rev. Cancer* **16**, 413–430.
- Eram, M.S., Shen, Y., Szweczyk, M., Wu, H., Senisterra, G., Li, F., Butler, K.V., Kaniskan, H.U., Speed, B.A., Dela Seña, C., et al. (2016). A Potent, Selective, and Cell-Active Inhibitor of Human Type I Protein Arginine Methyltransferases. *ACS Chem. Biol.* **11**, 772–781.
- Fedoriw, A., Rajapurkar, S.R., O'Brien, S., Gerhart, S.V., Mitchell, L.H., Adams, N.D., Rioux, N., Lingaraj, T., Ribich, S.A., Pappalardi, M.B., et al. (2019). Antitumor Activity of the Type I PRMT Inhibitor, GSK3368715, Synergizes with PRMT5 Inhibition through MTAP Loss. *Cancer Cell* **36**, 100–114.e25.
- Flicek, P., Ahmed, I., Amode, M.R., Barrell, D., Beal, K., Brent, S., Carvalho-Silva, D., Clapham, P., Coates, G., Fairley, S., et al. (2013). Ensembl 2013. *Nucleic Acids Res.* **41**, D48–D55.
- Fong, J.Y., Pignata, L., Goy, P.A., Kawabata, K.C., Lee, S.C., Koh, C.M., Musiani, D., Massignani, E., Kotini, A.G., Penson, A., et al. (2019). Therapeutic Targeting of RNA Splicing Catalysis through Inhibition of Protein Arginine Methylation. *Cancer Cell* **36**, 194–209.e9.
- Han, T., Goralski, M., Gaskill, N., Capota, E., Kim, J., Ting, T.C., Xie, Y., Williams, N.S., and Nijhawan, D. (2017). Anticancer sulfonamides target splicing by inducing RBM39 degradation via recruitment to DCAF15. *Science* **356**, eaal3755.
- Huber, W., Carey, V.J., Gentleman, R., Anders, S., Carlson, M., Carvalho, B.S., Bravo, H.C., Davis, S., Gatto, L., Girke, T., et al. (2015). Orchestrating high-throughput genomic analysis with Bioconductor. *Nat. Methods* **12**, 115–121.
- Hubert, C.G., Bradley, R.K., Ding, Y., Toledo, C.M., Herman, J., Skutt-Kakaria, K., Girard, E.J., Davison, J., Berndt, J., Corrin, P., et al. (2013). Genome-wide RNAi screens in human brain tumor isolates reveal a novel viability requirement for PHF5A. *Genes Dev.* **27**, 1032–1045.
- Hutchinson, J.N., Ensminger, A.W., Clemson, C.M., Lynch, C.R., Lawrence, J.B., and Chess, A. (2007). A screen for nuclear transcripts identifies two linked noncoding RNAs associated with SC35 splicing domains. *BMC Genomics* **8**, 39.
- Ishihama, Y., Rappsilber, J., and Mann, M. (2006). Modular stop and go extraction tips with stacked disks for parallel and multidimensional Peptide fractionation in proteomics. *J. Proteome Res.* **5**, 988–994.
- Jayasinghe, R.G., Cao, S., Gao, Q., Wendl, M.C., Vo, N.S., Reynolds, S.M., Zhao, Y., Climente-González, H., Chai, S., Wang, F., et al.; Cancer Genome Atlas Research Network (2018). Systematic Analysis of Splice-Site-Creating Mutations in Cancer. *Cell Rep.* **23**, 270–281.e3.
- Jurtz, V., Paul, S., Andreatta, M., Marcatili, P., Peters, B., and Nielsen, M. (2017). NetMHCpan-4.0: Improved Peptide-MHC Class I Interaction Predictions Integrating Eluted Ligand and Peptide Binding Affinity Data. *J. Immunol.* **199**, 3360–3368.
- Kahles, A., Lehmann, K.V., Toussaint, N.C., Hüser, M., Stark, S.G., Sachsenberg, T., Stegle, O., Kohlbacher, O., Sander, C., and Ratsch, G.; Cancer Genome Atlas Research Network (2018). Comprehensive Analysis of Alternative Splicing Across Tumors from 8,705 Patients. *Cancer Cell* **34**, 211–224.e6.
- Katz, Y., Wang, E.T., Airoidi, E.M., and Burge, C.B. (2010). Analysis and design of RNA sequencing experiments for identifying isoform regulation. *Nat. Methods* **7**, 1009–1015.
- Langmead, B., Trapnell, C., Pop, M., and Salzberg, S.L. (2009). Ultrafast and memory-efficient alignment of short DNA sequences to the human genome. *Genome Biol.* **10**, R25.
- Le, D.T., Durham, J.N., Smith, K.N., Wang, H., Bartlett, B.R., Aulakh, L.K., Lu, S., Kemberling, H., Wilt, C., Luber, B.S., et al. (2017). Mismatch repair deficiency predicts response of solid tumors to PD-1 blockade. *Science* **357**, 409–413.
- Lee, S.C., Dvinge, H., Kim, E., Cho, H., Micol, J.B., Chung, Y.R., Durham, B.H., Yoshimi, A., Kim, Y.J., Thomas, M., et al. (2016). Modulation of splicing catalysis for therapeutic targeting of leukemia with mutations in genes encoding spliceosomal proteins. *Nat. Med.* **22**, 672–678.
- Lesterhuis, W.J., Salmons, J., Nowak, A.K., Rozali, E.N., Khong, A., Dick, I.M., Harken, J.A., Robinson, B.W., and Lake, R.A. (2013). Synergistic effect of CTLA-4 blockade and cancer chemotherapy in the induction of anti-tumor immunity. *PLoS ONE* **8**, e61895.
- Li, B., and Dewey, C.N. (2011). RSEM: accurate transcript quantification from RNA-Seq data with or without a reference genome. *BMC Bioinformatics* **12**, 323.
- Li, H., Handsaker, B., Wysoker, A., Fennell, T., Ruan, J., Homer, N., Marth, G., Abecasis, G., and Durbin, R.; 1000 Genome Project Data Processing Subgroup (2009). The Sequence Alignment/Map format and SAMtools. *Bioinformatics* **25**, 2078–2079. <https://doi.org/10.1093/bioinformatics/btp352>.
- Marabelle, A., Fakih, M., Lopez, J., Shah, M., Shapira-Frommer, R., Nakagawa, K., Chung, H.C., Kindler, H.L., Lopez-Martin, J.A., Miller, W.H., Jr., et al. (2020). Association of tumour mutational burden with outcomes in patients with advanced solid tumours treated with pembrolizumab: prospective biomarker analysis of the multicohort, open-label, phase 2 KEYNOTE-158 study. *Lancet Oncol.* **21**, 1353–1365.
- Meyer, L.R., Zweig, A.S., Hinrichs, A.S., Karolchik, D., Kuhn, R.M., Wong, M., Sloan, C.A., Rosenbloom, K.R., Roe, G., Rhead, B., et al. (2013). The UCSC Genome Browser database: extensions and updates 2013. *Nucleic Acids Res.* **41**, D64–D69.
- Murphy, J.P., Konda, P., Kowalewski, D.J., Schuster, H., Clements, D., Kim, Y., Cohen, A.M., Sharif, T., Nielsen, M., Stevanovic, S., et al. (2017). MHC-I Ligand Discovery Using Targeted Database Searches of Mass Spectrometry Data: Implications for T-Cell Immunotherapies. *J. Proteome Res.* **16**, 1806–1816.
- Musiani, D., Bok, J., Massignani, E., Wu, L., Tabaglio, T., Ippolito, M.R., Cuomo, A., Ozbek, U., Zorgati, H., Ghoshdastider, U., et al. (2019). Proteomics profiling of arginine methylation defines PRMT5 substrate specificity. *Sci. Signal.* **12**, eaat8388.
- Na, I.K., Lu, S.X., Yim, N.L., Goldberg, G.L., Tsai, J., Rao, U., Smith, O.M., King, C.G., Suh, D., Hirschhorn-Cymerman, D., et al. (2010). The cytolytic molecules Fas ligand and TRAIL are required for murine thymic graft-versus-host disease. *J. Clin. Invest.* **120**, 343–356.
- O'Donnell, T.J., Rubinsteyn, A., Bonsack, M., Riemer, A.B., Laserson, U., and Hammerbacher, J. (2018). MHCflurry: Open-Source Class I MHC Binding Affinity Prediction. *Cell Syst.* **7**, 129–132.e4.
- Ran, F.A., Hsu, P.D., Wright, J., Agarwala, V., Scott, D.A., and Zhang, F. (2013). Genome engineering using the CRISPR-Cas9 system. *Nat. Protoc.* **8**, 2281–2308.
- Ritz, C., Baty, F., Streibig, J.C., and Gerhard, D. (2015). Dose-Response Analysis Using R. *PLoS ONE* **10**, e0146021.
- Ross, P., Holmes, J.C., Gojanovich, G.S., and Hess, P.R. (2012). A cell-based MHC stabilization assay for the detection of peptide binding to the canine classical class I molecule, DLA-88. *Vet. Immunol. Immunopathol.* **150**, 206–212.
- Schuster, H., Shao, W., Weiss, T., Pedrioli, P.G.A., Roth, P., Weller, M., Campbell, D.S., Deutsch, E.W., Moritz, R.L., Planz, O., et al. (2018). A tissue-based draft map of the murine MHC class I immunopeptidome. *Sci. Data* **5**, 180157.

- Seiler, M., Yoshimi, A., Darman, R., Chan, B., Keaney, G., Thomas, M., Agrawal, A.A., Caleb, B., Csibi, A., Sean, E., et al. (2018). H3B-8800, an orally available small-molecule splicing modulator, induces lethality in spliceosome-mutant cancers. *Nat. Med.* *24*, 497–504.
- Sellin, M., Mack, R., Rhodes, M.C., Zhang, L., Wei, W., Breslin, P., Berg, S., Huang, S., Taylor, R., and Zhang, J. (2019). The Splicing Modulator GEX1A Exhibits Potent Anti-Leukemic Activity Both in Vitro and In Vivo through Inducing an MCL1 Splice-Switch in Pre-Clinical Models of Acute Myeloid Leukemia. *Blood* *134*, 2666.
- Sha, D., Jin, Z., Budczies, J., Kluck, K., Stenzinger, A., and Sinicrope, F.A. (2020). Tumor Mutational Burden as a Predictive Biomarker in Solid Tumors. *Cancer Discov.* *10*, 1808–1825.
- Smart, A.C., Margolis, C.A., Pimentel, H., He, M.X., Miao, D., Adeegbe, D., Fugmann, T., Wong, K.K., and Van Allen, E.M. (2018). Intron retention is a source of neoepitopes in cancer. *Nat. Biotechnol.* *36*, 1056–1058.
- Thomas, J.D., Polaski, J.T., Feng, Q., De Neef, E.J., Hoppe, E.R., McSharry, M.V., Pangallo, J., Gabel, A.M., Belleville, A.E., Watson, J., et al. (2020). RNA isoform screens uncover the essentiality and tumor-suppressor activity of ultraconserved poison exons. *Nat. Genet.* *52*, 84–94.
- Trapnell, C., Pachter, L., and Salzberg, S.L. (2009). TopHat: discovering splice junctions with RNA-Seq. *Bioinformatics* *25*, 1105–1111.
- Wagenmakers, E.J., Lodewyckx, T., Kuriyal, H., and Grasman, R. (2010). Bayesian hypothesis testing for psychologists: a tutorial on the Savage-Dickey method. *Cognit. Psychol.* *60*, 158–189.
- Wang, E., Lu, S.X., Pastore, A., Chen, X., Imig, J., Chun-Wei Lee, S., Hockemeyer, K., Ghebrecristos, Y.E., Yoshimi, A., Inoue, D., et al. (2019). Targeting an RNA-Binding Protein Network in Acute Myeloid Leukemia. *Cancer Cell* *35*, 369–384.e7.
- Wells, D.K., van Buuren, M.M., Dang, K.K., Hubbard-Lucey, V.M., Sheehan, K.C.F., Campbell, K.M., Lamb, A., Ward, J.P., Sidney, J., Blazquez, A.B., et al.; Tumor Neoantigen Selection Alliance (2020). Key Parameters of Tumor Epitope Immunogenicity Revealed Through a Consortium Approach Improve Neoantigen Prediction. *Cell* *183*, 818–834.e13.
- Wickham, H., Averick, M., Bryan, J., Chang, W., D’Agostino McGowan, L., Francois, R., Grolemund, G., Hayes, A., Henry, L., Hester, J., et al. (2019). Welcome to the Tidyverse. *The Journal of Open Source Software*. <https://doi.org/10.21105/joss.01686>.
- Yadav, M., Jhunjhunwala, S., Phung, Q.T., Lupardus, P., Tanguay, J., Bum-baca, S., Franci, C., Cheung, T.K., Fritsche, J., Weinschenk, T., et al. (2014). Predicting immunogenic tumour mutations by combining mass spectrometry and exome sequencing. *Nature* *515*, 572–576.
- Yokoi, A., Kotake, Y., Takahashi, K., Kadowaki, T., Matsumoto, Y., Minoshima, Y., Sugi, N.H., Sagane, K., Hamaguchi, M., Iwata, M., and Mizui, Y. (2011). Biological validation that SF3b is a target of the antitumor macrolide pladienolide. *FEBS J.* *278*, 4870–4880.
- Zhou, Z., Luo, M.J., Straesser, K., Katahira, J., Hurt, E., and Reed, R. (2000). The protein Aly links pre-messenger-RNA splicing to nuclear export in metazoans. *Nature* *407*, 401–405.

STAR★METHODS

KEY RESOURCES TABLE

REAGENT or RESOURCE	SOURCE	IDENTIFIER
<b>Antibodies</b>		
Anti PD1 for <i>in vivo</i> administration, clone RMP1-14	BioXCell	Cat#BE0146; RRID:AB_10949053
Anti CD8 for <i>in vivo</i> administration, clone 2.43	BioXCell	Cat#BE0061; RRID:AB_1125541
Anti CD4 for <i>in vivo</i> administration, clone GK1.5	BioXCell	Cat#BE0003-1; RRID:AB_1107636
Anti NK1.1 for <i>in vivo</i> administration, clone PK136	BioXCell	Cat#BE0036; RRID:AB_1107737
Anti H-2D <sup>b</sup> for MHC IP, clone B22-249.R1	CedarLane Labs	Cat#CL9001AP; RRID:AB_10548100
Anti H-2K <sup>b</sup> for MHC IP, clone Y-3	BioXCell	Cat#BE0172; RRID:AB_10949300
Anti H-2K <sup>D</sup> for flow cytometry, clone AF6-88.5	BioLegend	Cat#116508; RRID:AB_313735
Anti H-2D <sup>b</sup> for flow cytometry, clone KH95	BioLegend	Cat#111504; RRID:AB_313509
Anti H-2D <sup>b</sup> /H-2K <sup>b</sup> for flow cytometry, clone 28-8-6	BioLegend	Cat#114606; RRID:AB_313597
Anti-PDL1 for flow cytometry, clone 10F.9G2	BioLegend	Cat#124308; RRID:AB_2073556
Anti-PD1 for flow cytometry, clone 29F.1A12	BioLegend	Cat#135206; RRID:AB_1877231
Anti CD3 for flow cytometry, clone 145-2C11	BioLegend	Cat#100304; RRID:AB_312669
Anti CD4 for flow cytometry, clone RM4-5	BioLegend	Cat#100552; RRID:AB_2563053
Anti CD8 for flow cytometry, clone 53-5.8	BioLegend	Cat#140416; RRID:AB_2564385
Anti CD8 for tetramer staining, clone KT15	MBL International	Cat#D271-A64; RRID:AB_10794611
Anti CD25 for flow cytometry, clone PC61	BioLegend	Cat#102049; RRID:AB_2564130
Anti CD44 for flow cytometry, clone IM7	BioLegend	Cat#103026; RRID:AB_493713
Anti CD45 for flow cytometry, clone 30-F11	BioLegend	Cat#103140; RRID:AB_2562342
Anti CD45.1 for flow cytometry, clone A20	BioLegend	Cat#110738; RRID:AB_2562565
Anti CD45.2 for flow cytometry, clone 104	BioLegend	Cat#109814; RRID:AB_389211
Anti CD62L for flow cytometry, clone MEL-14	BioLegend	Cat#104432; RRID:AB_2285839
Anti CD127 for flow cytometry, clone A7R34	BioLegend	Cat#135006; RRID:AB_2126118
Anti CTLA4 for flow cytometry, clone UC10-4B9	BioLegend	Cat#106310; RRID:AB_2087653
Anti LAG3 for flow cytometry, clone C9B7W	BioLegend	Cat#125208; RRID:AB_2133343
Anti TIM-3 for flow cytometry, clone B8.2C12	BioLegend	Cat#134008; RRID:AB_2562998
Anti TER119 for flow cytometry, clone TER-119	BioLegend	Cat#116223; RRID:AB_2137788
Anti CD107a (LAMP-1) for flow cytometry, clone 1D4B	BioLegend	Cat#121612; RRID:AB_2134487
Anti TNFalpha for flow cytometry, clone MP6-XT22	BD Biosciences	Cat#554419; RRID:AB_395380
Anti IFNgamma for flow cytometry, clone XMG1.2	BD Biosciences	Cat#554413; RRID:AB_398551

(Continued on next page)

**Continued**

REAGENT or RESOURCE	SOURCE	IDENTIFIER
Anti IL-2 for flow cytometry, clone JES6-5H4	BD Biosciences	Cat#554427; RRID:AB_395385
Anti Nkp46 antibody for flow cytometry, clone 29A1.4	BioLegend	Cat#137621; RRID:AB_2563289
Annexin V	BioLegend	Cat#640941
Anti RBM39 for western blotting, polyclonal	Atlas Antibodies	Cat#HPA001591; RRID:AB_1079749
Anti ADMA for western blotting, polyclonal	Cell Signaling Tech.	Cat#13222; RRID:AB_2714013
Anti SDMA for western blotting, polyclonal	Cell Signaling Tech.	Cat#13522; RRID:AB_2665370
Anti CD3 for T cell stimulation, clone 145-2C11	Biolegend	Cat#100302; RRID:AB_312667
Anti CD28 for T cell stimulation, clone 37.51	Biolegend	Cat#102102; RRID:AB_312867
Anti CD5 beads for T cell selection	Miltenyi Biotec	Cat#130-049-301
Anti CD8 beads for T cell selection	Miltenyi Biotec	Cat#130-117-044
CountBright Absolute Counting Beads	ThermoFisher	Cat#C36950

**Chemicals, peptides, and recombinant proteins**

MS-023	Tocris	Cat#5713
Indisulam	Millipore Sigma	Cat#SML1225-25MG
EPZ015666	Millipore Sigma	Cat#SML1421-25MG
Pladienolide B	Tocris	Cat#6070
Herboxidiene (GEX1A)	Cayman Chemicals	Cat#25136
TiterMax Classic	TiterMax Co.	Cat#R10
LPS from <i>E. coli</i> 026:B6	eBioscience	Cat#00-4976-93
Candidate splicing-derived neoantigenic peptides	Genscript	This paper; <a href="#">Table S7</a>
Recombinant mouse IL-2	Peprotech	Cat#212-12
Recombinant mouse IL-3	R&D Systems	Cat#403-ML
Recombinant mouse IFN $\gamma$	Peprotech	Cat#315-05
Recombinant mouse FLT3 ligand	Peprotech	Cat#250-31L
10X Collagenase/hyaluronidase in DMEM	Stemcell Tech.	Cat#07912
DNase I recombinant, RNase-free	Millipore-Sigma	Cat#4716728001
Captisol (SBE- $\beta$ -CD (Synonyms: Sulfobutylether- $\beta$ -Cyclodextrin)	MedChemExpress	Cat# HY-17031
(2-Hydroxypropyl)- $\beta$ -cyclodextrin	MilliporeSigma	Cat# H107-100G
N-Methyl-2-Pyrrolidone	MilliporeSigma	Cat# 494496-1L
Dimethyl sulfoxide	MilliporeSigma	Cat# D4540-100ML
Polyethylene glycol 400	MilliporeSigma	Cat#91893-1L-F
GolgiPlug (Brefeldin A)	BD Biosciences	Cat#555029
GolgiStop (Monensin)	BD Biosciences	Cat#554724
Ionomycin	Cell Signaling Tech.	Cat#9995S
12-O-Tetradecanoylphorbol-13-Acetate (PMA)	Cell Signaling Tech.	Cat#4174S
CellTrace CFSE Cell Proliferation Kit	Fisher Scientific	Cat#C34554
Tween 20 (50% solution)	ThermoFisher	Cat#3005
Cell Dissociation Buffer, enzyme-free, HBSS	ThermoFisher	Cat#13150016

**Critical commercial assays**

Subcellular Fractionation Kit for RNA	Active Motif	Cat#25501
Anti mouse-IFN $\gamma$ ELISpot	BD Biosciences	Cat#551083
AEC substrate set	BD Biosciences	Cat#551951
CellTiter Glo	Promega	Cat#G7573

(Continued on next page)

**Continued**

REAGENT or RESOURCE	SOURCE	IDENTIFIER
QuickSwitch H-2Kb Tetramer Kit	MBL International	Cat#TB-7400-K1
MethoCult GF M3434	StemCell Tech.	Cat#03434
<b>Deposited data</b>		
RNA-seq data generated for this study	NCBI Gene Expression Omnibus	GEO: GSE162818
<b>Experimental models: Cell lines</b>		
MC38	Kerafast	ENH204-FP
B16-F10	ATCC	CRL-6475
CT26	ATCC	CRL-2638
MB49	MilliporeSigma	SCC148
LLC (LL/2)	ATCC	CRL-1642
A375	ATCC	CRL-1619
501MEL	Generated in laboratory of J.W. & T.M.	N/A
SKMEL-239	Generated in laboratory of J.W. & T.M.	N/A
RMA-S	N/A	N/A
<b>Experimental models: Organisms/strains</b>		
B6.129P2-B2m <sup>tm1Unc</sup> /DcrJ (Beta2 microglobulin KO)	Jackson Laboratories	002087
C57BL/6-Tg(TcraTcrb)1100Mjb/J (OT-I)	Jackson Laboratories	003831
B6.SJL-Ptprc <sup>a</sup> Pepc <sup>b</sup> /BoyJ (B6 CD45.1)	Jackson Laboratories	002014
B6.Cg-Rag2 <sup>tm1.1Cgn</sup> /J (RAG2 KO)	Jackson Laboratories	008449
<b>Oligonucleotides</b>		
AGTATACTACGCCACCCACCGG	This study	mB2Msg#1
TCACGCCACCCACCGGAGAAATGG	This study	mB2Msg#2
GGCGTATGTATCAGTCTCAGTGG	This study	mB2Msg#3
TCGGCTTCCATTCTCCGGTGGG	This study	mB2Msg#4
CACCGGAGCGCACCATCTTCTTCA	This study	NTsgRNA
AAAAAGTCCGCGATTACGTC	This study	pgRNA.non-targeting.gRNA1
ACCCATCCCGCGTCCGAGA	N/A	pgRNA.non-targeting.gRNA2
GAGGGGTTTCTGAGGGCCAC	This study	pgRNA.B2m.gRNA1_
AGTATACTACGCCACCCAC	This study	pgRNA.B2m.gRNA2
<b>Recombinant DNA</b>		
pLenti-Cas9-blast	Addgene	52962
LentiGuide-Puro	Addgene	52963
pSpCas9(BB)-2A-Puro (PX459) V2.0	Addgene	62988
<b>Software and algorithms</b>		
FlowJo	BD Biosciences	V10
GraphPad Prism	GraphPad Software	V8
Bowtie v1.0.0	<a href="#">Langmead et al., 2009</a>	<a href="https://github.com/BenLangmead/bowtie/">https://github.com/BenLangmead/bowtie/</a> ; RRID: SCR_005476
RSEM v.1.2.4	<a href="#">Li and Dewey, 2011</a>	<a href="https://deweylab.github.io/RSEM/">https://deweylab.github.io/RSEM/</a> ; RRID: SCR_013027
TopHat v2.0.8b	<a href="#">Trapnell et al., 2009</a>	<a href="https://ccb.jhu.edu/software/tophat/index.shtml">https://ccb.jhu.edu/software/tophat/index.shtml</a> ; RRID: SCR_013035
MISO v2.0	<a href="#">Katz et al., 2010</a>	<a href="https://www.genes.mit.edu/burgelab/miso/">https://www.genes.mit.edu/burgelab/miso/</a> ; RRID: SCR_003124
Samtools v1.3.1	<a href="#">Li et al., 2009</a>	<a href="https://www.htslib.org">https://www.htslib.org</a> ; RRID: SCR_002105
Bioconductor	<a href="#">Huber et al., 2015</a>	<a href="https://www.bioconductor.org">https://www.bioconductor.org</a> ; RRID: SCR_006442

(Continued on next page)

**Continued**

REAGENT or RESOURCE	SOURCE	IDENTIFIER
tidyverse	Wickham et al., 2019	CRAN: tidyverse; RRID: SCR_019186
Proteome Discoverer v2.4.1.15	ThermoFisher	OPTON-30945; RRID:SCR_014477

**RESOURCE AVAILABILITY**

**Lead contact**

Omar Abdel-Wahab; [abdelwao@mskcc.org](mailto:abdelwao@mskcc.org)

**Materials availability**

Unique reagents were not generated for this study.

**Data and code availability**

RNA-seq data generated as part of this study were deposited at the Gene Expression Omnibus (accession GSE162818). Software RRIDs (also available in the [Key Resources Table](#)) are: Bowtie RRID: SCR\_005476, RSEM RRID: SCR\_013027, TopHat RRID: SCR\_013035, MISO RRID: SCR\_003124, Samtools RRID: SCR\_002105, Bioconductor RRID: SCR\_006442, dplyr RRID: SCR016708, ggplot2 RRID: SCR\_014601, Proteome Discoverer RRID: SCR\_014477.

**EXPERIMENTAL MODEL AND SUBJECT DETAILS**

**Mice**

All *in vivo* experiments were approved by the Institutional Animal Care and Use Committees (IACUC) of Memorial Sloan Kettering Cancer Center and/or Fred Hutchinson Cancer Research Center and conducted in accordance with ARRIVE guidelines. All animals were housed in the respective specific pathogen-free (SPF) barrier facilities and maintained under standard husbandry conditions. B6(Cg)-Rag2tm1.1Cgn/J (RAG2 KO) mice, C57BL/6-Tg (TcratTcrb)1100Mjb/J (OT-1) mice and B6.129P2-B2mtm1Unc/DcrJ (B2M KO) mice were obtained from Jackson Laboratories (Cat. 008440, 003831, 002087 respectively). C57BL/6 mice, congenic B6.SJL-*Ptprc*<sup>a</sup> *Peprc*<sup>b</sup>/BoyJ (CD45.1) mice, BALB/c and LP/J mice were also obtained from Jackson Laboratories (Cat. 000664, 002014, 000651 and 000676). CD45.1, RAG2 KO, B2M KO, and OT-1 mice are all fully backcrossed onto the C57BL/6 genetic background. Unless otherwise noted in the text, females from 6–8 weeks old were used for all experiments. Animals within each genotype and treatment condition were randomly allocated to experimental groups; we did not exclude any allocated animals from our analyses. We minimized nuisance variables associated with the vivarium by checking on each cage of animals at least daily, and randomizing the location of cages when animals were placed back in their housing. Multiple authors (S.X.L., D.C., H.C., M.S., C.E.) were assigned to each experiment to minimize bias due to animal handling techniques. Blinding was not feasible for animal tumor challenge, drug treatment, or tumor measurements as the same authors performed all of the above. Animal group sample sizes (indicated in Figure Legends) were determined based on prior published literature on the same tumor models, with differences in tumor growth as the primary outcome measure. Individual study designs, outcome measures and corresponding statistical tests for animal experiments and *ex vivo* analyses of primary murine tissues are otherwise described in the text and figure legends.

**Cell lines**

B16-F10, CT26.WT (CT26), and LLC cells were obtained from ATCC (Cat. CRL-6475, CRL-2638, and CRL-1642 respectively). MB49 cells were obtained from MilliporeSigma (Cat. SCC148, Burlington, MA); MC38 cells were obtained from Kerfast (Cat. ENH204-FP, Boston, MA). B16-F10 and MC38 cells expressing chicken ovalbumin (B16ova and MC38ova) were a kind gift of Jeff Ravetch (Rockefeller University, New York, NY). To generate  $\beta_2$  microglobulin-deficient cell lines for *in vitro* experiments, four candidate sgRNAs for mouse  $\beta_2$  microglobulin (#1 AGTATACTCAGCCACCCACCGG, #2 TCACGCCACCCACCGGAGAAATGG, #3 GGCGTATGTATCAGTCTCAGTGG, #4 TCGGCTTCCCATTCTCCGGTGGG) or non-targeting control (GGAGCGCACCATCTTCTTCA) were cloned into pSpCas9(BB)-2A-Puro (PX459) as previously described (Ran et al., 2013) and used to engineer deficient MC38, B16-F10, and CT26 cell lines via transfection using XtremeGene 9 reagent as per manufacturer's instructions (MilliporeSigma Cat. 6365809001) followed by puromycin selection at 10  $\mu$ g/mL for three days. Polyclonal cell populations were obtained by flow sorting for H-2K<sup>b</sup>/D<sup>b</sup> and  $\beta_2$  microglobulin double-negative cells, and gene knockout further confirmed by stimulating a culture of these sorted cells for 48 hours with 10U/mL mouse IFN $\gamma$  and analyzing for the same markers. For *in vivo* experiments, lentiCas9-Blast was used to generate Cas9-expressing B16-F10 cells. *B2m* gRNAs (GAGGGTTTCTGAGGGCCAC, AGTATACTCAGCCACCAC) and non-targeting control gRNAs (AAAAAGTCCGCGATTACGTC, ACCCATCCCCGCGTCCGAGA) were cloned into lentiGuide-Puro and introduced into Cas9-expressing B16-F10 cells via lentiviral transduction as previously described (Thomas et al., 2020) and underwent similar selection. PX459, lentiCas9-blast, and lentiGuide-Puro were kind gifts of Feng Zhang (Addgene Cat. 62988, 52962, 52963).

## METHOD DETAILS

### Pretreatment with splicing inhibitors

Unless otherwise specified, cell lines were treated with splicing inhibitors at the indicated concentrations for 96 hours *in vitro*, harvested and washed three times with PBS in excess to remove all drug, and then used for downstream analyses and/or subsequent studies, including phenotyping, RNA-seq analyses, continued growth *in vitro*, or tumor challenge *in vivo* into syngeneic animals.

### *In vivo* tumor challenge

Unless otherwise specified, syngeneic B6 or BALB/c mice were engrafted subcutaneously on bilateral flanks with MC38, B16-F10, CT26 or LLC tumor cells at the following doses: MC38  $10^6$  cells, B16-F10  $0.5 \times 10^6$  cells, CT26  $0.25 \times 10^6$  cells, LLC  $0.25 \times 10^6$  cells. Tumors were measured serially twice or three times weekly and tumor volumes were estimated by length x width x height. Animals were monitored daily for survival and weighed twice weekly. Experimental endpoints mandating euthanasia were approved by the IACUC and included: animal lethargy, severe kyphosis or evidence of pain, difficulty with ambulation or feeding, tumor ulceration > 1 cm or bleeding tumor, evidence of infected tumor, tumor volumes exceeding  $2.5 \text{ cm}^3$ , or animal total body weight loss > 10% from baseline.

### Determination of cell growth, Annexin V, and activation marker IC<sub>50</sub> values

Cell lines were grown with half- $\log_{10}$  concentrations of the indicated drug in 4 to 8 technical replicates under standard conditions until the control condition (DMSO or vehicle) was confluent by microscopy. For tumor cell lines, viable cells were quantified via the CellTiter-Glo® assay (Promega Cat. G7573) as per manufacturer instructions. For the *ex vivo* proliferation of T cells, viable cells were instead quantified via flow cytometry using counting beads. The percentage or number of viable cells with drug treatment was calculated relative to DMSO control (as 100%). These data were  $\log_{10}$  transformed and a three-parameter nonlinear fit of  $\log(\text{inhibitor})$  versus response was performed in GraphPad Prism v9.0 (GraphPad Software, San Diego, CA) to determine IC<sub>50</sub> values. For absolute cell number, Annexin V+, CD25+, and PD1+ flow cytometry data presented in [Figure S4](#), dose-response models and IC<sub>50</sub> values were computed using the R language's drc package ([Ritz et al., 2015](#)).

### OT-1 cytotoxicity assay

Bulk splenocytes from OT-1 animals were cultured for three days with 100 U/mL murine IL-2 and 100  $\mu\text{g}/\text{mL}$  SIINFEKL peptide to activate CD8<sup>+</sup> T cells. Cultures were subsequently washed thoroughly to remove ova peptide and rested for at least 24 hours prior to use. OT-1 cells were passaged in T cell media with 50 U/mL IL-2 for no more than seven days from animal sacrifice prior to use. For the cytotoxicity assay, tumor cells alone or OT-1 + tumor cells (1:1 ratio) were incubated in T cell media for 18 hours under standard conditions with the indicated concentrations of splicing drugs and analyzed by flow cytometry to quantify killing. OT-1 cells and other hematopoietic cells were excluded with the use of CD45, CD3, and CD8 staining. Tumor cell viability was measured using DAPI.

### LAMP-1 T cell degranulation assay

OT-1 cells were generated as described for the cytotoxicity assay and incubated with ovalbumin-expressing tumor cell lines (pretreated overnight with IFN $\gamma$  100U/mL to upregulate cell-surface MHC I) in the presence of DMSO or varying concentrations of splicing modulator drugs as indicated, in the presence of LAMP-1 antibody for 5-6 hours under standard incubator conditions. After the first hour of incubation, BD GolgiPlug (brefeldin A) and BD GolgiStop (monensin) was added at 1:1,1000 + 1:1,500 respectively into cells. At the end of incubation, cells were washed and stained for cell surface markers prior to standard flow cytometry.

### Generation and use of peptide:H-2K<sup>b</sup> tetramers

Peptide:MHC I tetramers with neoantigenic peptides and murine H-2K<sup>b</sup> were generated using the QuickSwitch Quant Tetramer Kit-PE (Cat. TB-7400-K1, MBL International) per manufacturer instructions. Briefly, 10  $\mu\text{g}$  of peptide together with 50  $\mu\text{L}$  of the tetramer reagent and 1  $\mu\text{L}$  of peptide exchange factor were incubated at room temperature for 5-6 hours and used to stain cell populations of interest. Clone KT15 of an anti-CD8 antibody (Cat. D271-A64, MBL International) was used to identify CD8<sup>+</sup> T cells of interest as this clone does not interfere with tetramer binding.

### Intracellular cytokine staining

OT-1 cells were prepared and incubated with ovalbumin-expressing tumors as described above in the LAMP-1 assay. For some experiments OT-1 cells were instead left unstimulated (DMSO) or treated with PMA 1  $\mu\text{g}/\text{mL}$  + ionomycin 1  $\mu\text{M}$  as a supraphysiologic stimulus. In all cases, T cells underwent a 5-6 hour incubation period in the presence of DMSO or splicing modulators at the indicated concentrations, and with brefeldin A and monensin present for the entire duration. Cells were subsequently washed, stained for surface markers, and then fixed/permeabilized for intracellular staining of the indicated cytokines according to manufacturer instructions (BD Biosciences).

### Western blotting

Western blotting was performed as per standard techniques. Anti-RBM39 (Atlas Antibodies, Cat. HPA001591 or Bethyl laboratories, Cat. A300-291A) were used to detect RBM39 degradation. ADMA and SDMA levels were determined using antibodies from Cell

Signaling Technologies (Cat. 13222S and Cat. 13522S). Actin antibody (clone AC-15) was obtained from MilliporeSigma (Cat. A5441-.2ML). Densitometry of RBM39 and actin loading control was performed using ImageJ software in order to calculate RBM39 degradation  $IC_{50}$  values.

### Therapeutic treatment with splicing compounds and anti-PD1

Animals were subcutaneously engrafted on bilateral flanks with tumor cells (MC38  $1 \times 10^6$ , B16-F10  $0.5 \times 10^6$  and LLC  $0.25 \times 10^6$  cells unless otherwise specified) on day 0, and treated continuously with splicing inhibitors (MS-023 50 mg/kg i.p., indisulam 25 mg/kg i.v. or vehicle) daily for 5 of 7 weekly days starting from day +3 of tumor challenge. Indisulam was obtained from MilliporeSigma (Cat. SML1225-25MG) and MS-023 in sufficient quantities for *in vivo* studies was synthesized by the authors as previously described (Eram et al., 2016). For *in vivo* formulation, indisulam was dissolved in sterile DMSO at 50 mg/mL and this was combined in a 1:20 ratio with 15% 2-Hydroxypropyl- $\beta$ -cyclodextrin (Sigma. Cat. H107-100G) in sterile water (w/v) and filtered through a 0.45  $\mu$ M filter to yield a final solution of 2.5 mg/mL. For *in vivo* formulation, 62.5 mg of MS-023 was dissolved in 563  $\mu$ L of 1-methyl-2-pyrrolidinone (NMP, Sigma. 328634-1L), diluted with 2.257 mL of 20% Captisol in sterile water (w/v, SelleckChem Cat. S4592) and further combined with 2.257 mg of polyethylene glycol 400 (PEG-400, Sigma Cat. PX1286B-2), and 6.21 mL of PBS, mixed by vortexing and sterile filtered to yield a solution of 5.5 mg/mL. Mice were weighed weekly for weight-based drug dosing. Animals were treated with 250  $\mu$ g of anti-PD1 flat dose (clone RMP1-14, BioXCell Cat. BE0146) or PBS i.p. starting on day +7 and twice weekly thereafter for a total of five doses.

### In vivo T cell or NK cell depletion

For depleting T cells, mice were treated with simultaneous anti-CD4 (clone GK1.5, BioXCell Cat. BE0003-1) together with anti-CD8 (clone 2.43, BioXCell Cat. BE0061) versus PBS control, at days -7, -4, +4, and +7 relative to tumor challenge on day 0. Each depleting antibody was administered i.p. at 0.5 mg per dose.  $0.5 \times 10^6$  B16-F10 which were treated *in vitro* with indisulam at 1  $\mu$ M or DMSO for 96 hours were engrafted subcutaneously on the flanks of animals receiving T cell depletion or PBS control. For NK cell depletion, an identical experimental schedule and dose using clone PK136 (BioXCell Cat. BE0036) was utilized. To verify T cell depletion, CD4 clone H129.19 (Biolegend Cat. 130310), CD8 clone 53-5.8 (Biolegend Cat. 140410) were used. NKp46 (Biolegend Cat. 137608) was used to verify NK cell depletion.

### CFSE adoptive T cell transfer and splicing modulator treatment

Splenic T cells were obtained from naive B6 or CD45.1 donors by CD5 positive selection (Miltenyi Biotec, Cat. 130-049-301), labeled with CellTrace CFSE (ThermoFisher Cat. C34570) at 10  $\mu$ M, and adoptively transferred by tail vein injection into lethally irradiated B6, BALB/c, or LP/J recipients, with  $10^7$  labeled donor T cells transferred per recipient. All recipients were irradiated on day -1 prior to adoptive T cell transfer with 7 Gy as a single fraction and continuously received splicing inhibitor drugs or vehicle control at the indicated doses, from day -1 until day of sacrifice, with the initial dose of drug at least 4 hours after lethal irradiation. Recipients were treated with each splicing modulatory compound at doses used in prior studies that result in target engagement *in vivo* (Fong et al., 2019; Wang et al., 2019). Indisulam and MS-023 were solubilized for *in vivo* administration and animals were treated daily as above. Pladienolide B (Tocris, Cat. 6070) and GEX1A (Cayman Chemicals, Cat. 25136) were both dissolved in vehicle (10% ethanol and 4% Tween-80 in sterile PBS) and administered i.p., with pladienolide B dosed at 10 mg/kg every other day, and GEX1A dosed at 1.25 mg/kg every four days. For *in vivo* use, EPZ015666 was dissolved in DMSO and solubilized in 0.5% methylcellulose in water to 20 mg/mL; animals were treated daily with 200mg/kg by oral gavage.

### Anti-CD3/CD28 T cell activation

Plates were coated with 10  $\mu$ g/mL anti-CD3 (clone 145-2C11, Biolegend Cat. 100302) and 2  $\mu$ g/mL anti-CD28 (clone 37.51, Biolegend Cat. 102102) in PBS overnight at 4°C and washed twice with cold PBS prior to use. CFSE-labeled CD5-selected splenic T cells from naive C57BL/6J mice were obtained identically as for adoptive cell transfer, and  $5 \times 10^4$  cells incubated with coated plates in the presence of splicing inhibitor drugs at the indicated concentrations, followed by analysis by standard flow cytometry on day 3. Of note, for RNA-seq analyses, T cells were not labeled with CFSE, and underwent activation for 4 days (96 hours) in the presence of various splicing modulator drugs to harmonize experimental conditions with RNA-seq analyses of tumors treated with splicing inhibitors. For the RNA-seq experiments only, T cells in all conditions were also incubated with IL-2 at 50U/mL to maximize viability and yield.

### Mixed leukocyte reaction

RBC lysed bone marrow obtained from the femurs and tibias of C57BL/6 or  $\beta_2$  microglobulin deficient mice (Jackson Laboratories Cat. 2087) were cultured with mouse IL-3 (PeproTech Cat. 213-13) and mouse FLT3 ligand (PeproTech Cat. 250-31L) both at 10 ng/mL each in RPMI + 10% FCS for 7 days to generate bone marrow derived dendritic cells. Separately,  $10^7$  MC38 treated with splicing inhibitors versus DMSO or expressing chicken ovalbumin were harvested, washed and resuspended in sterile PBS, and subjected to five cycles of rapid freeze-thaw (alternating between 37°C and dry ice/acetone) to generate a cell lysate. After brief centrifugation at 100xg, the soluble fraction in PBS was added to bone marrow derived DCs and left to incubate overnight for antigen phagocytosis in the presence of LPS (ThermoFisher Cat. 00-4976-93). DCs were subsequently washed three times to remove cell-free lysates and

LPS and incubated in a 1:1 ratio with CFSE-labeled B6 splenic T cells ( $10^5$  stimulators with  $10^5$  responders) as described above. The MLR was analyzed at day 5 by flow cytometry.

### M3434 methylcellulose colony assay

25,000 red blood cell-lysed bone marrow mononuclear cells from C57BL/6 mice were plated in duplicates or triplicates in each well of a non tissue-culture treated 6 well plate with M3434 methylcellulose media in the presence of splicing drugs at the indicated concentrations as per manufacturer's instructions (StemCell Technologies, Cat. 03434) and incubated for seven days prior to quantification of colonies by manual microscopy.

### Intracellular flow cytometry

Cells were fixed with 2.1% formaldehyde in PBS for 10 minutes at 37°C, washed and permeabilized with ice-cold 90% methanol for 30 minutes, and washed prior to staining. If required, cell surface staining was performed after fixation but prior to permeabilization. For some experiments, intracellular staining was performed using the eBioscience Foxp3 transcription factor staining buffer set (ThermoFisher Cat. 00-5523-00) or reagents for intracellular cytokine staining (BD Cytotfix/Cytoperm, Cat. 554714, and BD Perm/Wash, Cat. 554723) as per manufacturer's instructions.

### Histology

Animal tissues were fixed in 4% paraformaldehyde, decalcified (for bone), dehydrated and paraffin embedded. Blocks were sectioned and stained with hematoxylin and eosin or anti-CD8. Images were acquired using an Axio Observer A1 microscope (Carl Zeiss, Oberkochen, Germany) or scanned using an Aperio AT slide scanner (Leica Biosystems, Buffalo Grove, IL). Automated quantification of infiltrating CD8<sup>+</sup> T cells was performed using HALO software (Indica labs, Albuquerque, NM). Pathologic evaluation of immune-related tissue toxicities was performed in a blinded fashion by one of the authors who is a trained pathologist (Ben Durham, MD).

### Cellular fractionation for RNA sequencing

Nuclear and cytoplasmic cellular fractions were isolated from B16-F10 cells using reagents from Active Motif (Cat. 25501) as per manufacturers' instructions, with the exception of RNA isolation and purification from each fraction using the QIAgen RNeasy Mini kit.

### RNA sequencing

Bulk lung and colon were homogenized using a QIAGEN TissueRuptor. For all tissues and cell types, RNA was extracted using an RNeasy kit (QIAGEN, Frederick, MD) and quantified using a NanoDrop 8000 (ThermoFisher Scientific). A minimum of 500 ng of high-quality RNA (as determined by Agilent Bioanalyzer) per sample or replicate was used for library preparation. Poly(A)-selected, strand-specific (dUTP method) Illumina libraries were prepared with a modified TruSeq protocol and sequenced on the Illumina Hi-Seq 2000 (~100M 2x101 bp paired-end reads per sample or replicate).

### RNA-seq data analysis

RNA-seq analysis was performed as previously described (Dvinge et al., 2014). Briefly, FASTQ files were mapped using RSEM version 1.2.4 (Li and Dewey, 2011) (modified to call Bowtie) (Langmead et al., 2009) with option '-v 2') to mouse or human transcriptome annotations built using transcript information from Ensembl v71.1 (Flicek et al., 2013), UCSC knownGene (Meyer et al., 2013), and MISO v2.0 (Katz et al., 2010). Reads that did not align at this step were then mapped using TopHat version 2.0.8b (Trapnell et al., 2009) to the mouse (GRCm38/mm10) or human (GRCh37/hg19) genome assemblies, as well as to a database of annotated splice junctions as well as all possible new junctions consisting of linkage between each co-linear annotated 5' and 3' splice sites within individual genes. Aligned reads from these two mapping steps were merged to generate final BAM files for all subsequent analyses.

Gene expression estimates were computed using RSEM (performed concordantly with the RNA-seq read mapping procedure described above). Significantly differentially expressed genes were defined as those meeting the follow criteria: minimum expression of 1 transcript per million (TPM); minimum fold-change of 1.5 ( $\log_2$  scale);  $p \leq 0.05$  (computed using an unpaired, two-sided t test comparing replicate groups for a given treatment and cell line) or a minimum Bayes factor of 100 (computed using Wagenmakers's Bayesian framework (Wagenmakers et al., 2010) for the median of gene expression and associated read counts over replicates for a given treatment and cell line). Splice junction-spanning reads were filtered to require a minimum overhang of 6 nt.

MISO v2.0 was used to quantify all expression of isoforms arising from exon skipping (cassette exons), competing 5' splice site selection, competing 3' splice site selection, and annotated intron retention. Quantification of constitutive intron retention, where constitutive introns were defined as those whose 5' and 3' splice sites were never joined to other splice sites in the knownGene annotation, was calculated as previously described (Hubert et al., 2013) using reads with a minimum of 6 nt overhang in both the exon and intron. Events were considered significantly differentially spliced if they met the following criteria: a minimum of 20 identifying reads (reads which align only to one, but not both, isoforms constituting a given splicing event) in each sample; a minimum of 10% change (absolute scale) in isoform ratio or minimum fold-change of 2 ( $\log_2$  scale) in absolute isoform ratio;  $p \leq 0.05$  (computed using an unpaired, two-sided t test comparing replicate groups for a given treatment and cell line) or a minimum Bayes factor of 5 (computed using Wagenmakers's Bayesian framework) (Wagenmakers et al., 2010) for the median of isoform ratios and distinguishing read

counts over replicates for a given treatment and cell line). All data parsing, statistical analyses, and data visualization were performed using the R programming environment with Bioconductor (Huber et al., 2015).

### MHC I immunoprecipitation, peptide purification, and mass spectrometry

Peptide-MHC complexes were isolated as previously described (Abelin et al., 2017), with the following modifications: anti-mouse H-2D<sup>b</sup> (clone B22-249.R1, CedarLane laboratories, Cat. CL9001AP) or H-2K<sup>b</sup> (clone Y-3, BioXCell Cat. BE0172) non-covalently linked to GammaBind Plus Sepharose beads were co-incubated with soluble lysates overnight. After washing with lysis buffer twice, 10mM Tris pH 8 twice, and dH<sub>2</sub>O twice, the peptides were desalted on C18 StaGE tips (Ishihama et al., 2006) (Pierce, Cat. 87784) and eluted using a 20%–35%–50% acetonitrile stepwise gradient. Eluted fractions were dried using a SpeedVac vacuum concentrator and stored until mass spectrometry. For B16-F10, cells in all experimental conditions were treated with 10U/mL mouse IFN $\gamma$  (PeproTech Cat. 315-05) for 48 hours prior to cell harvest and immunoprecipitation to upregulate surface MHC I expression.

### Mass spectrometry

Desalted, dried samples enriched for MHC peptides were resolubilized in 8uL 0.1% TFA and 3uL were loaded onto a packed-in-emitter 12cm/75um ID/3um C18 particles column (Nikkyo Technos Co., Ltd. Japan). Peptides were eluted using a gradient delivered at 300nL/min increasing from 2% Buffer B (0.1% formic acid in 80% acetonitrile) / 99% Buffer A (0.1% formic acid) to 30% Buffer B / 70% Buffer A, over 70 minutes (EasyLC 1200, Thermo Scientific). All solvents were LCMS grade (Optima, Fisher Scientific). MS and MS/MS (HCD type fragmentation) experiments were performed in data dependent mode with lock mass (m/z 445.12003) using Fusion Lumos (Thermo Scientific). Precursor mass spectra were recorded from m/z 300–1500 m/z range at 60,000 resolution. 1, 2 and 3 positive charges were selected for fragmentation experiments. MS/MS spectra were recorded at 30,000 resolution and lowest mass set at m/z 110. For MS/MS acquisition, injection time was set to maximum 100 ms with an Auto Gain Control setting of 5e4. Normalized collision energy was set to 30. All experiments were recorded in FT-mode.

### Proteome creation

Gene and isoform annotations were created as described in RNA-seq data analysis. This merged transcript annotation, as well as the RefSeq annotations of the human and mouse genomes, was used to create the four distinct proteomes described in the main text as follows.

Isoforms were computationally translated into proteins and digested into unique 8-14-mers. Isoforms were translated into proteins “conservatively,” in the sense that the translation was performed assuming that the annotated start codons were used and no stop codon readthrough or internal translation initiation occurred (e.g., generally only the first portion of a retained intron would be translated until an in-frame premature termination codon was encountered, after which translation was assumed to halt). The binding affinity for each resulting peptide to the relevant MHC alleles was then predicted using NetMHCpan v4.0 (Jurtz et al., 2017). Each peptide was annotated with relevant information about its encoding transcript, including parent gene, parent isoform(s), differential gene and/or isoform expression (if relevant), position within parent transcript, unique assignment to one versus two or more isoforms of the originating splicing event (if relevant), etc.

Four distinct, custom proteomes for subsequent spectra mapping were created (illustrated in Figure 5B). (1) “full-length proteome,” created using peptides arising from all unique full-length isoforms. (2) “predicted binders,” created by further restricting to unique 8-14-mers that had a NetMHCpan 4.0 percentile rank < 2 (the recommended cutoff for binders from NetMHCpan 4.0). Two versions of this proteome were created, one including only those isoforms derived from differentially retained constitutive introns based on the RNA-seq data, and one including all isoforms derived from constitutive intron retention (constituting an increase in unique 8-14-mers of ~28%). Analyses used the complete (latter) proteome unless otherwise indicated. (3) “predicted binders + spiked non-binders,” created by augmenting the “predicted binders” proteome with peptides that were predicted to not bind the relevant MHC alleles with high-confidence, defined as having NetMHCpan percentile rank > 90, with the number of such non-binders chosen such that they comprised 10% of the final proteome after adding to the “predicted binders” proteome. (4) “filtered predicted binders,” created by further filtering the “predicted binders” proteome by restricting to peptides arising from genes that were significantly differentially expressed or isoforms that were significantly differentially spliced in indisulam-treated versus DMSO-treated samples, defined based on the RNA-seq analysis for the corresponding cell lines.

### Peptide identification from mass spectrometry data

Mass spectra from all MHC immunoprecipitations were analyzed using Proteome Discoverer v2.4.1.15, with the following workflow. Spectra from each replicate were searched against each distinct proteome (described above) as follows. For each proteome, searches were performed with no enzyme specificity, precursor mass tolerance of 10 ppm, and fragment mass tolerance of 0.6 Da. Oxidation (+15.995 Da), phosphorylation (+79.966 Da), and deamidated (+0.984 Da) dynamic modifications were included, in addition to N-terminal glutamate to pyro-glutamate (–17.027 Da). False discovery rate (FDR) estimation was performed computationally using the Percolator software. Peptides reaching the 5% FDR threshold were retained for downstream analyses. For the “full-length” proteome, identified peptides were further restricted to those of length 8-14 amino acids before being used as input for subsequent analyses. For the “predicted binders,” “predicted binders + spiked non-binders,” and “filtered predicted binders” proteomes, peptides corresponding to subsequences of the sequences in the input proteomes were removed before the identified peptides were used for subsequent analyses.

### Candidate neoepitope identification

As described in the main text, two distinct groups of candidate neoepitopes were selected for subsequent immunization experiments. The first group was based on the intersection between mass spectrometry analyses and RNA-seq analyses. Peptides were first identified using the mass spectrometry analysis described above. These peptides were then restricted to the set of indisulam-specific peptides, where an indisulam-specific peptide was defined as a peptide that was identified in one or more indisulam-treated samples, but not recovered in any DMSO-treated samples. These indisulam-specific peptides were then filtered to retain only those peptides arising from alternative isoforms that were significantly differentially spliced in indisulam-treated versus DMSO-treated cells, and subsequently additionally filtered to require (1) isoform specificity and (2) appropriate direction of differential splicing, with those two criteria defined as follows. (1) An isoform-specific peptide was defined as a peptide which arose exclusively from one isoform associated with a given splicing event (e.g., a peptide from a retained intron event is isoform-specific if it arises from translation of the intronic portion of the unspliced mRNA, or if it arises from translation of the exon-exon junction within the spliced mRNA). This definition means that differential splicing of a given event is predicted to alter levels of the isoform encoding an isoform-specific peptide, and therefore likely similarly alter abundance of the isoform-specific peptide itself. (2) Peptides that exhibit appropriate direction of differential splicing are those isoform-specific peptides which are specifically encoded by differentially spliced isoforms that are promoted by indisulam treatment (e.g., the encoding isoform is present at higher levels in indisulam-treated versus DMSO-treated cells). Isoform-specific peptides were only used for subsequent immunization experiments if their parent isoform was more prevalent in the indisulam treatment, signifying that the peptide is expected to be more abundant in indisulam-treated cells. These criteria yielded 72 peptides, which were subsequently tested in immunization experiments.

The second group of peptides used for immunization experiments was derived by combining evidence from RNA-seq analyses and MHC I binding predictions. This set of peptides was defined using the same criteria described above for the first set (derived by intersecting predictions from mass spectrometry analyses as well as RNA-seq analyses), but without the requirement that peptides be detected as indisulam-specific epitopes via MHC I mass spectrometry. To compensate for the fact that direct protein-level detection was not required, a stringent predicted MHC I binding threshold of rank < 0.5 (the NetMHCpan recommended threshold for strong binders) for one or more relevant alleles was applied (versus the more lenient threshold of rank < 2 used for other, mass spectrometry-based predictions and analyses). Peptides were additionally restricted to those of lengths between 8 and 11 amino acids, as such lengths are preferred by the studied alleles. The final set of peptides used for subsequent immunization experiments was then derived by additionally requiring that peptides be isoform-specific; arise from genes with expression > 5 TPM in corresponding indisulam-treated samples (in order to favor peptides from relatively highly expressed genes); and have a difference in isoform ratio > 20% in indisulam-treated versus DMSO-treated samples, and isoform ratio < 25% in DMSO-treated samples (in order to restrict to peptides that were associated with more dramatic splicing changes). These criteria yielded 39 peptides, which were subsequently tested in immunization experiments.

### Peptide synthesis

Experimental peptides were individually custom synthesized via the solid-phase method by GenScript (Piscataway, NJ), with standard removal of trifluoroacetic acid and replacement with hydrochloride, purified to > 98% by HPLC, and lyophilized for storage. Peptides were reconstituted in DMSO at 10 mg/mL and frozen at  $-80^{\circ}\text{C}$  until use.

### RMA-S peptide H-2 stabilization assay

RMA-S cells were maintained under standard conditions in RPMI + 7.5% FCS for expansion. H-2 stabilization experiments were performed as previously described (Ross et al., 2012). Briefly, RMA-S were exposed to  $31^{\circ}\text{C}$  and 5%  $\text{CO}_2$  conditions overnight, incubated with peptides of interest for 30 minutes at  $31^{\circ}\text{C}$ , and then returned to  $37^{\circ}\text{C}$  and 5%  $\text{CO}_2$  for three hours prior to cell surface staining for H-2K<sup>b</sup> (clone AF6-88.5) and H-2D<sup>b</sup> molecules (clone KH95) and standard flow cytometry analysis. For Figures 5N–5Q, spike-in negative control peptides were as follows for each experimental peptide – Hus1: PPSGRALLW; Zpf512: QKPKGSQRG; D14Abb1e: LKPQAKRSK; Poldip3: GESWQEKER

### TiterMax immunization

Unless otherwise specified, 10  $\mu\text{g}$  of peptide was emulsified with TiterMax Classic (TiterMax Corp., Norcross, GA) and injected into the hocks of anesthetized animals. On day +7 after challenge, draining lymph nodes were collected and CD8<sup>+</sup> T cells purified by magnetic selection (Miltenyi Biotec, Cat. 130-117-044).

### IFN $\gamma$ ELISpot

CD8<sup>+</sup> T cells from TiterMax immunized animals were cultured overnight with 20 U/mL mouse IL-2 (PeproTech, Cat. 212-12) and plated at  $10^5$  per well in combination with  $3 \times 10^5$  T cell depleted syngeneic splenocytes which had been loaded with 100  $\mu\text{g}/\text{mL}$  of peptides of interest for 18 hours. PMA 1  $\mu\text{g}/\text{mL}$  + ionomycin 500 ng/mL stimulation of T cells served as positive control.

In some experiments, in lieu of peptide-loaded splenocytes, instead ovalbumin-expressing B16-F10 cells or B16-F10 cells treated with DMSO or indisulam 1  $\mu\text{M}$  for 96 hours were stimulated overnight with IFN $\gamma$  100U/mL for the last 24 hours of cell culture. Such cells were then non-enzymatically harvested, washed repeatedly to remove IFN $\gamma$ , and irradiated to 60 Gy from a  $^{60}\text{Co}$  source to inhibit growth and further upregulate MHC I. Tumor cells thus generated were counted and incubated with CD8<sup>+</sup> T cells at identical ratios as for splenocytes ( $10^5$  CD8<sup>+</sup> T cells +  $3 \times 10^5$  melanoma cells). IFN $\gamma$  ELISpot was performed as per manufacturer's instructions (BD

Biosciences, Cat. 551083). Spots were imaged and quantified on an Immunospot® analyzer (Cellular Technology Limited, Cleveland, OH).

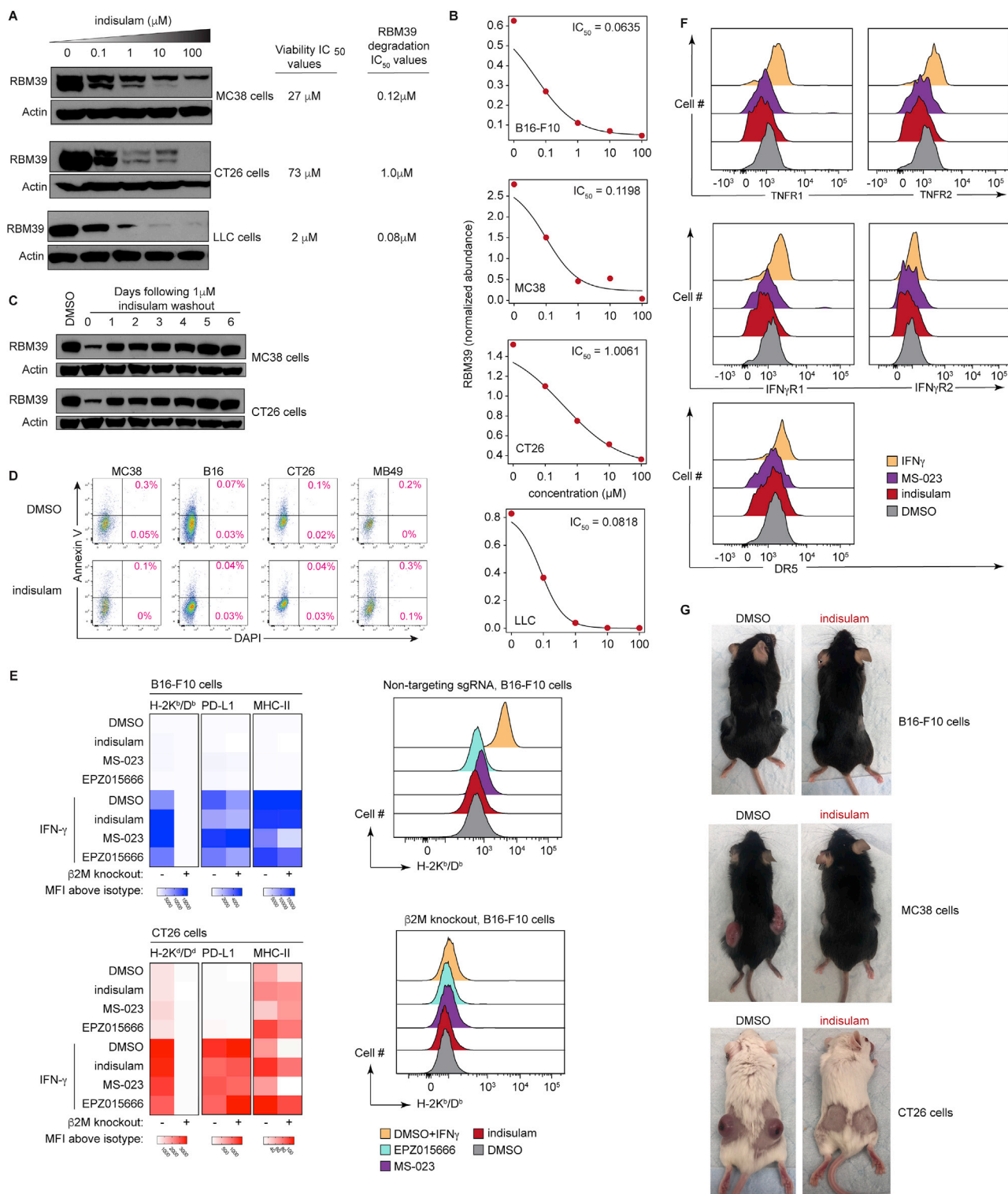
#### **B16-F10 co-culture cytotoxicity assay**

B16-F10 cells were harvested, counted, and plated at  $10^4$  per well in the presence of 100U/mL IFN $\gamma$  overnight to upregulate MHC I. After washing, peptides were loaded onto tumor cells at 100  $\mu$ g/mL, and  $10^6$  CD8 $^+$  T cells from TiterMax immunized animals were added to the tumor cells. 50 U/mL mouse IL-2 was added to this co-culture of tumor cells + CD8 $^+$  T cells, which was incubated for three days. After washing to remove free (detached) B16-F10 and T cells, viable B16-F10 were harvested, stained (to exclude T and other hematopoietic cells) and absolute cell numbers enumerated via flow cytometry using counting beads according to the manufacturers' instructions (ThermoFisher Cat. C36950).

#### **QUANTIFICATION AND STATISTICAL ANALYSIS**

All data summarization, visualization, and statistical analysis were performed using GraphPad Prism v9.0 (GraphPad Software, San Diego, CA) or in the R programming language. Details for statistical procedures, including statistical test used, number of replicates, definition of center, and definition of error bars are found within the figure legends. Unless otherwise noted in the text, n represents biological replicates of the sample type (e.g., individual tumors, independent cell cultures, etc.) indicated in the figure legend. The normality of data was assessed using a Shapiro-Wilk test. If data were normally distributed, a parametric test (e.g., unpaired, two-sided t test) was used to test for significant differences between groups; otherwise, a non-parametric test (e.g., Wilcoxon rank-sum test) was used, as indicated in the figure legends. Differences between groups were considered significant if  $p$  was less than 0.05. No methods were used for sample randomization or sample size estimation and no data were excluded from analysis.

# Supplemental figures



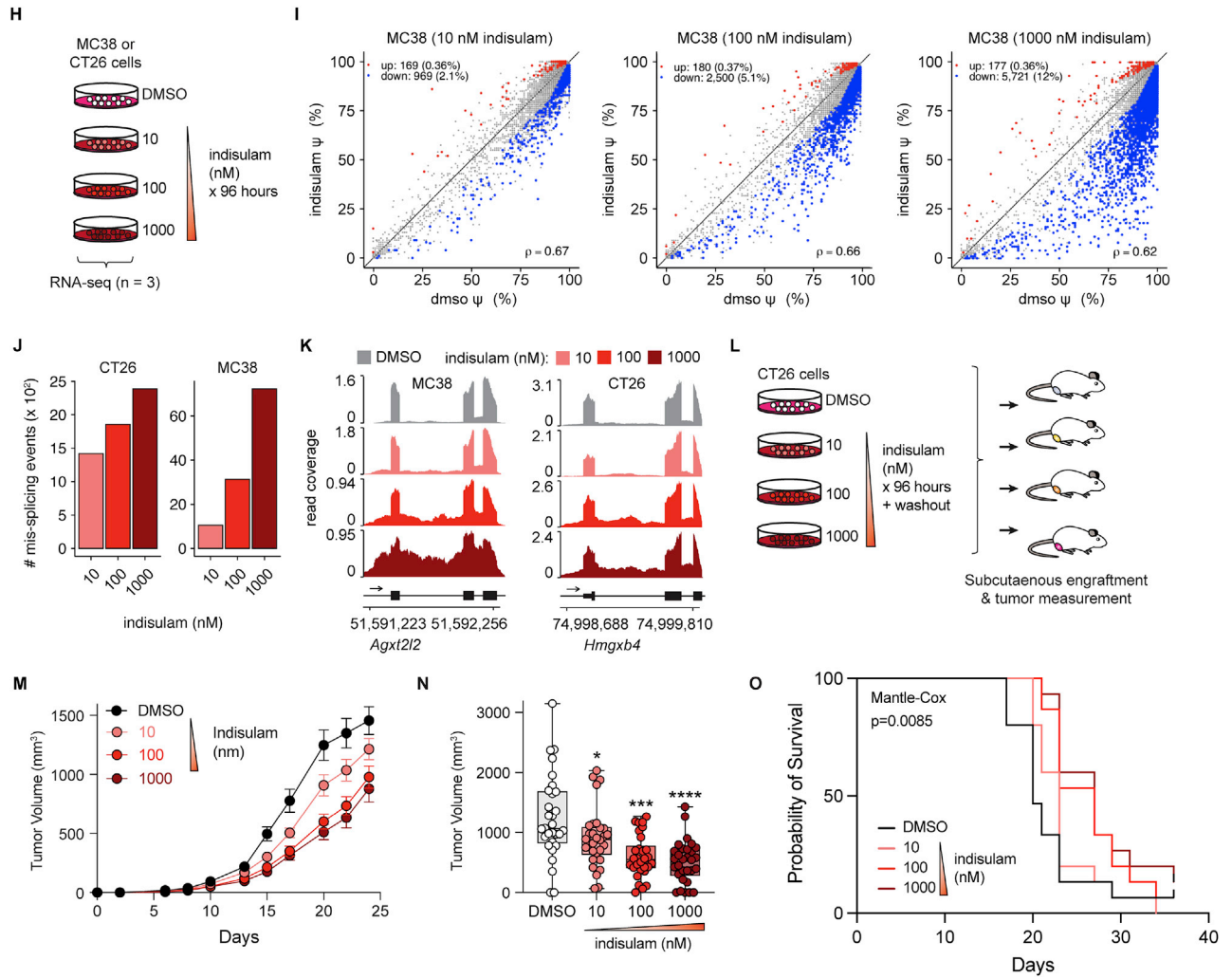


(figure continued on next page)

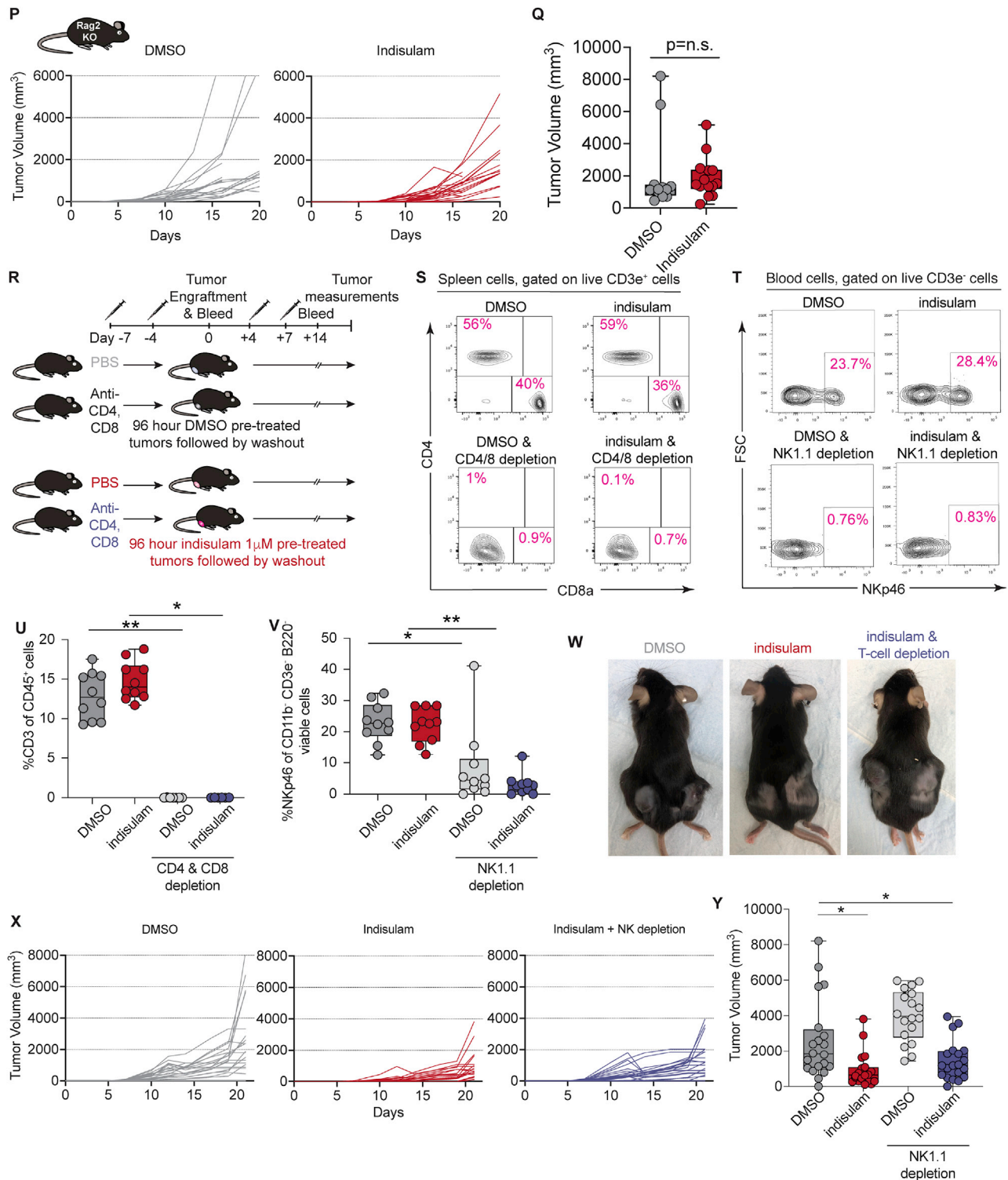


**Figure S1. Pharmacologic perturbation of RNA splicing impairs tumor growth *in vivo*, in a dose-dependent fashion dependent on adaptive immunity, related to Figure 1**

(A) Left, western blot of RBM39 after *in vitro* exposure to the indicated concentrations of indisulam for 24 hours in MC38 and CT26 cells. Right, half-maximal inhibitory concentration (IC<sub>50</sub>, computed using the Hill equation) values for cell growth inhibition and RBM39 degradation. (B) Dose-response curves for RBM39 abundance (normalized to β-actin) across the indicated concentrations of indisulam treatment as measured by densitometry. IC<sub>50</sub> values are shown. (C) Western blot of RBM39 after MC38 or CT26 cells were exposed to 1 μM indisulam for 96 hours, drug was washed off, and RBM39 levels were allowed to recover. (D)

(legend continued on next page)

Annexin-V and DAPI analysis of MC38, B16-F10, CT26, and MB49 cells after *in vitro* treatment with indisulam 1  $\mu$ M or DMSO for 96 hours. (E) Heatmap of MFI values above isotype control of cell surface levels of H-2K/H-2D, I-A/I-E (MHC II), or PD-L1 after 96 hours of treatment with DMSO, indisulam 1  $\mu$ M, MS-023 5  $\mu$ M, or EPZ015666 1  $\mu$ M, or the same drugs in the presence of mouse IFN $\gamma$  10U/mL. CRISPR-mediated  $\beta_2$ -microglobulin knockout cells served as biologic control for H-2K/H-2D staining. B16-F10 cells shown on top (blue). CT26 cells on bottom (red). Representative histograms of B16-F10 data are shown on right. (F) Cell surface levels of cytokine and death receptors in B16-F10 cells after treatment with conditions identical to (D). (G) Sample photos of B16-F10 (top), MC38 (middle), CT26 (bottom) bearing mice treated with indisulam or DMSO and engrafted into syngeneic animals. (H) Experimental schema. MC38 or CT26 cells were treated with DMSO or indisulam at the indicated concentrations for 96 hours in technical triplicate; these were then subjected to RNA-seq analyses or used for biological experiments as in (L-O). (I) numbers of constitutive U2-type introns retained in MC38 cells treated with the indicated doses of indisulam compared with DMSO. (J) Total number of splicing alterations in CT26 and MC38 tumors exposed to the indicated doses of indisulam, as compared with DMSO. (K) RNA-seq coverage plot depicting two representative intron retention events in Agxt2l2 and Hmgxb4 with increasing doses of indisulam. (L) experimental schema showing the engraftment of CT26 tumors treated with indisulam *in vitro* into syngeneic BALB/c mice. (M) tumor volumes of CT26 bearing mice from (L) over time (n = 15 mice/group; tumors engrafted on bilateral flanks of mice). Mean  $\pm$  sem. (N) tumor volumes from (M) at day 24. P values were calculated for the indicated group compared to DMSO control using the Wilcoxon rank-sum test: \*p = 0.048; \*\*\*p = 0.000798; \*\*\*\*p = 0.000363. (O) Kaplan-Meier survival curve of animals from (L). (P) Individual tumor growth curves for DMSO-treated and indisulam-treated B16-F10 cells in Rag2 knockout mice. n = 10 mice per group; tumors engrafted on bilateral flanks. (Q) Box-and-whisker plots of day 28 individual tumor volumes from (P). (R) Schema of CD4 & CD8 T cell depletion or NK cell depletion versus control. (S) Representative flow cytometry confirmation of T cell depletion using anti-CD4 and anti-CD8 antibodies, gated for CD3 $\epsilon$  in the spleens of animals sacrificed at day 19 post-tumor challenge. Remaining double-negative population are NK1.1<sup>+</sup> NKT cells (not shown). (T) Representative flow cytometry confirmation of NK cell depletion via NKp46 antibody; peripheral blood on day 14 after tumor challenge. (U-V) Box-and-whisker plot quantification of (S) and (T). Each dot represents an individual animal. (W) Sample photos of tumor-bearing animals treated with CD4/CD8 T cell depletion and challenged with B16-F10 cells pre-treated with indisulam or control. (X) Individual tumor growth curves for NK1.1 depletion experiment. n = 10 per group; tumors engrafted on bilateral flanks. (Y) Box-and-whisker plots of day 21 tumor volumes for B16-F10 treated as in [Figure 1A](#), with or without NK cell depletion. \*p < 0.05; \*\*p < 0.01. ANOVA calculated using the Kruskal-Wallis test and multiple comparisons versus DMSO alone calculated using the Dunn's test.

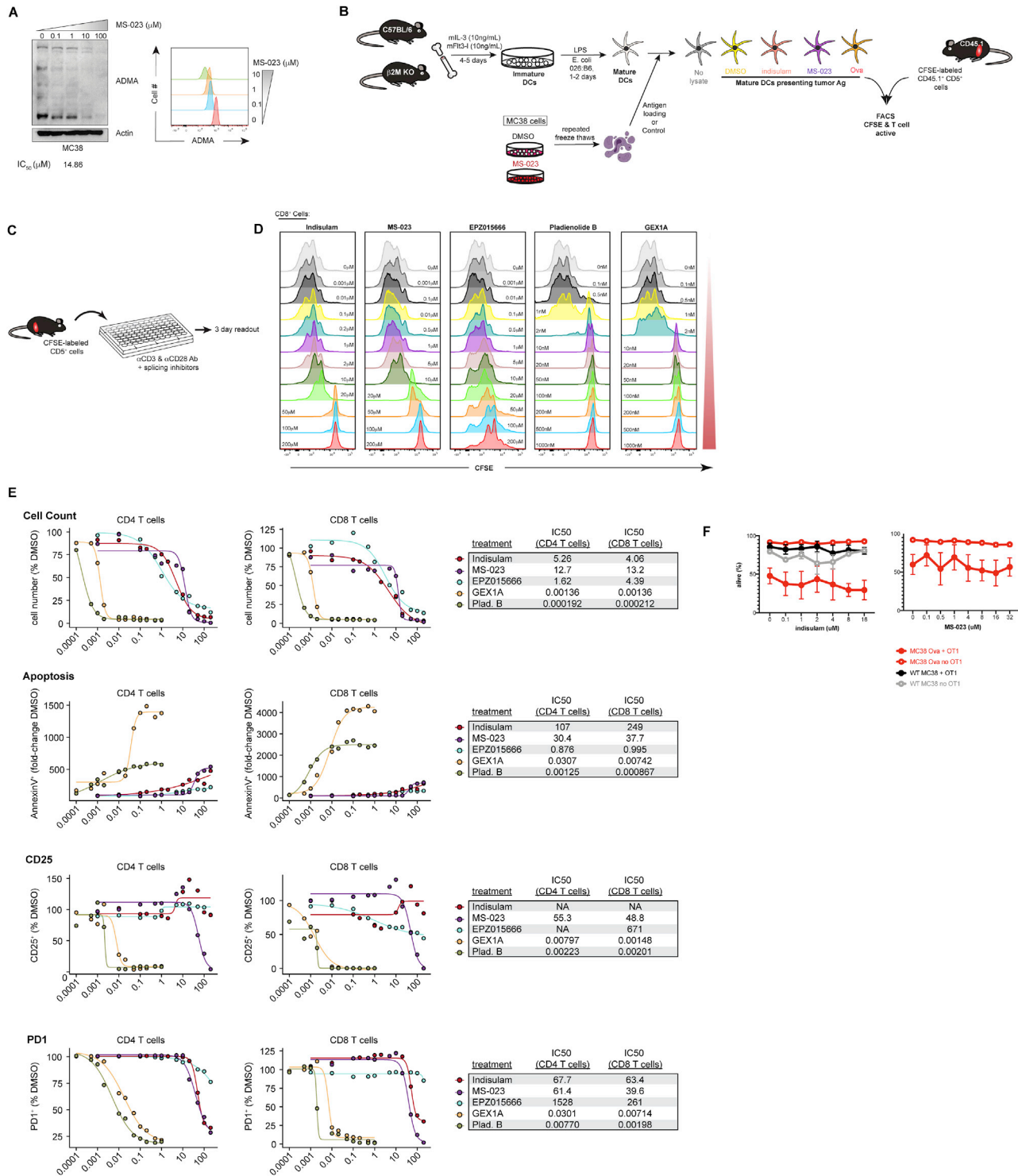


(figure continued on next page)

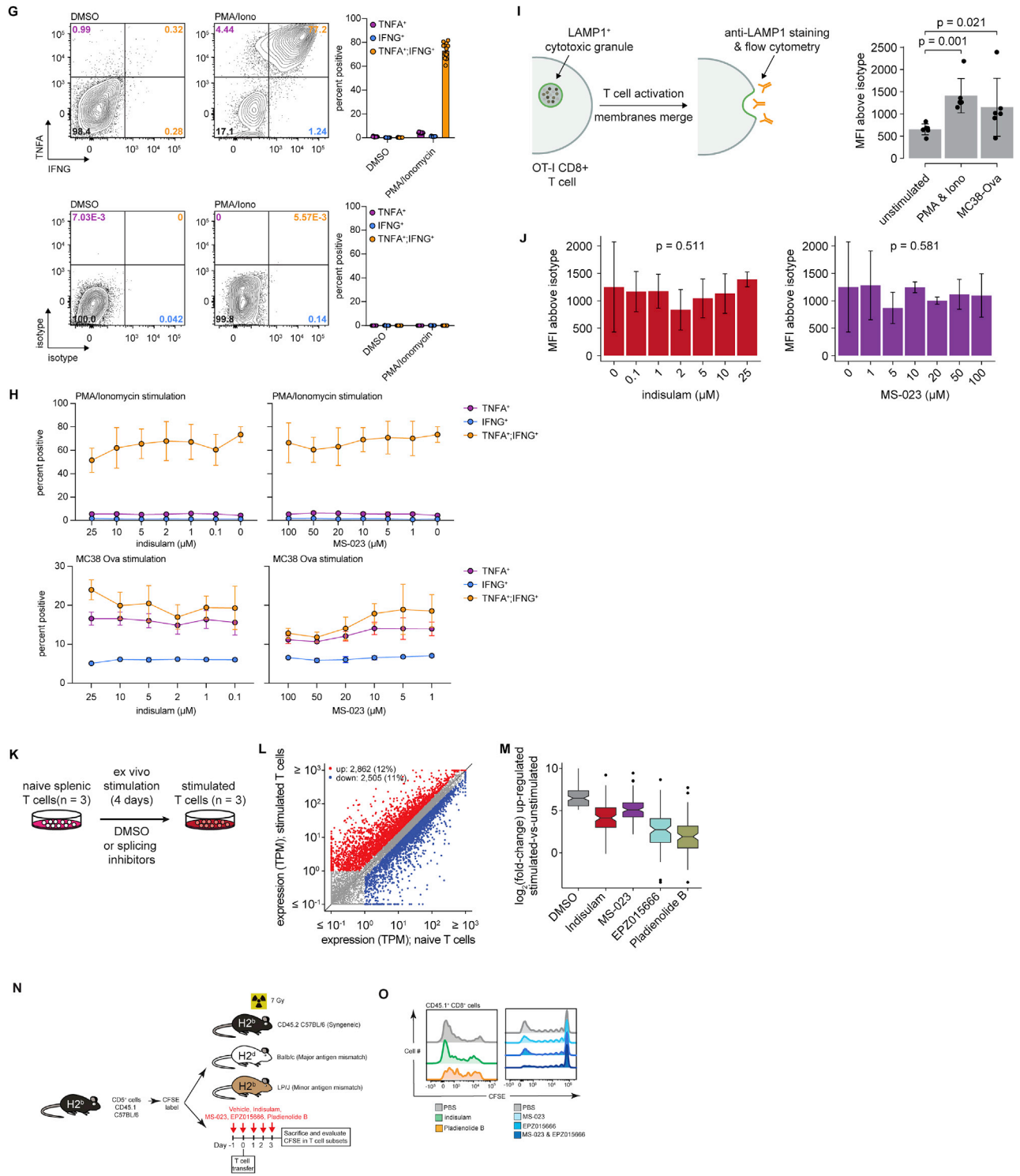
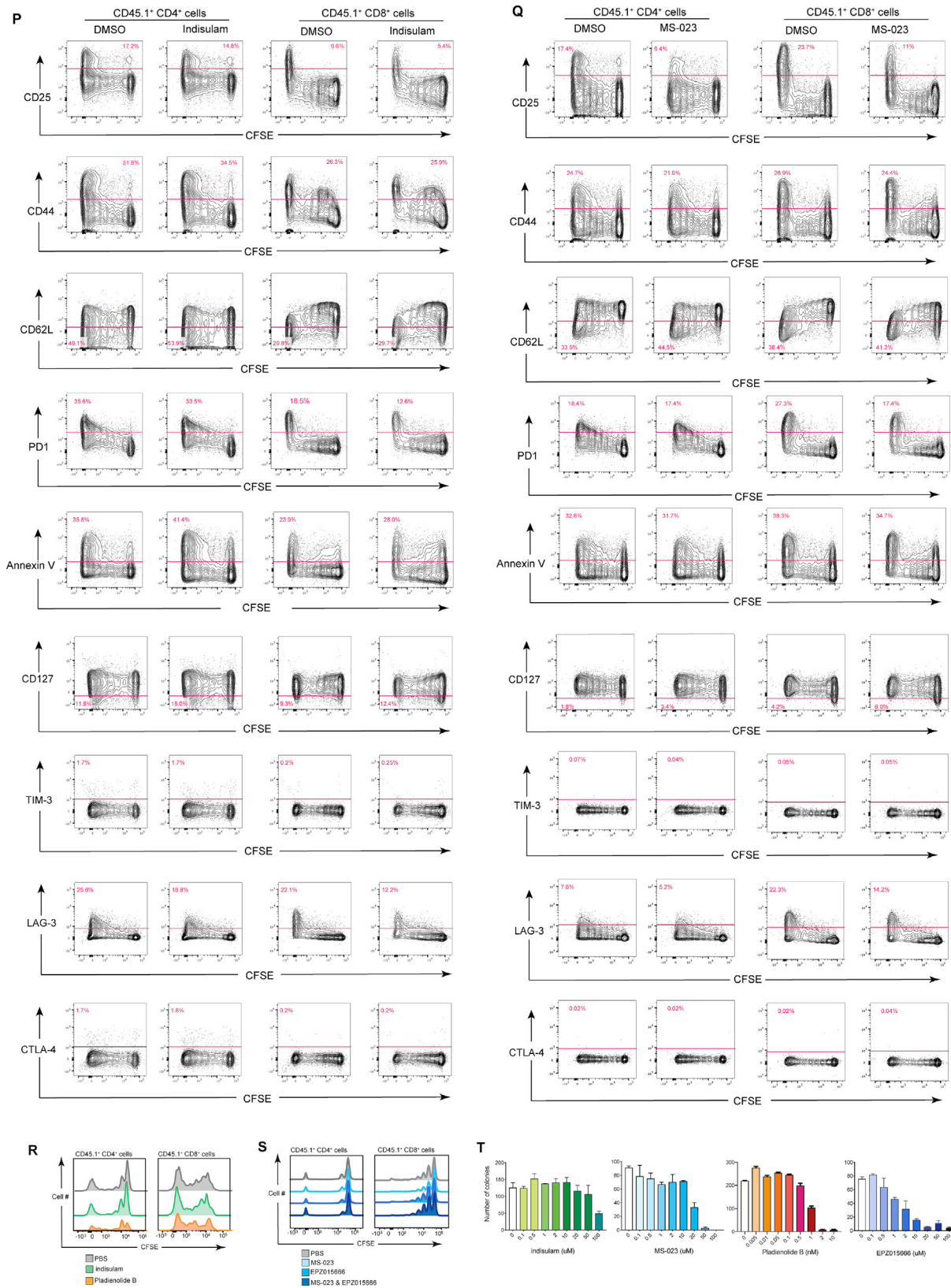


(figure continued on next page)



(legend on next page)

**Figure S2. Class-specific effects of splicing modulator drugs on hematopoiesis, T cell gene expression, and function *in vitro* and *in vivo*, related to Figure 2**

(A) Left, western blot showing dose-dependent reduction in asymmetric dimethyl arginine (ADMA) with MS-023 treatment in MC38 tumor cells; right, corresponding flow cytometry analysis for intracellular ADMA. (B) Schema for the mixed leukocyte reaction, depicting generation of tumor lysates, generation of bone marrow derived dendritic cells, process of pulsing dendritic cells with lysates and lipopolysaccharide (LPS) for maturation and antigen presentation, and mixed leukocyte reaction with congenic CD45.1 CFSE-labeled naive splenic T cells. (C) Schema depicting purification of splenic T cells, CFSE labeling, and *in vitro* stimulation with plate-bound anti-CD3 and anti-CD28 antibody in the presence of splicing drugs. (D) Full dose range of splicing drugs tested in (C) demonstrating dose-dependent inhibition of CFSE dye dilution and T cell proliferations at higher drug concentrations; representative histogram from N = 8 technical replicates each. (E) absolute numbers of CD4 (left) and CD8 (right) T cells from experiment in (C) for each drug and concentration were quantified to calculate IC<sub>50</sub> for cell proliferation (table). Each dot is the average from 3-8 technical replicates. Curves and IC<sub>50</sub> values for the activation markers CD25 and PD1 are shown (bottom panels), and EC<sub>50</sub> for induction of apoptosis as measured by annexin-V staining is shown (middle panel). (F) OT-1 killing assay against wild-type or ovalbumin-expressing MC38 tumors; experiment performed as in Figure 2G. (G) representative contour plots showing the staining of OT-1 cells for TNF $\alpha$  and IFN $\gamma$  or isotype control, after exposure to DMSO (left) or PMA/Iono (Phorbol 12-myristate 13-acetate and Iono: ionomycin, right). Percentage of positive cells are quantified in the associated bar plots. Each dot is one technical replicate. (H) As in (G) but OT-1 cells were stimulated with PMA/Iono (top) or incubated with MC38 cells overexpressing ovalbumin at a 1:1 ratio (bottom), at the indicated concentrations of indisulam or MS-023 on the x axis. Graph shows mean  $\pm$  sem. N = 4 technical replicates per condition. (I) Experimental schema demonstrating normal intracellular localization of the LAMP1 protein on cytotoxic granules in resting cytotoxic T cells, and appearance of LAMP1 on the plasma membrane upon T cell degranulation, rendering the protein stainable for flow cytometry. Bar plots at right show LAMP1 MFI of OT-1 cells remaining unstimulated, exposed to PMA/ionomycin, or incubated at a 1:1 ratio with MC38 overexpressing ovalbumin. Each dot indicates a technical replicate. P values were calculated using the Wilcoxon rank-sum test. (J) experiment as in (I) except in the presence of the indicated doses of indisulam or MS-023 on the x axis. N = 4 technical replicates per condition. Graph shows mean  $\pm$  SD. P values were calculated using the Kruskal-Wallis non-parametric ANOVA test. (K) experimental design: naive C57BL/6 splenic T cells were isolated and cultured *ex vivo* for 96 hours in media with IL-2 50U/mL. Cells were either left unstimulated, or activated with plate-bound anti-CD3 + CD28 antibody in the presence of DMSO or the indicated splicing compounds: indisulam 1  $\mu$ M, MS-023 1  $\mu$ M, EPZ015666 5  $\mu$ M, or pladienolide B 2nM. At the end of 96 hours, cells were subjected to RNA-seq. N = 3 replicates for each condition. (L) Differential gene expression from (K) of unstimulated T cells versus those stimulated in the presence of DMSO. (M) Boxplots of fold changes of the top 100 upregulated genes in T cells undergoing activation from (K) in the presence of the indicated drugs. Each dot is one replicate. (N) Schema of adoptive transfer of C57BL/6 CD45.1 CFSE labeled T cells into syngeneic, minor antigen mismatched, or major antigen mismatched lethally irradiated recipients to assess T cell activation and expansion. (O) Histograms of CFSE dilution of donor adoptively transferred CD45.1<sup>+</sup> CD8<sup>+</sup> T cells into BALB/c mice on day 3 to assess for alloreactivity. (P) Representative flow cytometry plots of T cell activation and death markers in adoptively transferred donor CFSE-labeled CD45.1 splenic CD4<sup>+</sup> or CD8<sup>+</sup> T cells into lethally irradiated BALB/c recipients with or without daily indisulam (25 mg/kg) treatment. Spleens were analyzed on day 3. Two animals from each condition are shown. (Q) as in (P) but with daily MS-023 treatment, 50mg/kg daily. (R-S) Histograms of CFSE dilution in donor adoptively transferred CD45.1<sup>+</sup> T cells into syngeneic C57BL/6 mice to assess for homeostatic proliferation. Cells in the spleen on day 7 after transfer are shown. (T) Numbers of colonies in M3434 methylcellulose media on day 7. 25,000 red blood cell-lysed bone marrow hematopoietic stem and precursor cells (HSPC) from C57BL/6 mice were grown in methylcellulose with continuous exposure to splicing compounds at the indicated concentrations.

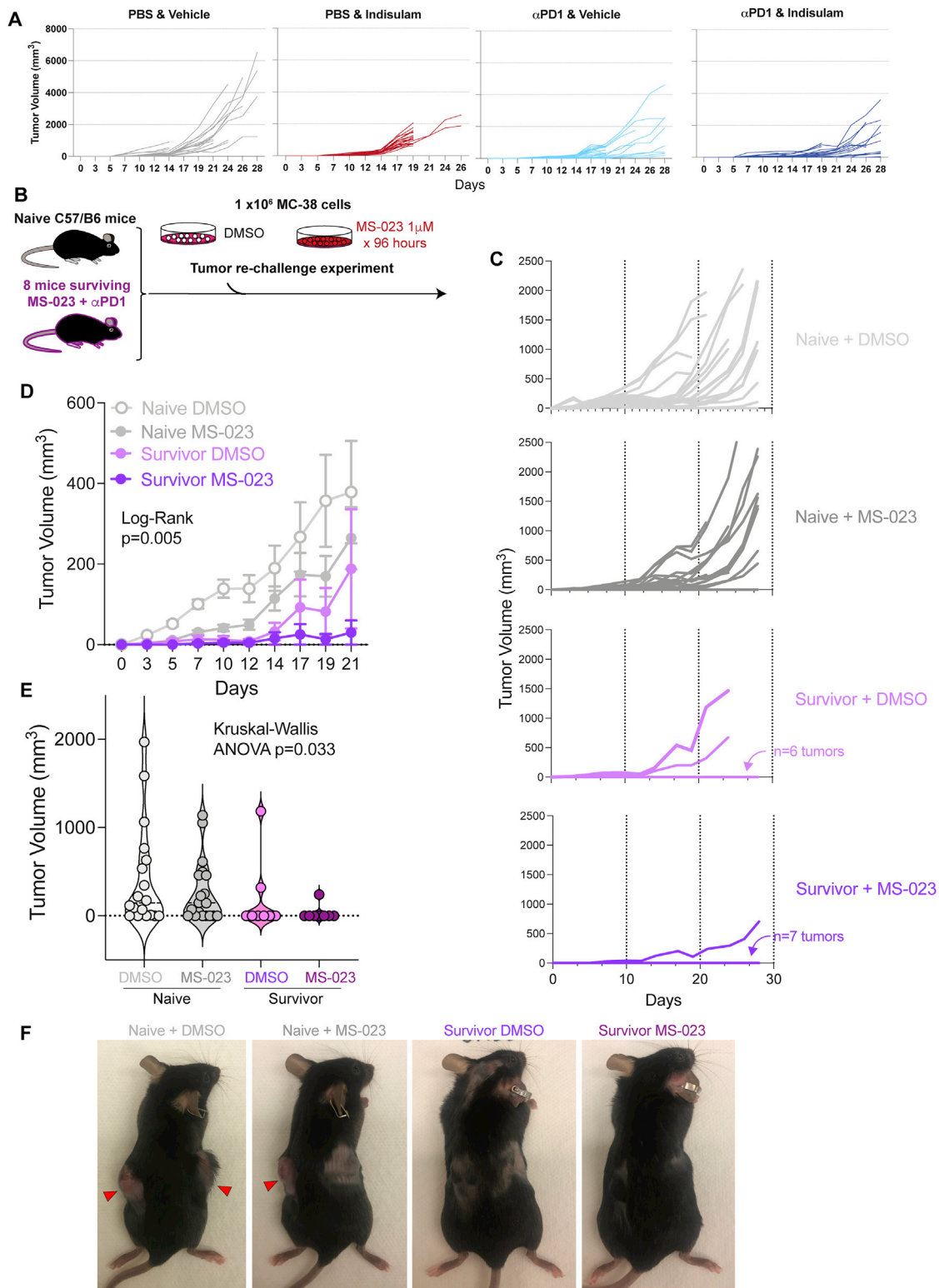


**Figure S3. Treatment of tumor-bearing animals with splicing modulator compounds *in vivo* enhances tumor control and can elicit memory, related to Figure 3**

(A) Growth curves of individual B16-F10 tumors from C57BL/6 mice exposed to the indicated treatment, as summarized in Figure 3C. Each line represents one tumor; termination of lines prior to the end of the experiment indicates animal mortality or euthanasia according to predetermined endpoints, as described in the

(legend continued on next page)

---

STAR Methods section. (B) Experimental design: MC38 cells were treated with DMSO or MS-023 *in vitro* for 96 hours, and then  $10^6$  cells engrafted onto the bilateral flanks of either naive C57BL/6 mice, or animals which had successfully rejected MC38 tumors previously after treatment with anti-PD1 and MS-023 *in vivo* (from Figures 3K–3M). (C) Growth curves of individual tumors from (B). Pink and purple arrows indicate tumors which were implanted but rejected. (D) Line graphs summarizing growth curves from (C), showing mean  $\pm$  sem. (E) Violin plots showing tumor volumes at day 28. P values (calculated using the Wilcoxon rank-sum test) for the “DMSO survivor” -versus- “DMSO naïve” and “MS-023 survivor” -versus- “MS-023 naïve” comparisons are 0.044 and 0.011, respectively. (F) Representative animals from (E).

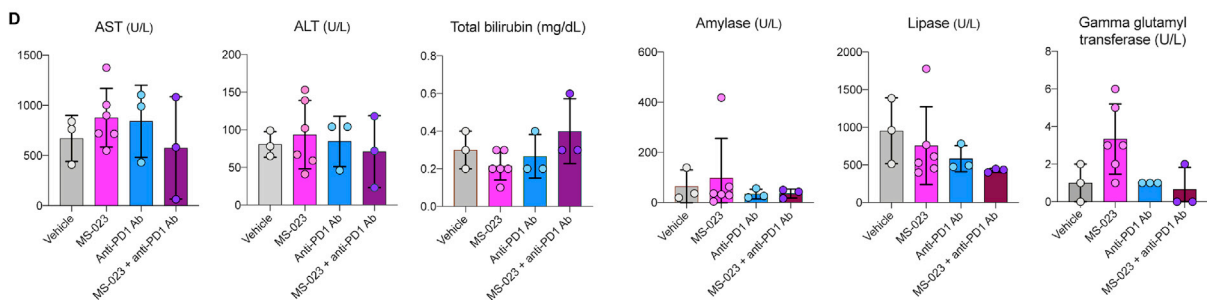
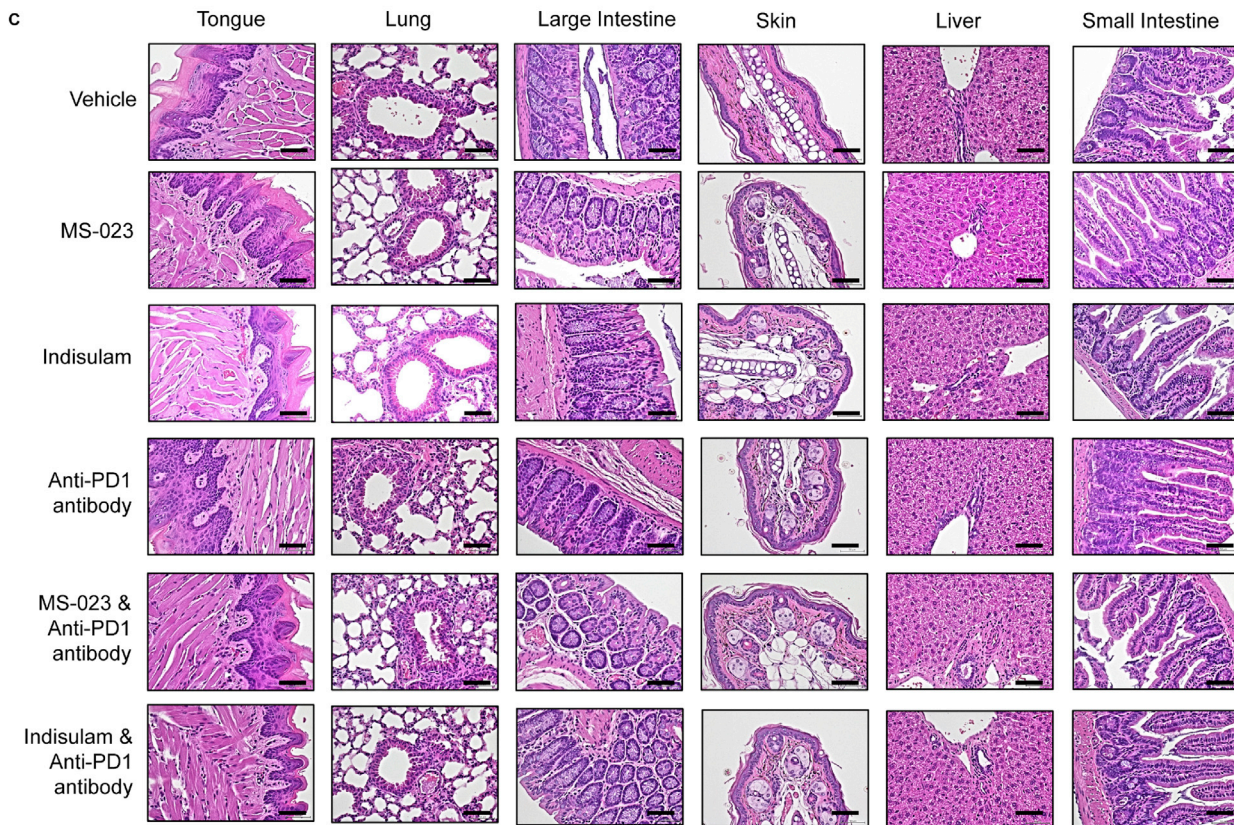
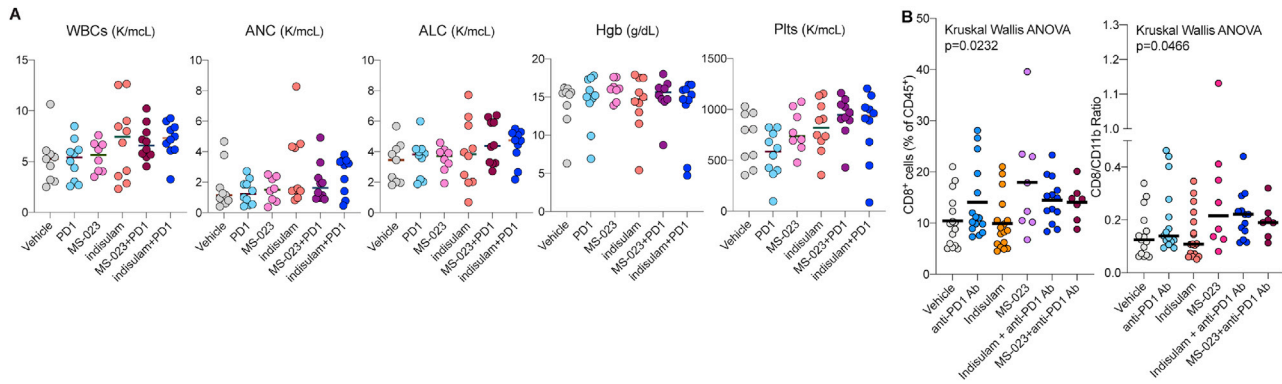


(figure continued on next page)

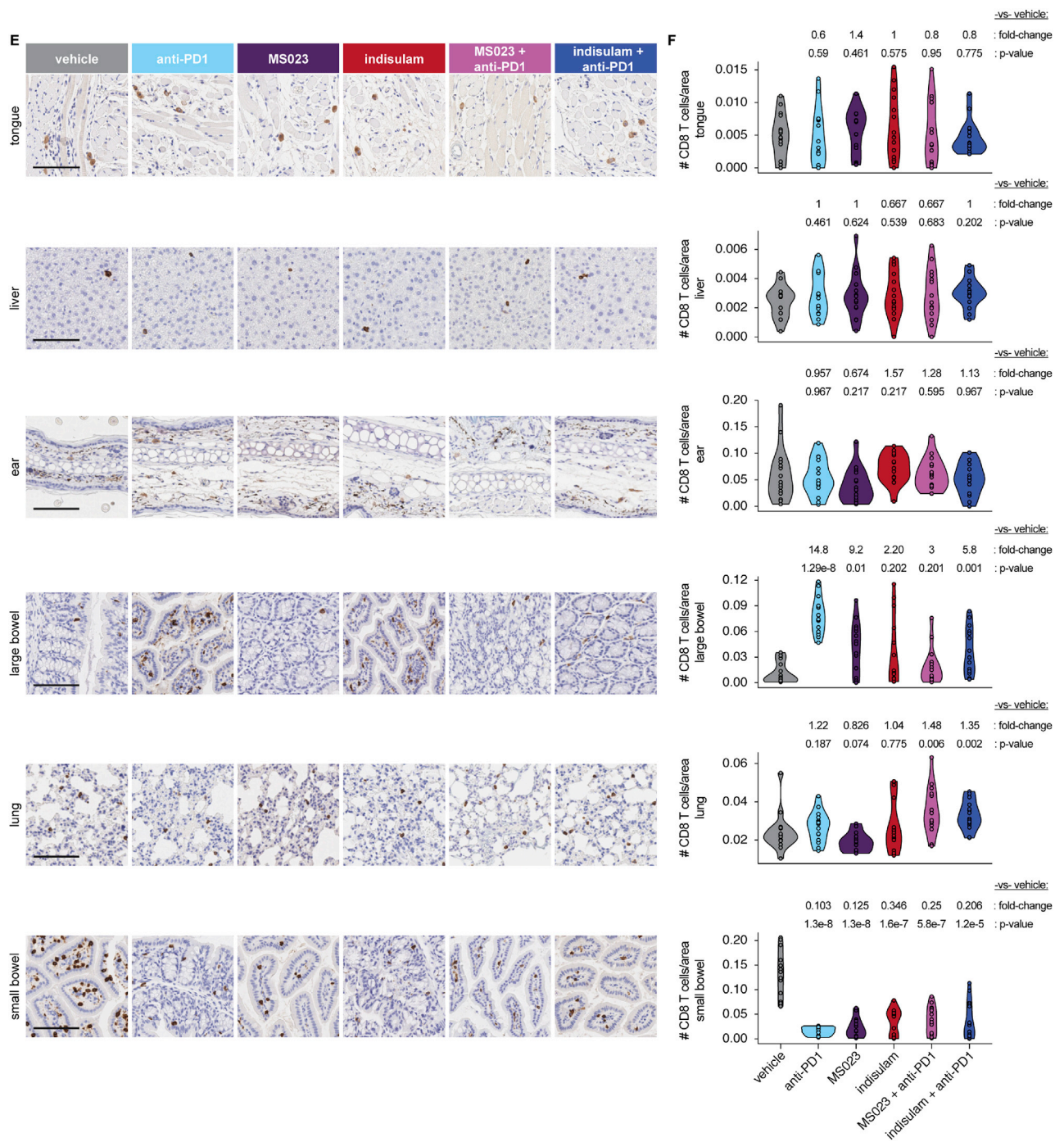


(figure continued on next page)

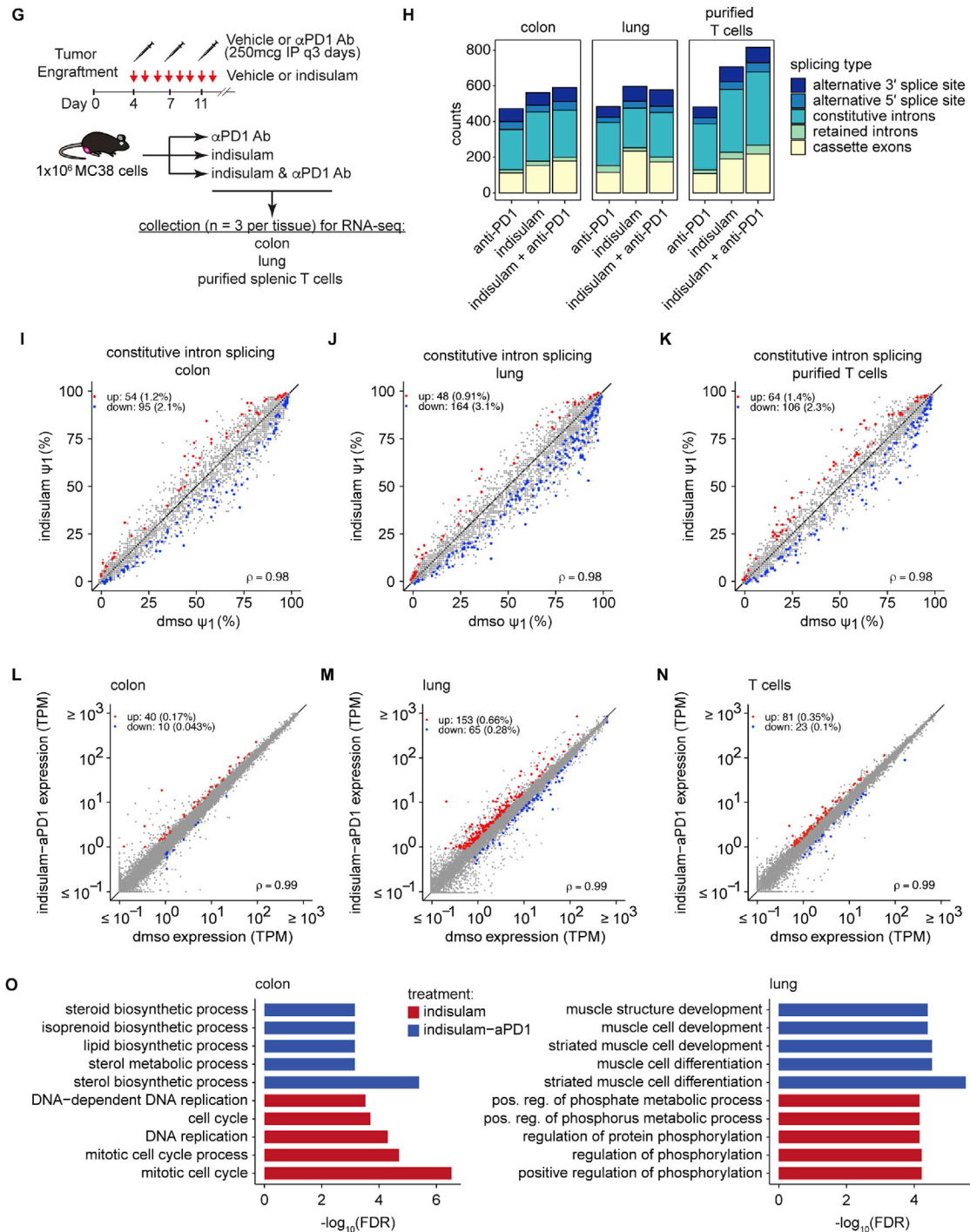


**Figure S4. Lack of toxicity and absence of inflammatory signatures or increased CD8<sup>+</sup> T cell infiltrates into healthy, non-tumor tissues in animals treated with splicing modulator compounds with or without anti-PD1, related to Figure 3**

(A) Peripheral blood counts of tumor-bearing mice treated for 3 weeks with vehicle, anti-PD1 (250  $\mu$ g flat dose), indisolam (25 mg/kg), MS-023 (50 mg/kg), or combined anti-PD1 with MS-023 or indisolam. ALC: absolute lymphocyte count; ANC: absolute neutrophil count; Hgb: hemoglobin; Plt: platelet count; WBC: white blood cell count. (B) Percentage of CD8<sup>+</sup> cells among CD45<sup>+</sup> cells (left) and proportion of CD8<sup>+</sup>/CD11b<sup>+</sup> cells (right) in tumors at day 21 following treatment of animals bearing MC38 tumors with the treatments indicated on the x axis. n = 10 mice/group. ANOVA calculated using the Kruskal-Wallis test. (C) H&E stained tissue sections from mice treated with indisolam, MS-023, anti-PD1, or combination at day 21. N = 5 animals per treatment group per tissue were assessed. Review of the necropsy tissues shows no overt evidence of toxicity, and the tongue shows typical squamous epithelium overlying bundles of skeletal muscle. The lung demonstrates typical alveolar spaces, alveolar septa, and bronchioles with respiratory epithelium. The large intestine shows typical colonic mucosa,

(legend continued on next page)

---

submucosa, and muscularis propria. The skin from the ear demonstrates typical epidermis, dermis, and subcutaneous tissues overlying cartilage. The liver shows typical portal tracts and hepatocytes, and the small intestine demonstrates normal villi with typical mucosa, submucosa, and muscularis propria. Representative micrographs of the findings are depicted. (H&E; Magnification 400x; Scale bar: 50 microns). (D) Liver and pancreas enzymes and markers in the blood from these same animals at the time of sacrifice (n = 3 mice/group). ALT: alanine aminotransferase. AST: aspartate aminotransferase. Mean  $\pm$  sd shown. (E) B16-F10-tumor bearing C57BL/6 mice received the indicated treatment; tissues were collected on day 21. Paraformaldehyde-fixed and paraffin-embedded tissues were sectioned and stained for CD8 by immunohistochemistry. Representative sections of the tongue (muscle), liver, ear (skin), small and large bowel and lung are shown. 20x magnification. Scale bar: 100 microns. (F) Violin plots depicting the automated enumeration of CD8<sup>+</sup> T cell infiltrates in the corresponding organs are shown. N = 3 mice per tissue per treatment were analyzed, and N = 5 fields per mouse were analyzed. Fold-change in CD8<sup>+</sup> T cell infiltrates versus the vehicle condition are shown. p values were calculated using the Wilcoxon rank-sum test. (G) Experimental design: C57BL/6 mice were engrafted with 10<sup>6</sup> MC38 tumor cells on each flank and subjected to treatment with vehicle, indisulam 25mg/kg beginning day +3, anti-PD1 250  $\mu$ g twice weekly beginning day +7, or the combination. Lung, colon, and splenic T cells were obtained on day 14 after tumor challenge for RNA-seq. (H) Stacked bar graphs indicating the absolute number and type of splicing alterations in the lungs, colon and T cells of animals receiving the indicated therapy. Splicing alterations were defined as a 5% change in splicing with a p value threshold of 0.05 (I-K) Scatterplots indicating constitutive intron retention in tissues of animals treated with indisulam versus vehicle. (L-N) Scatterplots indicating differentially expressed genes in the colon, lung and T cells of animals treated with vehicle versus combination of indisulam and anti-PD1. (O) Pathway analyses of differential gene expression from (L-M) in the colon and lung. No significantly enriched gene ontology pathways were identified in the T cell RNA-seq dataset.

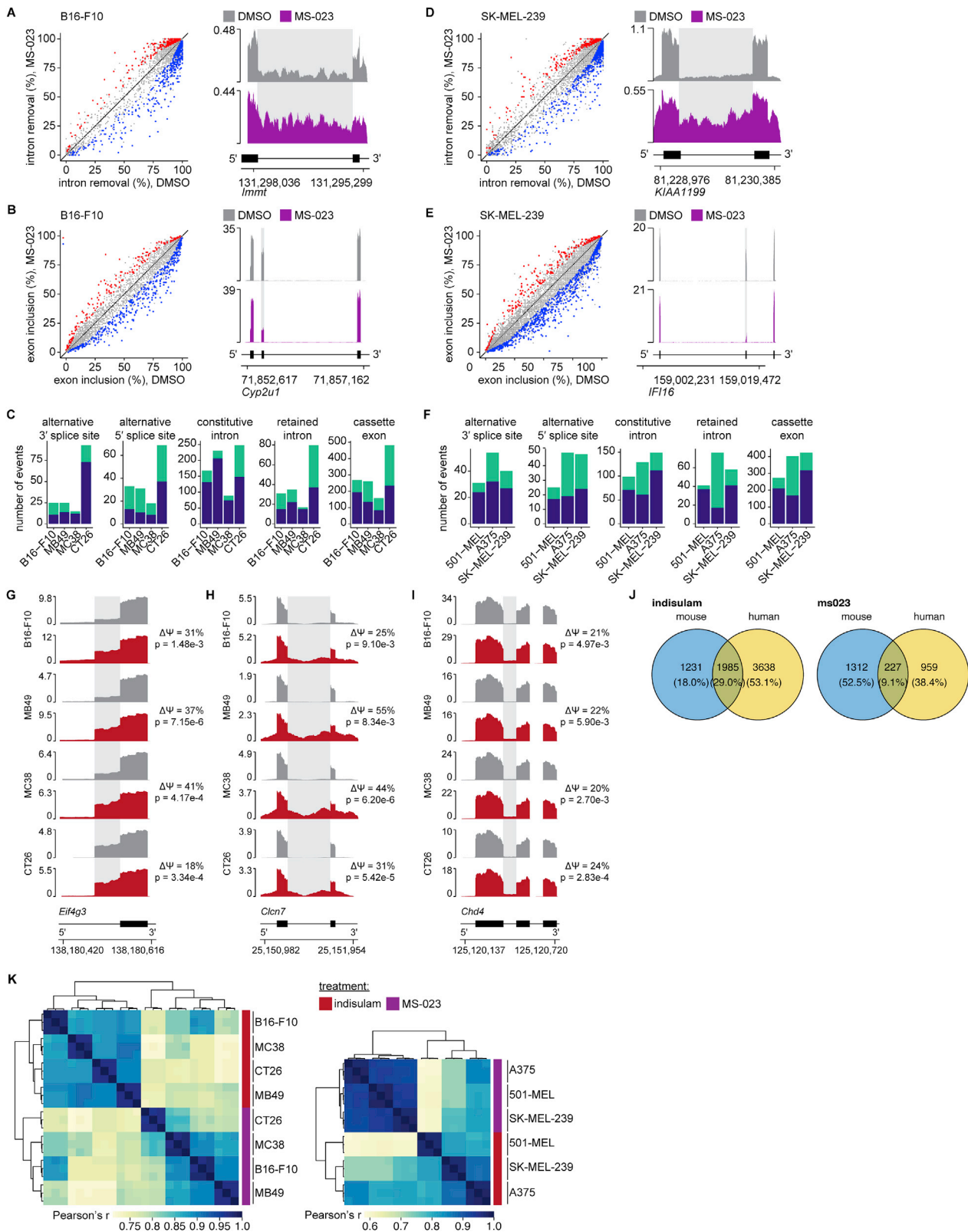


(figure continued on next page)

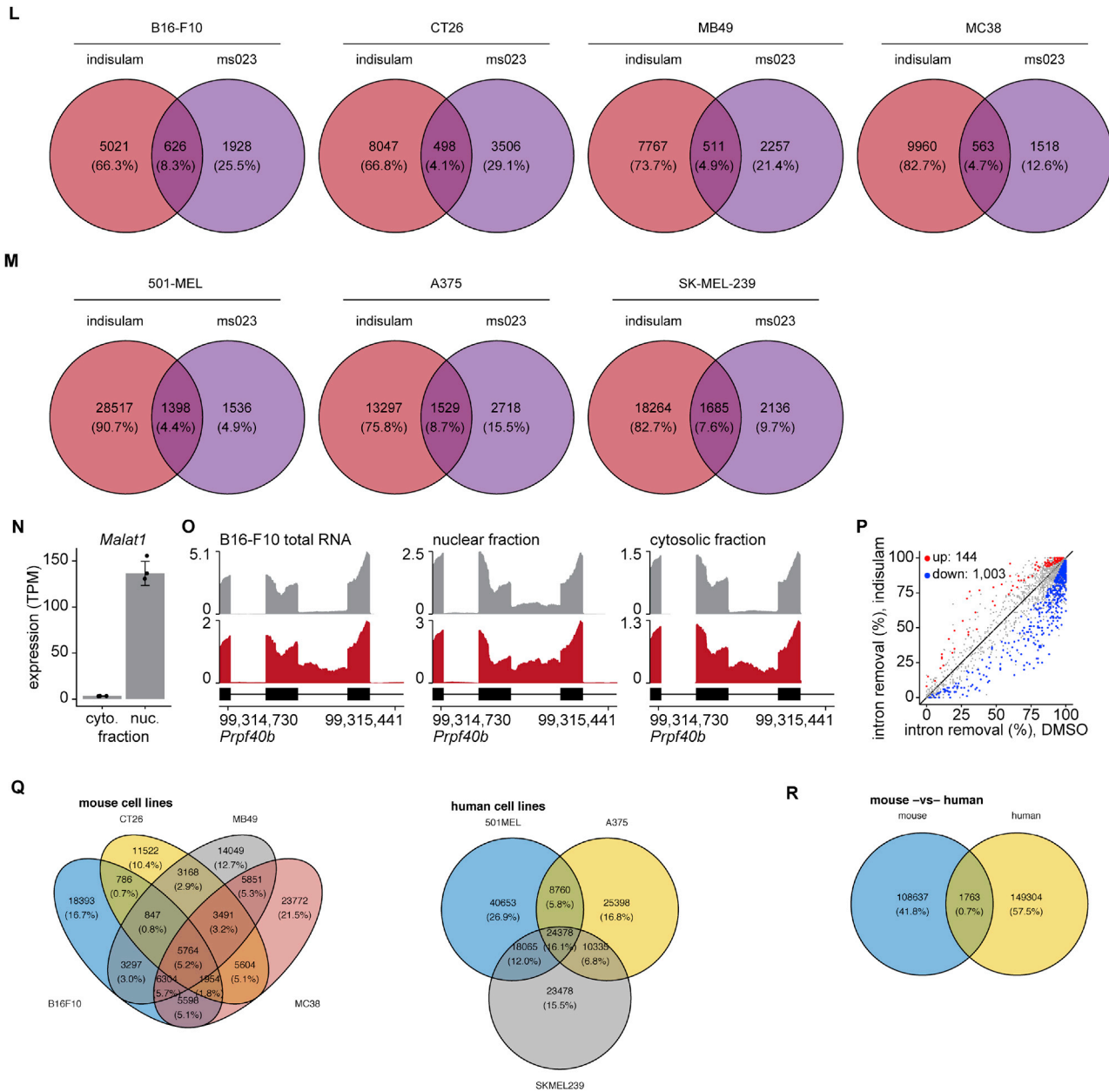


**Figure S5. Splicing alterations generated by MS-023 and indisulam treatment, related to Figure 4**

(A) Left, scatterplot comparing constitutive intron splicing in DMSO- versus MS-023-treated B16-F10 cells. Right, RNA-seq read coverage illustrating increased intron retention following MS-023 treatment. (B) As (A), but for cassette exons. (C) Bar graphs representing numbers of differentially spliced events of each indicated type in DMSO- versus MS-023-treated B16-F10 cells. Blue/green, mis-splicing events indicative of reduced/increased splicing efficiency (for example, decreased/increased cassette exon inclusion). (D) As (A), but for human SK-MEL-239 cells. (E) As (D), but for cassette exons. (F) As (C), but for human SK-MEL-239 cells. (G) representative example of a 5' alternative splice site event induced with indisulam treatment in all of the murine cell lines studied. (H-I) two representative examples of intron retention events observed in all murine cell line studied. (J) Venn diagram depicting the number of genes mis-spliced in common across mouse versus human cell lines analyzed, upon exposure to either indisulam or MS-023. (K) Left, heatmap illustrating Pearson correlations for all retained introns, constitutive introns, and cassette exons that are differentially spliced following indisulam or MS-023 treatment in at least one sample from the indicated mouse cell lines. Pearson correlations computed using the absolute isoform expression values (0%–100%) for each splicing event. Right, identical analysis, but for human data. Dendrograms, unsupervised clustering by the Euclidean distance method. (L) Venn diagrams depicting shared mis-splicing events upon exposure to indisulam or MS-023 in the indicated murine cell lines. (M) as for (L) but for the indicated human cell lines studied. (N) Bar graph of *Malat1* RNA levels in the cytoplasmic (cyto.) and nuclear (nuc.) fractions of DMSO-treated B16-F10 cells. As *Malat1* RNA is restricted to the nucleus (Hutchinson et al., 2007), these data confirm the specificity of our fractionation. (O) RNA-seq read coverage illustrating that increased *Prpf40b* intron retention following indisulam treatment of B16-F10 cells is evident in total (left), nuclear (middle), and cytoplasmic (right) fractions. Gray, DMSO treatment; red,

(legend continued on next page)

---

indisulam treatment. (P) Scatterplot comparing constitutive intron splicing in the cytoplasmic fractions of DMSO- versus indisulam-treated B16-F10 cells. Increased intron retention is readily evident in the cytoplasm. (Q) Venn diagram indicating shared and unique predicted neoantigens among mouse and human cell lines, treated with either indisulam or MS-023. (R) Shared and unique predicted neoantigens, across mouse and human cell lines upon treatment with splicing modulator compounds.

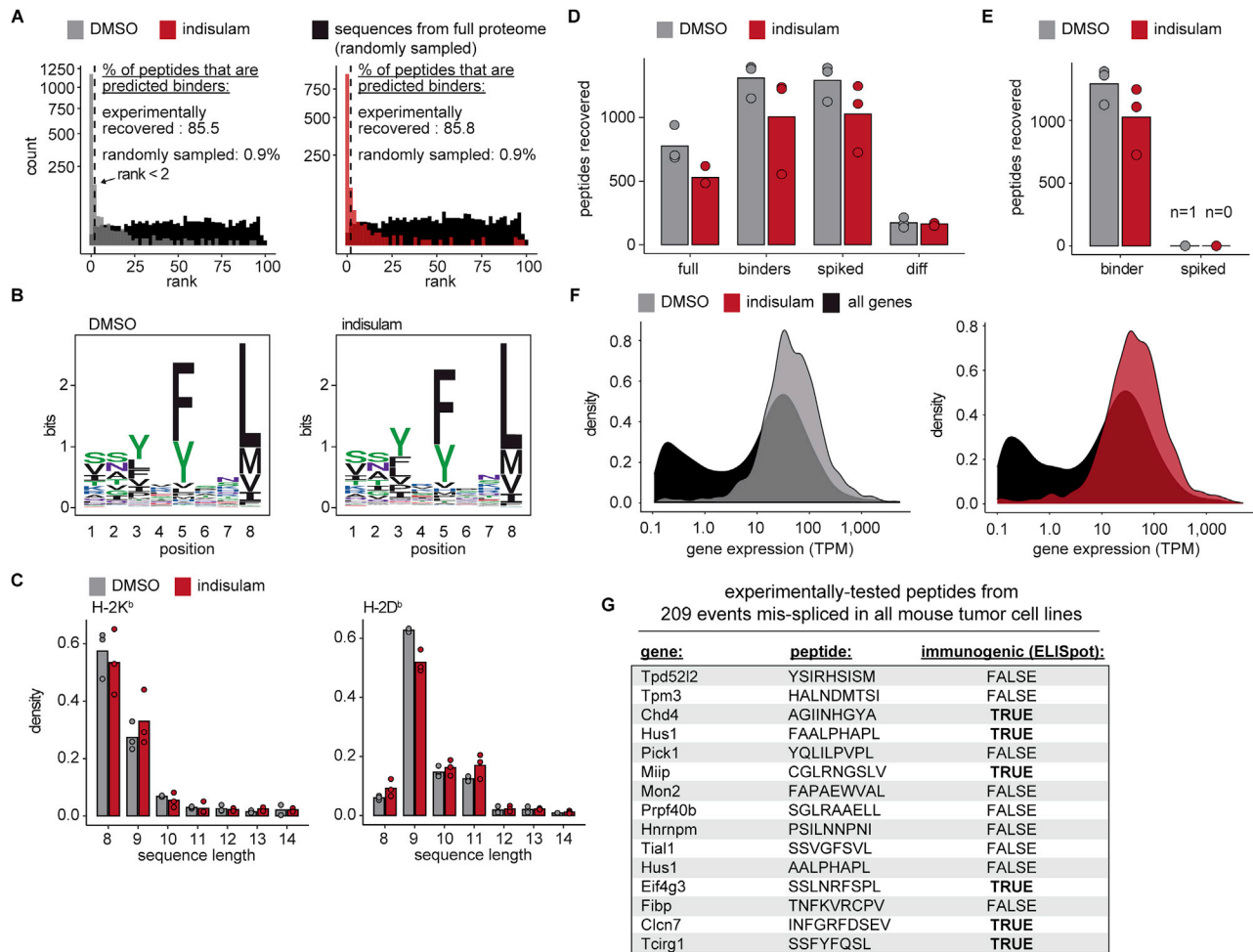


**Figure S6. Analysis of mass spectrometry results for H-2D<sup>b</sup> and H-2K<sup>b</sup> immunoprecipitations, related to Figure 5**

(A) As Figure 5A, but for H-2K<sup>b</sup> immunoprecipitation. (B) As Figure 5D, but for H-2K<sup>b</sup> immunoprecipitation. (C) Histogram of lengths of identified peptides using the predicted binders proteome. The majority of identified peptides are 8-9-mers, as expected. (D) As Figure 5E, but for H-2K<sup>b</sup> immunoprecipitation. (E) As Figure 5F, but for H-2K<sup>b</sup> immunoprecipitation. (F) As Figure 5G, but for H-2K<sup>b</sup> immunoprecipitation. (G) Table showing selected candidate neoantigenic peptides induced by indisulam exposure and shared across MC38, B16-F10, CT26 and MB49 mouse tumor cell lines, which were subjected to experimental analysis by TiterMax immunization of C57BL/6 mice followed by evaluation of reactive CD8<sup>+</sup> T cells by IFN $\gamma$  ELISpot.

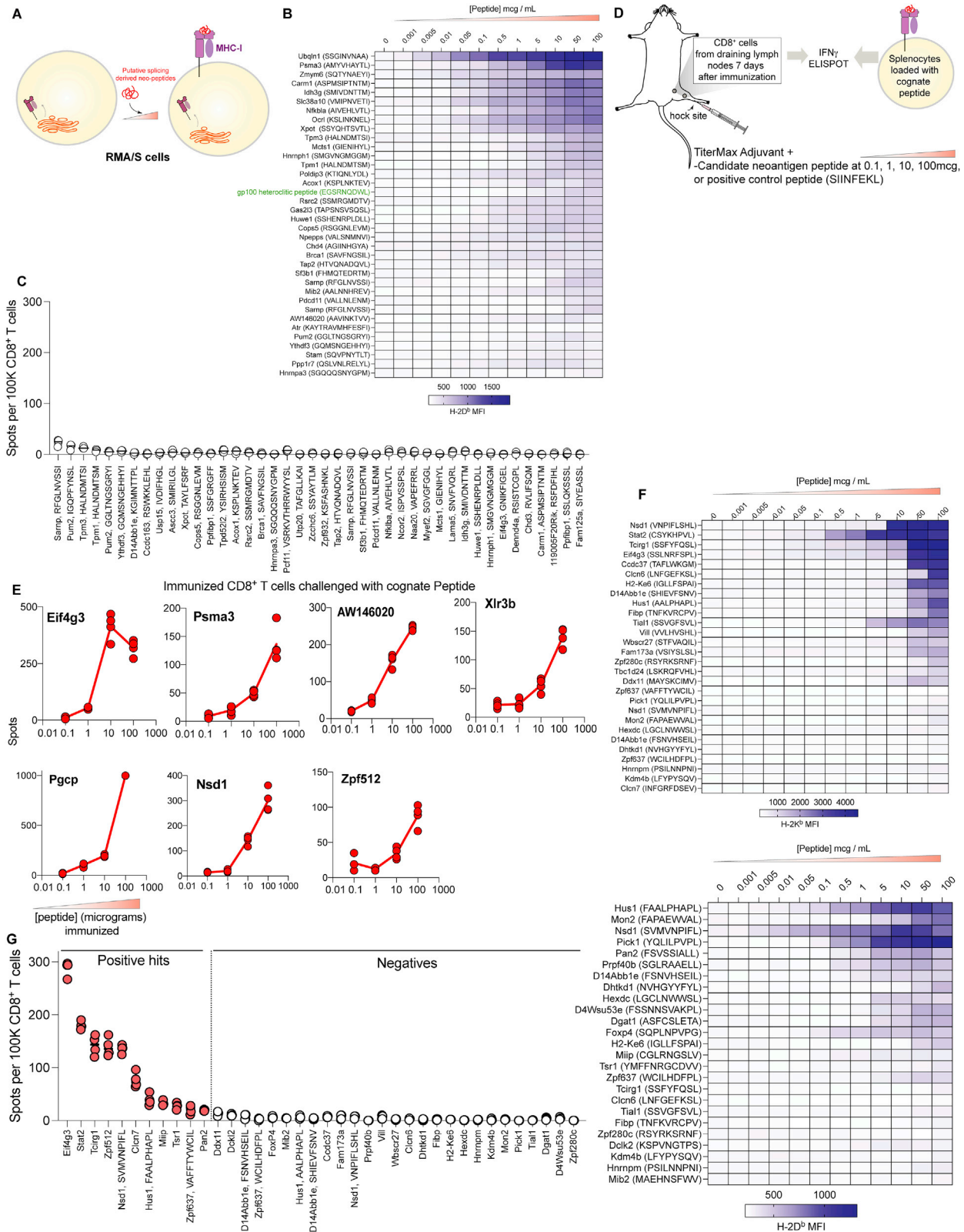


(figure continued on next page)

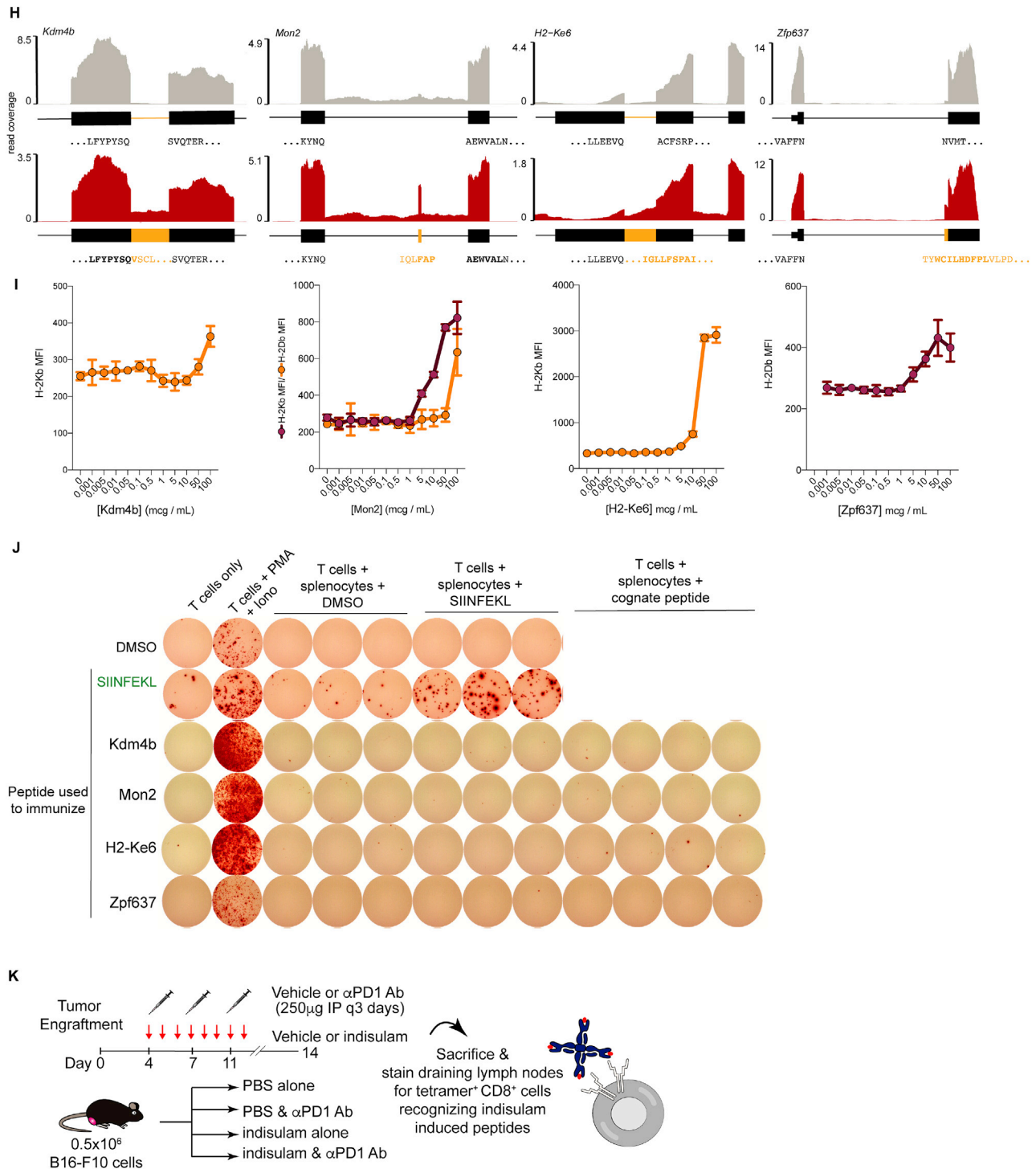


**Figure S7. Functional evaluation of candidate splicing-derived, neoantigenic peptides, related to Figures 6 and 7**

(A) Schema of MHC I peptide stabilization assay on TAP-deficient RMA-S cells. (B) Heatmap of mean MFI values of H-2D<sup>b</sup> levels from RMA-S peptide stabilization experiments across 30 peptides identified as binding to H-2D<sup>b</sup> in the RMA-S assay. Green text indicates control known immunogenic peptide with H-2D<sup>b</sup> binding (gp100). (C) Number of spots per 10<sup>5</sup> CD8<sup>+</sup> T cells from IFN $\gamma$  ELISpot quantified across 70 peptides derived from mass spectrometry analyses and tested *in vivo* which did not elicit an immune response. Bar indicates median. Each dot represents a technical replicate. (D) Diagram of experiment immunizing C57BL/6 mice with graded doses of candidate peptides at 0.1, 1, 10, or 100  $\mu$ g followed by analysis of CD8<sup>+</sup> T cells in IFN $\gamma$  ELISpot. (E) Results from experiment described in (D), with graded doses of the indicated peptide on the x axis. Each dot indicates one technical replicate. (F) As (B), but for H-2K<sup>b</sup> and H-2D<sup>b</sup> expression levels from the RMA-S assay for candidate splicing-derived neoantigenic peptides induced by indisulam that were identified based on RNA-seq data and MHC I binding predictions alone. Some peptides appear twice as they bind to both H-2K<sup>b</sup> and H-2D<sup>b</sup>. (G) As (C), but for the 39 candidate splicing-derived neoantigenic peptides

(legend continued on next page)

---

induced by indisulam identified based on RNA-seq data and MHC I binding predictions alone. (H) RNA-seq coverage plots of representative indisulam-induced, candidate splicing-derived neoantigens generated by intron retention events in *Kdm4b* and *H2-Ke6*, cassette exon inclusion in *Mon2*, and competing 3' splice sites in *Zpf637*. Indisulam-promoted peptide shown in bold, underlined text. (I) Median fluorescence intensities (MFIs) of H-2D<sup>b</sup> and/or H-2K<sup>b</sup> on RMA-S cells following incubation with increasing doses of candidate nonantigenic peptide from (H). Mean  $\pm$  sd shown. (J) Representative ELISpot images for the peptides from (H). (K) Schema of peptide:MHC I tetramer studies. B16-F10 tumor-bearing animals were treated with vehicle, anti-PD1, indisulam or the combination and were sacrificed at day 14 post-tumor challenge. Tumor-draining lymph nodes were analyzed for the frequency of tetramer-positive CD8<sup>+</sup> T cells.